이학박사 학위논문

# Computational Study on Amyloid Formation and Peptide Self-Assembly

2015년 8월

서울대학교 대학원

화학부 물리화학 전공

박 성 병

# Computational Study on Amyloid Formation and Peptide Self-Assembly

지도교수 신 석 민

이 논문을 이학박사 학위논문으로 제출함.

2015년 6월

서울대학교 대학원

화학부 물리화학 전공

박 성 병

박성병의 박사학위논문을 인준함.

2015년 6월

위 원 장 이상엽 (인)

부 위 원 장 신석민 (인)

위 원 석차옥 (인)

위 원 정연준 (인)

위 원 장순민 (인)

# Abstract

## Computational Study on Amyloid Formation and Peptide Self-Assembly

PARK, SeongByeong

Physical Chemistry, Dept. of Chem.,

The Graduate School

Seoul National University

According to the DNA doctrine, a genetic information flows from a DNA to a protein via the processes, such as the replication, the transcription, and the translation. In the post-translation, proteins are folded as corresponded to their functions and at that time self-assembly phenomena take place. On the aspect of the energy landscape, proteins could have the energy-deep corresponding to the folding structure. However, IDPs like $\alpha$-Synuclein and A$\beta_{40/42}$ don't show such the energy-deep. Since any faults in the flow of the genetic materials from the replication to the post-translation can cause severe disease, precise understanding on the structure and the dynamics of such proteins would be necessary even for therapeutic purposes.

We performed the MD simulation for several types of $\alpha$-Synucleins, A$\beta$s, and artificial peptides under various conditions with the REMD and the classical MD methods.

As for $\alpha$-Synuclein which consists of 140 amino acids and

three functional domains (the membrane binding, the NAC and the acidic domains), P128 in the acidic domain gets in touch with the middle of the NAC domain with higher probabilities and factors, such as the P-to-A mutation in the acidic domain and the change of the acidity, make this characteristics diminished. Therefore, the acidic domain is implied to play a role in the aggregation of $\alpha$-Synuclein as an intramolecular chaperone.

As for A$\beta$ which is secreted from APP by ß-secretase and has the chain lengths of 40 or 42 in general, the extra IA terminal residues make potential energies of intermediates more discriminated, barriers between intermediates elevated, and gains of binding energies more beneficial. The F(19,20)I/L mutation deepens this characteristics. Therefore, the extra IA residues are thought to play a role in the aggregation of A$\beta$ as a facilitator.

As for artificial peptides which mimic the $\beta$-barrel structure in nature, the Coulombic interaction, the hydrogen bonding, the hydrophobic interaction, and the optimally minimized electronic repulsion contribute to the formation of the bionanostructure. Of those interactions, the optimal electronic repulsion is the key factor in controlling the artificials.

.....

keywords: MD, α-Synuclein, A$\beta$, chaperone, and facilitator

*Student Number*: 2008-30092

The purpose of models is not to fit the data but to sharpen the questions.

—Samuel Karlin

# Table of Contents

# List of Figures

# List of Tables

# List of Abbreviations

MC: Monte Carlo

MD: molecular dynamics

NAC: nonamyloid component

FKBP: FK506 binding proteins

PPIase: peptidyl−prolyl isomerase

REMD: replica exchange MD

GB/SA: generalized Born/surface area

B3LYP: Becke's 3−parameter hybrid functional
using the Lee−Yang−Parr correlation functional

TS: transition state

IRC: intrinsic reaction coordinate

RMSD: root means square deviation

WT: wild type

COM: center of mass

SASA: solvent accessible surface area

Rg: radius of gyration

A$\beta$: amyloid $\beta$

APP: amyloid $\beta$ precursor protein

IDP: intrinsically disordered protein

BFGS: Bryden−Fletcher−Goldfarb−Shanno

NEB: nudged elastic band

MP2: the $2^{nd}$ order Møller−Plesset perturbation theory

DFT: density functional theory

HF: Hartree Fock

RESP: restrained electrostatic potential

GAFF: generalized amber force field

RMSF: root means square fluctuation

RDF: radial distribution function

MO: molecular orbital

# 0. Overviews

Proteins and nucleic acids are the primary elements in cellular machinery. Knowledge of the structure, dynamics, and functions of such molecules could enhance the understanding of phenomena in living organisms. In addition, this understanding could contribute to the regulation of natural phenomena, such as disease. It's advantageous to study the structure and dynamics of these molecules for the better insight on their biological function.

Proteins are biological macromolecules made up of amino acids residues. An amino acid consists of a central carbon atom bound to a carboxyl group, an amine group, a hydrogen, and 20 unique side chains. The amino acids are linked into a chain through amide bonds (or peptide bonds).

The sequence of amino acids in a protein is called as the primary structure which determines its characteristics in its environment. Three types of atoms (amide nitrogen, alpha carbon, and carbonyl carbon) are repeated along the chain. The rotation about the bonds between these atoms is very stiff and thereby dictates the peptide bond. Based on these rotational angles, the secondary structures are classified into the alpha-helix, the $\beta$ sheet and the turn. The secondary structure could be illustrated in a two-dimensional histogram in backbone dihedral angle space, called Ramachandran plot.

Furthermore, the tertiary structure of a protein is the relative arrangement of the secondary structure segments. Lastly, the quaternary structure is the arrangement of multiple protein chains.

Although experiments can acquire accurate and essential structural data, there are limitations. However, simulations offer a representation of systems whenever the atomic detail is necessary. Quantum ab-initio methods represent every atom of a molecule with accurate knowledge of the instantaneous electronic state. While a coarse-grained model represents a molecule as a chain of subunits. The caveat is that the increasing computational cost comes with increasing detail of the system. For large systems, electronic detail is intractable. For certain size of system, there is a limit, based on the computational cost and how much detail can be given.

The all-atom representation of proteins is between the quantum mechanical and the coarse-grained descriptions in both accuracy and speed. In the all-atom method, individual atoms interact with each other via both bonded and nonbonded energy terms: in the amber force field,

$$V(r^N) = \sum_{bonds} \frac{1}{2} k_b (l - l_0)^2 + \sum_{angles} \frac{1}{2} k_a (\theta - \theta_0)^2 + \sum_{torsions} \frac{1}{2} V_N [1 + cos(n\omega - \gamma)] + \sum_{j=1}^{N-1} \sum_{i=j+1}^{N} \left\{ 4\epsilon_{i,j} \left[ \left( \frac{\sigma_{i,j}}{r_{ij}} \right)^{12} - 2 \left( \frac{\sigma_{i,j}}{r_{ij}} \right) \right] + \frac{q_i q_j}{4\pi\varepsilon r_{ij}} \right\}$$

The first two terms represent bond stretching and rotation as springs. The third term represents dihedral angle. The double sum represents nonbonded interactions. The potential energy for each molecular system will have a unique set of terms according this equation.

Although all-atom simulations offer the detail about the structure of biological molecules, there are several flaws. The representation can be wrong if the parameter set for the force field is incorrect. There is a fundamental difference between the force field and the real system. Moreover, the simulation trajectory doesn't reflect the correct population proportionality between relevant states with accuracy.

The free energy difference between two states is related to the relative ensemble populations of those states. According to the ergodic hypothesis, these populations can be obtained by fully sampling either phase space or time. These populations can be the state populations among many particles or the state

probability of a single particle at any time. Thus, correct populations can be attained by fully sampling either phase space or time. Additionally, correct expectation values can be obtained via complete sampling of either phase space or time.

The duality of phase space and time lends to two approaches to sampling: Monte Carlo (MC) and molecular dynamics (MD). In MC the phase space sampling approach is used. A series of configuration are collected after extensive propagation via attempting configurational changes based on the transition probability between the past and the future states. The transition probability can be derived from the probability factor and the detailed balance condition. There is no formal requirement for the nature of any MC moves other than that the reverse should be possible. An advantage of MC over MD is that the MC moves may be chosen so that they allow system to move between two states irrespective of any energy barriers between them. A particular flaw to the MC approach is that sequential moves are not chronologically linked.

The MD approach uses integration over time to determine free energy landscape. In MD, systems are propagated by Newton's second law. The force on any particle is determined by the negative gradient of the potential and the equation of motion is established and solved numerically. Successive moves describe a movie-like representation of the system. After sufficient

propagation, accurate probabilities can be extracted by integrating over the snapshots.

A particular shortcoming to the MD approach is a kinetic trapping. In other words, if the system is inside a deep free energy valley, successive integration will sample the same space. This makes the computational cost of a converged simulation intractable.

The free energy of proteins are very complex. There are huge degrees of freedom and a large amount of possible configurations. There is often the unique configuration that allows proteins to perform their biological functions. On average, proteins consist of on the order of 100 amino acids. Each residue can sample its own dihedral angle space. Thus, for the entire protein, there should be $\sim 10^{50}$ conformational states available. If the protein were to sequentially sample each conformation at a rate similar to the experimental transition rate, it would take about $10^{38}$ seconds to completely sample configurational space. Experimental folding rates on the order of seconds or less and thereby it contradicts. C. Levinthal introduced this contradiction and suggested that proteins gradually move in the general direction of the folded state due to the local gradient of the potential energy surface from an unfolded configuration.(*1*)

Conformational sampling is an essential concern to the study of proteins. A major obstacle for the correct sampling is that the

potential energy surfaces of proteins are very rugged and contain huge number of local energy minima.(*2*) This causes a kinetic trapping in constant temperature MD. In order to overcome the kinetic trapping, multicanonical (*3*), simulated tempering(*4*), and parallel-tempering methods(*5*) are often utilized.

# I. Intrinsically Disordered Proteins

## I-1. α-Synuclein Proteins

### I-1-(1) Introduction

Parkinson's disease is characterized by the degeneration of dopaminergic neurons in the substantia nigra. One of the key proteins in Parkinson's disease is α-Synuclein.(*6, 7*) In the dopaminergic neurons of Parkinson's disease patients, the fibrillar form of α-Synuclein constitutes the main protein component of the characteristic cytoplasmic aggregates called Lewy bodies.(*8, 9*) Also, mutations in α-Synucleins that are responsible for rare inherited forms of Parkinson's disease accelerate the aggregation of the protein.(*10, 11*)

α-Synucleins have 140 amino acids and consists of three domains (the membrane binding, the nonamyloid component (NAC), and the acidic domains), and is intrinsically disordered protein that aggregates into a fibrillar β-sheeted structure under pathological conditions.(*11-13*) The central NAC domain mainly consists of hydrophobic residues and confers its propensity for the aggregation.(*13*) The acidic domain has ubiquitous carboxyl acids in its region.(*13-16*)

The aggregation of α-Synucleins into amyloid fibrils is a nucleation-dependent process with an initial lag phase, an elongation step and a steady-state phase.(*16*) In the lag phase,

the nucleus of aggregation is formed. It has been suggested that this nucleus is an α-Synuclein dimer.(*16*) The nucleation step involves the formation of a partially folded intermediate(*17*) and thereby is a difficult and a slow processes. Once a nucleus is established, the aggregates grow up rapidly until a thermodynamic equilibrium between aggregates and monomers is reached.(*18*) During the whole process, α-Synuclein folds and forms the secondary structure containing predominantly antiparallel β-sheets.(*19*)

The lag phase of the α-Synuclein aggregation is reduced *in vitro* in the presence of FK506 binding proteins (FKBP).(*20, 21*) FKBPs are members of the immunophilins, enzymes that bind immunosuppressive drugs and have a peptidyl-prolyl isomerase (PPIase). The PPIase activity speeds up the cis-trans isomerization of the proline residue, the process which has high activation energy barriers and is usually the rate-limiting step in protein folding.

FK506 binds to most FKBPs and is a potent and specific inhibitor of the PPIase activity.(*20, 21*) Several immunophilin ligands such as FK506 and members of the FKBP family have been associated with Parkinson's disease before.(*22*) Some studies have ascribed neuroregenerative and neuroprotective properties to immunophilin ligands in cell culture and in different rodent models.(*23*) Of FKBPs (FKBP12, FKBP52, FKBP65, and

FKBP38), FKBP12 is colocalized with α-Synuclein in lewy bodies and lewy neutrites(*24*), and both FKBP12 and FKBP52 are upregulated in surviving neurons following brain damage in rats(*25*).(*21*) Several studies have shown that the neurotrophic activity of FK506 is mediated by the interaction with FKBP.(*26-29*) Although many studies show some progresses, no conclusive answer has been provided so far, but the data suggest that the PPIase may play a role in the neurodegeneration.

Some studies have shown that α-Synuclein suppresses the aggregation of thermally denatured alcohol dehydrogenase and chemically denatured insulin, A53T mutant of α-Synuclein was able to inhibit the aggregation of insulin, and the chaperone-like activity of α-Synuclein was lost when the C-terminal residues from the $98^{th}$ to the $140^{th}$ were removed.(*14, 30, 31*)

Although the folding event of globular single-domain polypeptides occurs in the millisecond or the second time scales, it needs more time in the conformational conversion like the cis-trans isomerization reaction of the peptityl-prolyl bonds. Most peptide bonds are connected in the trans conformation during the biosynthesis at the ribosomes, and thereby is often found in nature. However, both the cis and the trans conformations of the peptidyl-prolyl bond are accessible in natural peptide backbones. Folding intermediates with such bonds are highly sensitive to the proteolytic degradation and aggregation, indicating that an

enzyme-catalyzed acceleration for the isomerization reaction of the proline residue may exist.(*32, 33*)

Going in more depth to the dynamics of α-Synucleins, it could make more precise understanding possible. Through the replica exchange MD (REMD) simulation method we report that the central role of the α-Synuclein as an intramolecular chaperone results from the restricted cis-trans isomerization of the proline residues in the acidic domain, and through the P-to-A mutation in the acidic domain the formation of the amyloid fibrils is accelerated, which is consistent with the experiment.(*34*)

## I-1-(2) Simulation Details

Monomers of residues 101-140 (the acidic domain) and 61-140 (the NAC and the acidic domains) from α-Synuclein were prepared under the modified generalize Born/Surface Area (GB/SA) model(*35-38*) and the amber force field 96(*39*) with modified hydrogen bonding radii over the leap module from Amber10™.(*40*) All the N-terminal and the C-terminal residues of monomers were acetylated ($CH_3CHO$-) and amidated (-$N(CH_3)_2$), respectively.

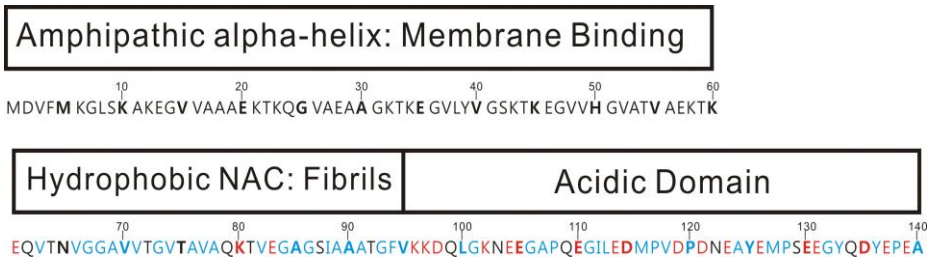


**Fig. I-1-1.** Primary structure of α-Synuclein protein, WT. In residues 61-140, blacks, reds, and blues symbolize the polar, the charged, and the hydrophobic residues, respectively.

Such prepared monomers were minimized with the steepest descent and the conjugate gradient algorithms(*41*), and heated up to 500 K in steps of 50 K over 150 ps with the weak-coupling algorithm.(*42*) After preparing several replicas (24 replicas for residues 101-140 and 34 replicas for residues 61-140 because residues 101-140 has 584 atoms and residues 61-140 has

1136 atoms, AP.I-1.) whose temperatures are made up of the geometric series in mathematics, all replicas were equilibrated at their respective temperatures.

For each equilibrated replica, the MD simulation independently took place for 400 fs, and then swapped their momenta based on the metropolitan criteria and those swapped velocities were re-scaled to be appropriate for swapped replicas. This cycle was iterated over all the MD simulation.(*43-45*) Distributions of potential energies of replicas were well overlapped and their swapping probabilities were ~0.6.

For the minimization, the equilibration, and the production MD of the system, the SHAKE algorithm(*46*) for fast moving hydrogens and the Langevin thermostat(*47*) (the collision frequency of 0.5 $ps^{-1}$) for controlling temperatures of replicas were applied. For the MD simulation under the acidic condition (pH=2), the constant pH calculation method(*48*) was employed.

For the energetic information of the cis-trans isomerization reaction, only the proline residue was geometrically optimized in the level of the B3LYP/6-31G(d)(*49, 50*) and confirmed to be in the stationary state by no imaginary frequencies. The transition state (TS) for the cis-trans conformational change was optimized in the STQN method, the TS optimization method based on the reactants and products that the transition structure connects. Through that computation, only one imaginary

frequency was obtained and the vibrational mode for the TS was reasonable for the cis-trans isomerization reaction. Moreover, it was verified as the reasonable structure through the intrinsic reaction coordinate (IRC) scan(*51*).

For all MD simulations and the quantum computations, the Amber10™(*40*) and the Gaussian03™(*52*) package programs were utilized, respectively. Initial structures for the MD were prepared with the Sirius package program.(*53*)

## I-1-(3) Results and Discussions

As time elapsed, monitoring for several monomers of α-Synucleins with full or some lengths to get aggregated could reveal deeper insight on the pathway to the amyloid fibrils. Unfortunately large molecular weights of α-Synucleins, 140 residues, could require huge computational resources and long computing time. However, the formation of the amyloid fibrils must proceed step by step and thereby the insight on the feature of a monomer could infer the expected progress of the aggregation.

Of 20 amino acids, only the proline residue gets the cyclic structure. This property can have played the important role in the biological function because the ring strain from the proline residue makes its conformational change restricted. Activation barriers for the cis-trans isomerization reaction of only the proline, ~12.4 kcal/mol, were obtained by the quantum computation (Figure I-1-2). Moreover, literatures have disclosed that the activation barriers for the cis-trans isomerization reaction of the peptidyl-prolyl proteins are ~30 kcal/mol.(*32*) These high barriers make the *in vivo* biological function related to the proline residues difficult, and thereby imply that some enzymatic activity is needed under the proline residue associated environment.

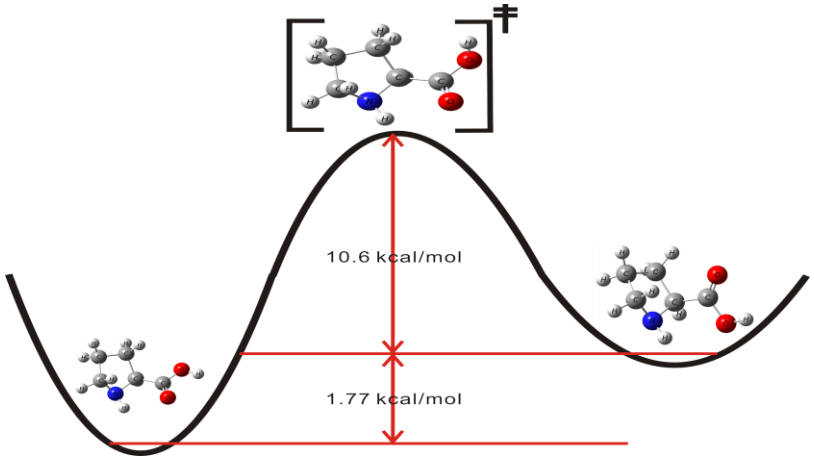


**Fig. I-1-2.** Energy profile for the cis-trans isomerization reaction for only the proline residue. Energies of the cis conformer are ~1.77 kcal/mol less than those of the trans conformer. Activation energies for the cis-trans isomerization reaction are ~12.4 kcal/mol and ~10.6 kcal/mol for the reverse reaction. All energies are corrected by their zero-point energies. Whites for hydrogens, grays for carbons, blues for nitrogens, and reds for oxygens. All the quantum computations were obtained on the level of B3LYP/6-31G(d) (*49, 50*).

The MD simulations for monomers and polymers were convergent based on the time evolution of the contents of the secondary structures and of RMSD, respectively. These two criteria showed the constant value converged as time evolved.

Although the contents of the antiparallel $\beta$ sheet in the NAC domain of WT were similar to those of P(108,117,120,128,138)A mutant, P(108,117,120,128,138)A mutant had higher contents of the antiparallel $\beta$ sheets in the acidic domain than WT irrespective of the acidity (Figure I-1-

3). However, the contents of the antiparallel $\beta$ sheets in the acidic domain significantly increased as the acidity decreased. It might imply that the removal of the rigidity from the proline residues might make the aggregates of P(108,117,120,128,138)A mutant more compact.

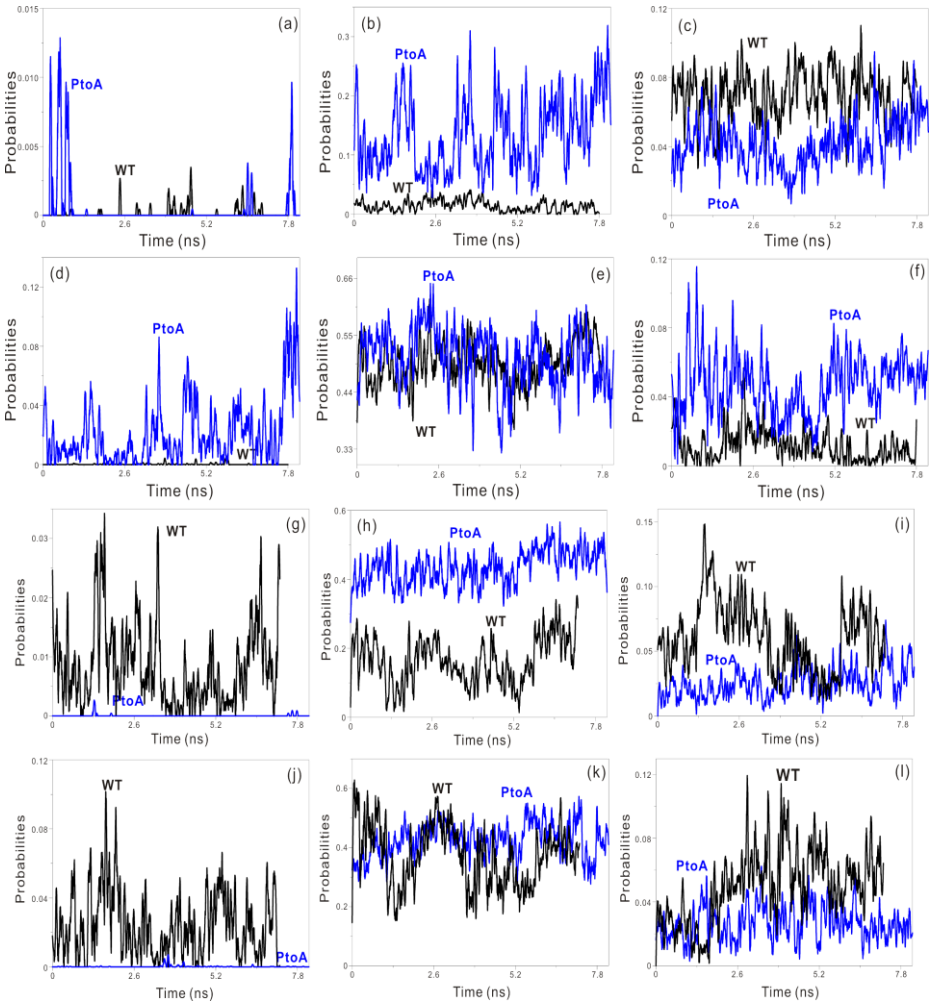


**Fig. I-1-3.** Time evolution of the contents of the secondary structures for WT of residues 61-140 at 300 K: (a) parallel $\beta$-sheet in the acidic domain at the neutral, (b) antiparallel $\beta$-sheet in the acidic domain at the neutral, (c) turn

in the acidic domain at the neutral, (d) parallel $\beta$-sheet in the NAC domain at the neutral, (e) antiparallel $\beta$-sheet in the NAC domain at the neutral, (f) turn in the NAC domain at the neutral, (g) parallel $\beta$-sheet in the acidic domain at the acidic, (h) antiparallel $\beta$-sheet in the acidic domain at the acidic, (i) turn in the acidic domain at the acidic, (j) parallel $\beta$-sheet in the NAC domain at the acidic, (k) antiparallel $\beta$-sheet in the NAC domain at the acidic, and (l) turn in the NAC domain at the acidic. P-to-A means P(108,117,120,128,138)A mutant.

In the respect of the distribution of distances between center of masses (COMs) for the NAC and the acidic domains at 300 K, WT at the neutral has the lowest distances (Figure I-1-4). In order for the aggregation to be enhanced one monomer should approach to aggregates or other monomer more easily. For the solvent accessible surface area (SASA), WT at the neutral has larger SASA than the other types (Table I-1-1). This implies that the NAC domain of the other types is more open to the environment than WT at the neutral, and thereby the other types of monomers are facilitated to bind to aggregates or other monomers.

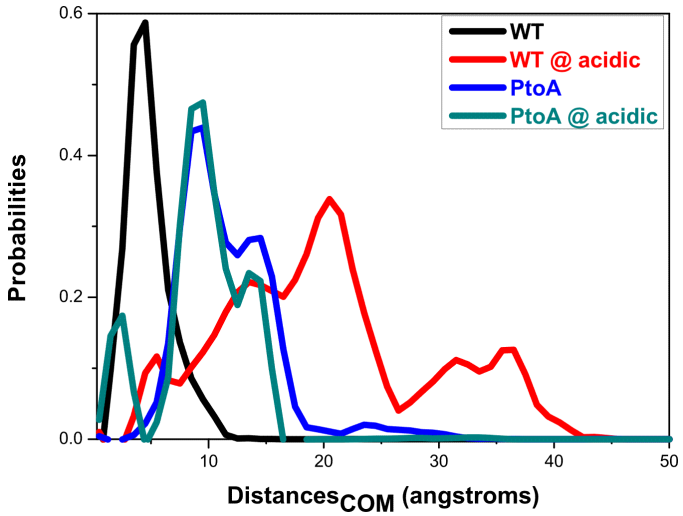


**Fig. I-1-4.** Distributions of COM distances between the NAC and the acidic domains for residues 61-140 in accordance with temperatures. Averages and standard deviations go like this: 4.95352(2.24154) for WT at the neutral, 20.28561(8.93399) for WT at the acidic, 11.76006(4.3553) for P(108,117,120,128,138)A mutant at the neutral, and 15.44856(3.98441) for P(108,117,120,128,138)A mutant at the acidic. Ordinates are probabilities. P-to-A means P(108,117,120,128,138)A mutant.

| Types | the NAC and the acidic domains | only the NAC domain |
|---|---|---|
| WT at the neutral | 6669.32425 (425.97991) | 2518.38852 (204.82135) |
| WT at pH=2 | 7243.20942 (407.43424) | 3231.6459 (396.09224) |
| P-to-A mutant at the neutral | 7174.01875 (350.49144) | 2925.17936 (163.23406) |
| P-to-A mutant at pH=2 | 6763.39858 (345.80606) | 3152.71329 (243.07813) |

**Table I-1-1.** Averages and standard deviations (parentheses) of SASA for

residues 61−140 at 300 K. For only the NAC domain, WT at the acidic has the 1.283 times open to the solvent than WT, P(108,117,120,128,138)A mutant at the neutral the 1.162 times, and P(108,117,120,128,138)A mutant at the acidic the 1.252 times. P−to−A means P(108,117,120,128,138)A mutant.

Since the carboxylic groups in the acidic domain should take the acidic form at the neutral, i.e., the deprotonated, they should get charged and thereby this makes the acidic domain hydrophilic. Moreover, this makes the acidic domain separated from the NAC domain as possible or wrap the NAC domain as the micelle shows at the neutral.(*14*)

However, under the acidic condition, the carboxyl groups should get the significantly decreased hydrophilic characteristics because they should take the basic form (the protonated form) and thereby the polar characteristics. This could result in the difficulty to be shuffled with the NAC domain which is hydrophobic.(*14*) In addition, the ring strain from the proline residues might make the NAC and the acidic domains difficult to be drawn more closely. As shown in representative conformers (Figure I−1−5 and I−1−6), the contents of the $\beta$ sheet for P(108,117,120,128,138)A mutant might be more or broader than for WT, and the acidic domains seem to wrap the NAC domain at the neutral and P(108,117,120,128,138)A mutant have more contents of the $\beta$ sheets per area than WT because of the released ring strains from the P−to−A mutation.

It implies that under the acidic condition the NAC and the acidic domains might be difficult to be mixed.

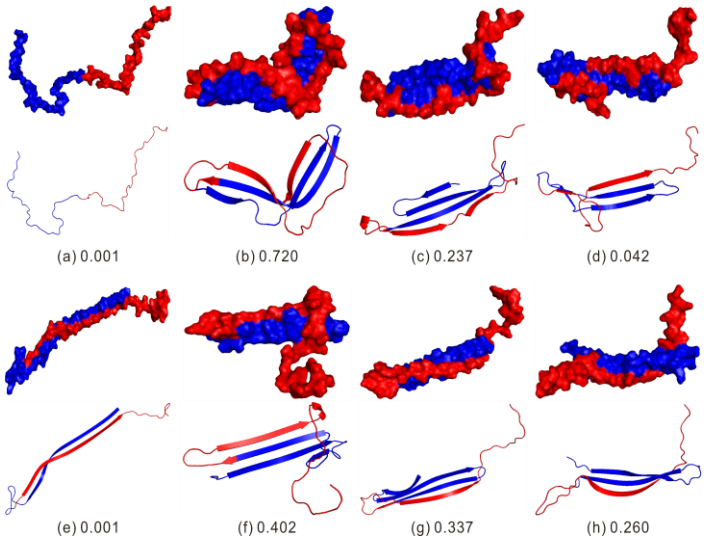


**Fig. I-1-5.** Representative conformers of residues 61-140 at 300 K and the neutral from clustering analyses based on the k-means algorithm(*54*): (a)-(d) for WT, (e)-(h) for P(108,117,120,128,138)A mutant. The reds display the acidic domains, the blues the NAC, and the numbers occurrence. The first rows are described as the surface representation and the second rows as the cartoon in each conformer. It might be reproduced as in the literature.(*14*)

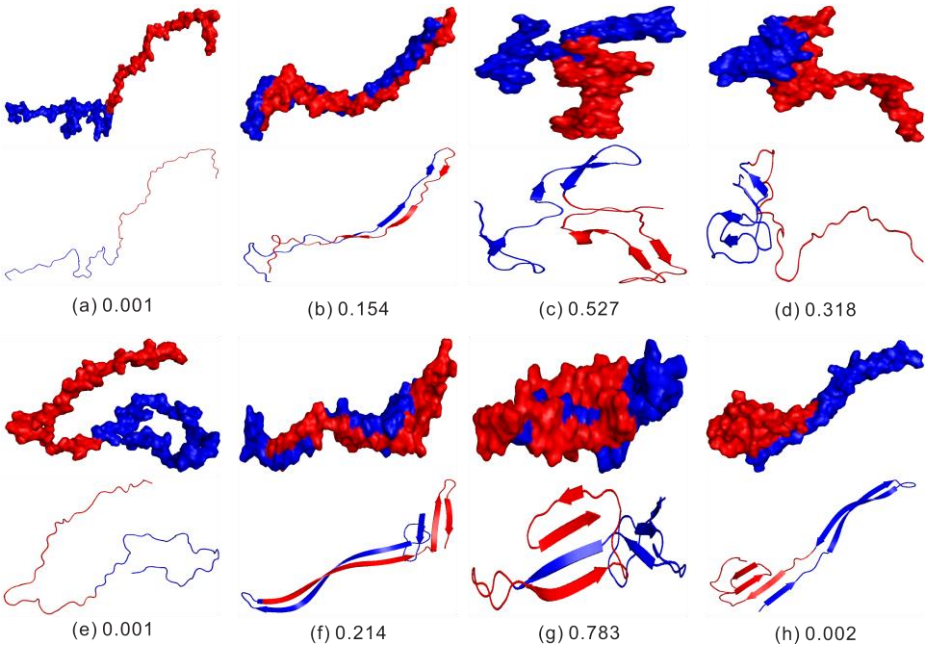


**Fig. I-1-6.** Representative conformers of residues 61-140 at 300 K and the acidic from clustering analyses based on the k-means algorithm(*54*): (a)-(d) for WT, (e)-(h) for P(108,117,120,128,138)A mutant. The reds display the acidic domains, the blues the NAC, and the numbers occurrence. The first rows are described as the surface representation and the second rows as the cartoon in each conformer. It might be reproduced as in the literature.(*14*)

Contact maps were obtained from the representative conformers (Figure I-1-7). Probabilities of 50 % or more was the highest for WT (Table I-1-2). The significant difference between WT and the others came from those probabilities (Figure I-1-8), and those residue pairs of WT were located to the middle of the NAC domain and the neighborhood of P128 in the acidic domain (Table I-1-3). Namely, P128 might get in touch with the middle of the NAC domain with higher

probabilities at 300 K and the neutral. This implies that one monomer of WT could have more difficulty to approach to other monomers or aggregates.

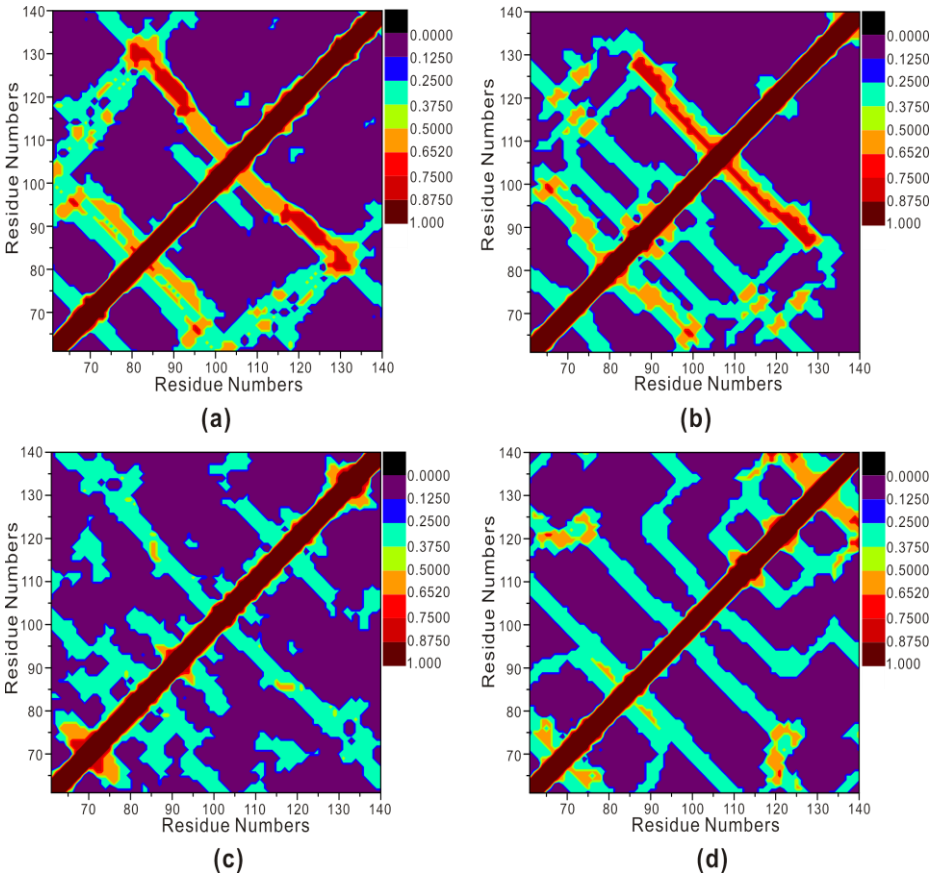


**Fig. I-1-7.** Contact maps for residues 61-140 at 300 K: (a) WT at the neutral, (b) P(108,117,120,128,138)A mutant at the neutral, (c) WT at the acidic, and (d) P(108,117,120,128,138)A mutant at the acidic. The distances within 12 Å are defined as "a contact".

| Types | Probabilities | | | |
|---|---|---|---|---|
| | 1.0 | 0.75 | 0.5 | 0.25 |
| WT at the neutral | 552 | 164 | 604 | 1334 |
| P-to-A at the neutral | 550 | 136 | 528 | 1662 |
| WT at pH=2 | 554 | 48 | 180 | 1954 |
| P-to-A at pH=2 | 552 | 38 | 356 | 1898 |

**Table I-1-2.** Numbers of residues pairs corresponding to their probabilities from contact maps for residues 61-140 at 300 K. P-to-A denotes P(108,117,120,128,138)A mutant.

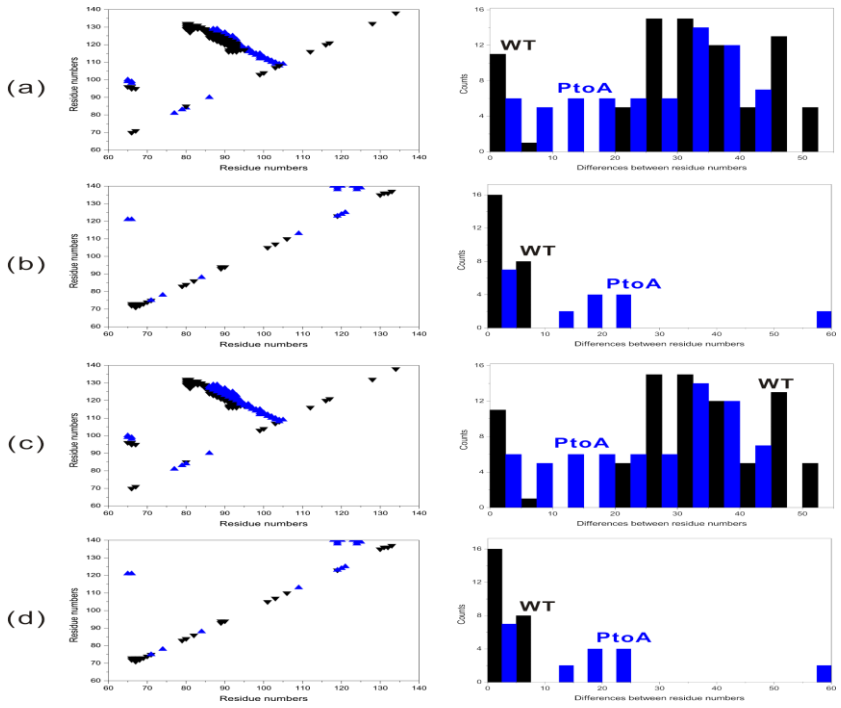


**Fig. I-1-8.** Pairs of residues within 12 Å and their histograms at 300 K for residues 61-140: (a) at the neutral and probability = 0.75, (b) at the acidic and probability = 0.75, (c) at the neutral and probability = 0.5, and (d) at the acidic and probability = 0.5. Since the order in the residue pairs is made not to

be distinguished for the simplification, the matrices are asymmetric. P-to-A denotes P(108,117,120,128,138)A mutant.

| | |
|---|---|
| 81 | 127,128,129,130,131,132 |
| 82 | 129,130,131 |
| 83 | 129,130,131 |
| 84 | 129,130 |
| 85 | 127,128,129 |

**Table I-1-3.** Residue pairs distinguishable in Figure I-1-8. Residues of the NAC domain are the median of the NAC and residues of the acidic domain are the neighborhood of the P128.

The nonpolar atoms were defined if the absolute values of their charges were less than 0.2 Coulomb and the polar atoms otherwise. Polar contacts for WT were greater than for P(108,117,120,128,138)A mutant without regard to the acidity and the difference was bigger under the neutral condition (Figure I-1-9). The rigidity from the proline residues could make the polar contacts increased, i.e., though the ring strain from the proline residues should make WT get in direct touch with other residues more difficultly, residues adjacent to the proline residues could make touches with the targeted residues increased as shown in Table I-1-2. Also, the acidity might dictate the degree of compactness. This implies that the NAC domain of WT at the neutral could get the least exposed to the

surrounding.

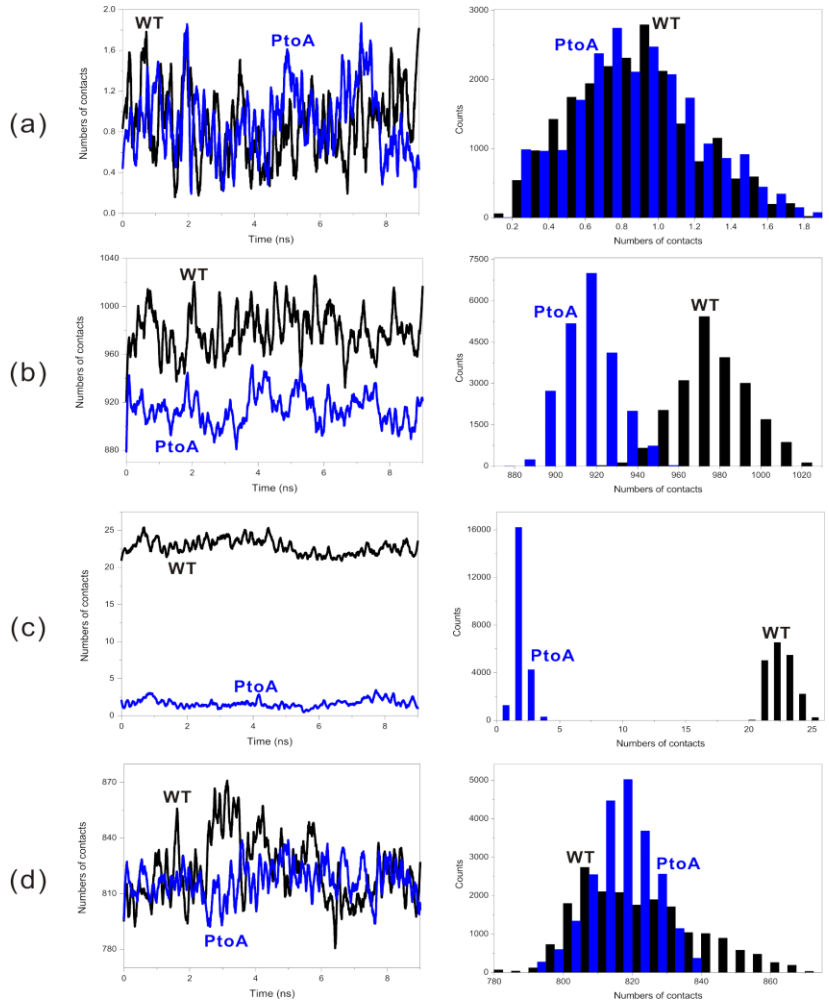


**Fig. I-1-9.** Time evolution of nonpolar/polar contacts for residues 61-140 at 300 K and their corresponding histograms: (a) at the neutral and nonpolar contacts, (b) at the neutral and polar contacts, (c) at the acidic and nonpolar contacts, and (d) at the acidic and polar contacts. P-to-A means P(108,117,120,128,138)A mutant.

Averaged Rg, <Rg> for residues 101-140 and residues 61-140 with respect to temperatures (Figure I-1-10) showed that

WT at the neutral had less slopes than for the other types. In addition, all types of residues 101-140 showed the linear dependence on temperatures but for residues 61-140, only P(108,117,120,128,138)A mutant showed the nonlinear one, which might result from the increased contents of the antiparallel $\beta$-sheets in the acidic domain for P(108,117,120,128,138)A mutant. Since such the increased contents of P(108,117,120,128,138)A mutant have the low probabilities (25%) (Figure I-1-7), the P-to-A mutation might make P(108,117,120,128,138)A mutant more flexible and more compact. The sensitivity of WT at the neutral to temperature was the least, and thereby this might imply the ability of WT to protect the NAC domain from the surroundings at the physiological condition.

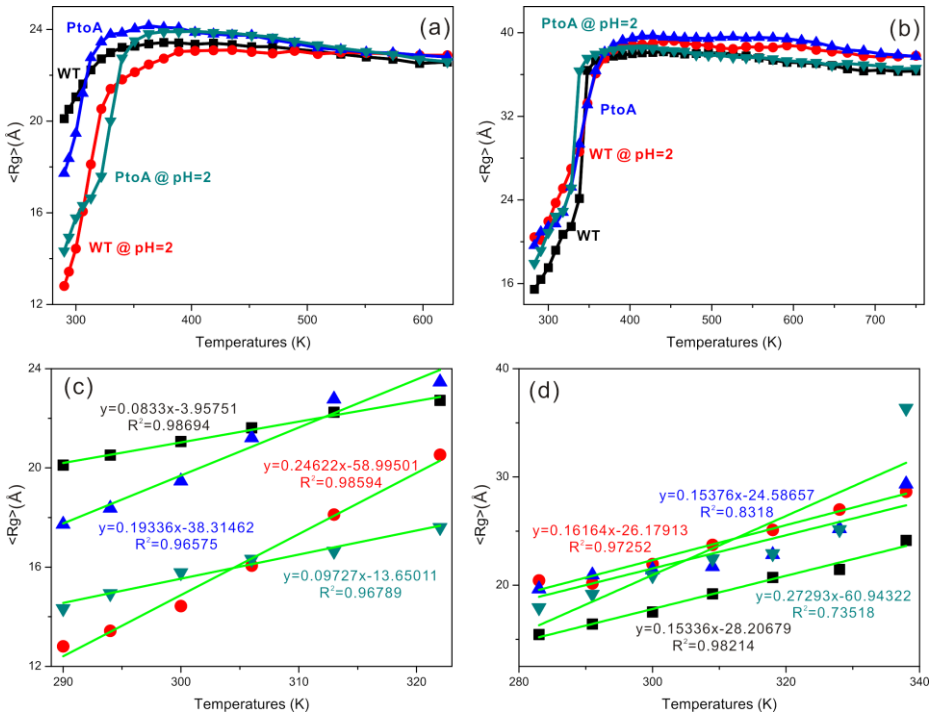


**Fig. I-1-10.** Averaged Rg, <Rg> in accordance with temperatures: (a) residues 101-140, (b) residue 61-140, (c) fitted curves for residues 101-140, and (d) fitted curves for residues 61-140. Green lines are fitted curves and P-to-A means P(108,117,120,128,138)A mutant.

Averaged polar contacts, <Polar contacts> (Figure I-1-11) displayed the trend that WT of residues 61-140 at the neutral had more sensitivity than the other types of residues 61-140, but WT of residues 101-140 more insensitivity than the other types of residues 101-140. In addition, under the acidic condition, P(108,117,120,128,138)A mutant might have two types of behaviors, which consisted of the slow and the fast ones. It might result from the fact that P(108,117,120,128,138)A mutant has more flexibility and compactness.

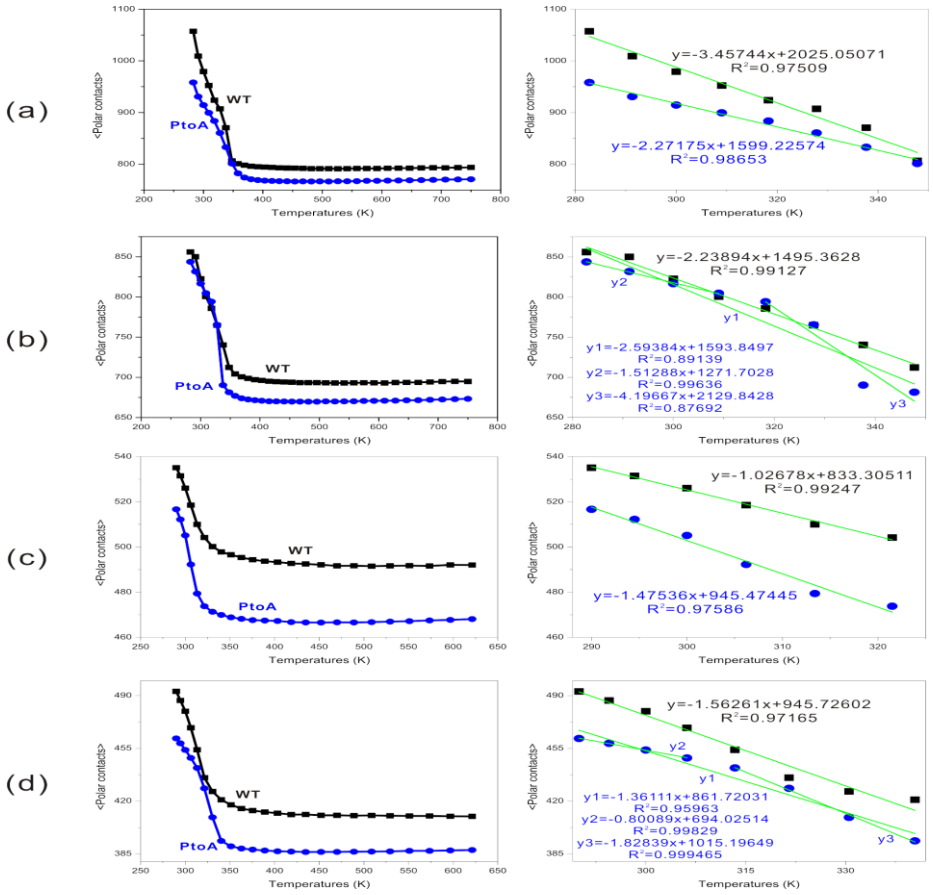


**Fig. I-1-11.** Averaged polar contacts, <Polar contacts> with respect to temperatures and their fitted curves: (a) residues 61-140 at the neutral, (b) residues 61-140 at the acidic, (c) residues 101-140 at the neutral, and (d) residues 101-140 at the acidic. Green lines are fitted curves and P-to-A means P(108,117,120,128,138)A mutant.

In summary, the protecting ability of the acidic domain to the NAC domain might get decreased as the P-to-A mutation proceeded or the acidity decreased.

## I-1-(4) Conclusions

We performed the MD simulation for several monomers under the various conditions with the parallel tempering method in order to identify the role of the proline residues in the formation of $\alpha$-Synuclein aggregates.

WT at the neutral could have the most insensitivity to temperatures than the other types. The rigidity of the proline residue might make the acidic domain get in touch with the NAC domain more difficultly. The acidic domain of P(108,117,120,128,138)A mutant would tend to wrap the NAC domain under the neutral condition but to get aggregated some distantly from the NAC domain under the acidic condition. Therefore, the NAC domain of WT might get less open to the surrounding and the formation of the amyloid fibrils could be suppressed.

In order for $\alpha$-Synuclein to be aggregated, the acidic domains should be more prone to unwrap the NAC domain when one $\alpha$-Synuclein approaches to other $\alpha$-Synucleins. Likewise, the acidic domain of P(108,117,120,128,138)A mutant should have less energies to unwrap the NAC domain both under the neutral and the acidic conditions. This results from the restricted cis-trans isomerization of the proline residues owing to their high activation barriers. This property might make the acidic domain play the role in the aggregation of $\alpha$-Synucleins as an

intramolecular chaperone (Scheme I-1-1).

The early onset of amyloid fibrils has been known to be very important in the pathway to the formation of the amyloid fibrils which consist of the nucleation and the elongation steps. Although the insight on the elongation of amyloid fibrils is not supplied, it is believed that the insight on the nucleation could be displayed.

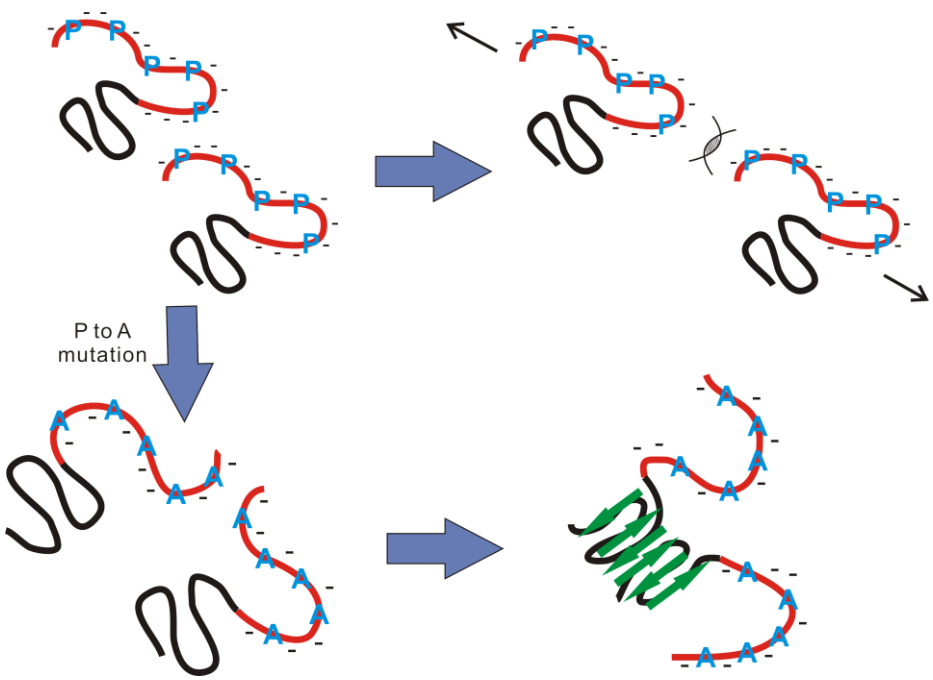


**Scheme I-1-1.** The proposed role of the acidic domain as the intramolecular chaperone in the formation of amyloid fibrils.

# I-2. Amyloid-β Proteins

## I-2-(1) Introduction

Of many neurodegenerative disorders, Alzheimer disease is the most general form of dementia. Although the cause and progression of Alzheimer disease are not well understood, several studies have shown that Alzheimer disease is associated with plaques and tangles in the brain, and those plaques and tangles are made up of amyloid β (Aβ) deposits(*55, 56*) which are secreted into the cytosol from an integral membrane protein, amyloid β precursor protein (APP) by several secretases(*57*).(*58*) The resulting amyloid plaques are toxic to nerve cells. The other protein implicated in Alzheimer's disease, tau protein, also forms such prion-like misfolded oligomers, and there is some evidence that misfolded Aβ can induce tau to misfolding.(*59, 60*) Similar plaques are found in some variants of Lewy body dementia(*61*) and in inclusion body myositis(*62*).

Although the secreted Aβ proteins have some positive functions *in vivo*,(*63, 64*) their faulty aggregation could raise Alzheimer disease. According to the amyloid cascade hypothesis, extracellular Aβ deposits have been known to be the fundamental cause of disease.(*55*) The secreted length of 40 or 42 are the most prevalent forms of Aβ deposits. Increases in either total Aβ levels or the relative concentration of both $A\beta_{40}$ and $A\beta_{42}$ have been implicated in Alzheimer's disease. The A

$\beta_{40}$ form is the more common of the two, but due to its more hydrophobic nature, the A$\beta_{42}$ is the most amyloidogenic form of the peptide, the more fibrillogenic, and thus associated with disease states. Mutations in APP associated with early-onset Alzheimer's have been notified to increase the relative production of $A\beta_{42}$, and thus one suggested the Alzheimer's therapy to produce mainly A$\beta_{40}$.(*65*) Moreover, Aβ could be destroyed by several amyloid-degrading enzymes including neprilysin.(*66*)

Some studies reported that the aggregation of monomeric to oligomeric A$\beta$ could be very important event in the formation of amyloid fibrils.(*67, 68*) And other studies showed that soluble oligomeric A$\beta$ could be more neurotoxic than the fibrillar form.(*69-71*) These toxic oligomers would bind to a surface receptor on neurons and change the structure of the synapse, thereby disrupting neuronal communication.(*72*) Since one receptor for A$\beta$ oligomers is thought to be the prion protein, the mechanism for Alzheimer disease is linked to the neurodegenerative disorders.(*73*) Such the aggregation of A$\beta$ oligomers could have been known to be proceeded in two steps, the nucleation and the elongation.(*74*) The nucleation steps could be the rate determining and the elongation go downhill in the energy landscape.

Although detailed structural information for A$\beta$ fibrils in the

atomic level had not been given until now, several studies showed that A$\beta$ fibrils has an in-register parallel $\beta$ strand structure and a steric zipper contact.(*75-79*) The central sequence KLVFF is known to form amyloid on its own, and probably forms the core of the fibril. Additionally, monomers of A$\beta_{40/42}$ have been known to get the $\beta$-turn-$\beta$ topology from the 11$^{th}$ residue to the C-terminal residue.(*79-82*) T.R. Serio *et. al.* showed that the formation of amyloid fibrils was accompanied with the conformational conversion.(*83*) Moreover, I. Bertini *et. al.* recently reported a new structural model of A$\beta_{40}$ fibrils from the X-ray crystallography.(*84*) Types of pairing between residues in the $\beta$-turn-$\beta$ topology for the protofilament and residues involved in steric zipper contacts between protofilaments made their model different from other models.

In the perspective of the energy landscape, folded proteins tend to exhibit a well-defined minimum energy state corresponding to the folded conformation but intrinsically disordered proteins (IDP) like A$\beta$ proteins lacks the deep potential energy minimum.(*85*) Since experimental studies for IDPs have many limitations because of this characteristics, the computational methods could be appropriate for the insight on IDPs.

Even for therapeutic purposes, more precise understanding of the structure and the dynamics of A$\beta$ protein seems needed.

Through the insight on intermediates with the REMD and the classical MD methods, we report that the terminally additional IA residues of A$\beta_{42}$ could play a role in the formation of A$\beta$ fibrils as "a facilitator", a conformational conversion happen and the interprotofilament contacts play an important role.

## I-2-(2) Simulation Details

### Monomers:

WTs of A$\beta_{40/42}$ (Figure I-2-1) were prepared under the modified GB/SA model(*35-38*) and the amber force field 96(*39*) with modified hydrogen bonding radii over the leap module.(*40*) All the N-terminal and the C-terminal residues of monomers were acetylated ($CH_3CHO$-) and amidated (-$NHCH_3$), respectively. And F(19,20)I/L mutants were prepared from their WTs by the point mutation method over the PyMol program(*86*). (Mutants could be prepared in the combination of the sed interpreter and the xleap(*40*), too.)

Such prepared monomers were minimized in the combination of the steepest descent, the conjugate gradient(*41*), and a limited-memory BFGS quasi-Newton algorithms(*87*), and heated up to 500 K in 50 K-step over 150 ps with the weak-coupling algorithm(*42*). After preparing 26 replicas (WT and F(19,20)I/L of A$\beta_{42}$ have 636 and 634 atoms, and WT and F(19,20)I/L of A$\beta_{40}$ 607 and 605 atoms, respectively, AP.I-2.) whose temperatures are made up of the mathematically geometric series, all replicas were equilibrated at their respective temperatures. For each equilibrated replica, the production MD simulation was performed, i.e. MD for all replicas independently took place over the Langevin thermostat(*47*) (the collision frequency 0.5 $ps^{-1}$)for 400 fs, and after swapped their

respective positions and momenta based on the metropolitan criteria, those swapped velocities were re-scaled to be appropriate for swapped replicas. This cycle was iterated over all the production MD simulation. Distributions of potential energies for replicas were well overlapped and swapping probabilities were ~0.6.

In addition, the REMDs for $A\beta_{11-40/42}$ (WT, F(19,20)I, and F(19,20)L mutants, Figure I-2-2) were performed as for $A\beta_{40/42}$, which was used for calculating the binding energies of the protofibrils from their constituent monomers. The protocols were followed as done in $A\beta_{40/42}$. Temperatures for replicas were extracted from those of $A\beta_{40/42}$, as necessary.

Polymers:

For monomers suggested by Tycko's and Bertini's groups (Figure I-2-2), the coordinates of the antiparallel $\beta$ sheets were adjusted, and connected by the β turn structure over the Sirius program(*53*) as suggested(*84*).

For the MD simulation, such prepared monomers were edited over the xleap module(*40*), and duplicated once, three, five, and seven times along the fibrillar axes to be dimers, tetramers, hexamers and octamers of the protofilaments, respectively.

For protofibrils, protofilaments were duplicated in orthogonal to the fibrillar axes to be dimers, tetramers, hexamers and

octamers, respectively.

Such prepared polymers of protofilaments and protofibrils were minimized in the combination of the steepest descent, the conjugate gradient, a limited-memory BFGS quasi-Newton algorithms(*87*), and heated up to 500 K in steps of 50 K over 150 ps with all C $\alpha$ s fixed using the weak-coupling algorithm(*42*) under the implicit solvation of water(*35-38*). Then, the equilibration and the production-MD were performed over the Berendsen thermostat(*42*) under 300 K and the implicit solvation of water (GB/SA)(*35-38*) without any positional restraints.

Nudged Elastic Band (NEB) method(*88, 89*):

The mutually corresponding couples of the Tycko's and the Bertini's were selected from the previously edited monomers and minimized with a limited-memory BFGS quasi-Newton algorithm(*87*), and heated up to 300 K for 20 ps using the weak-coupling algorithm(*42*) under the implicit solvation of water (GB/SA)(*35-38*). Then, the equilibration at 300 K was performed for 1 ns and the simulated annealing up to 500 K done for 300 ps. Then, the system cooled down in the 50 K step to 0 K in two stages. In the first stage, the system cooled down to 0 K for 120 ps, and maintained at 0 K for 1 ns in the second stage.

For the minimization, the equilibration, and the production MD

of the system, the Amber10$^{TM}$(*40*) was employed and the SHAKE algorithm(*46*) was applied over the equilibration and the production MD for fast moving hydrogens. The Berendsen thermostat(*42*) was employed for controlling temperatures in the equilibration and the production MD.


**Fig. I-2-1.** Primary structures of WT of A$\beta_{40/42}$ proteins.

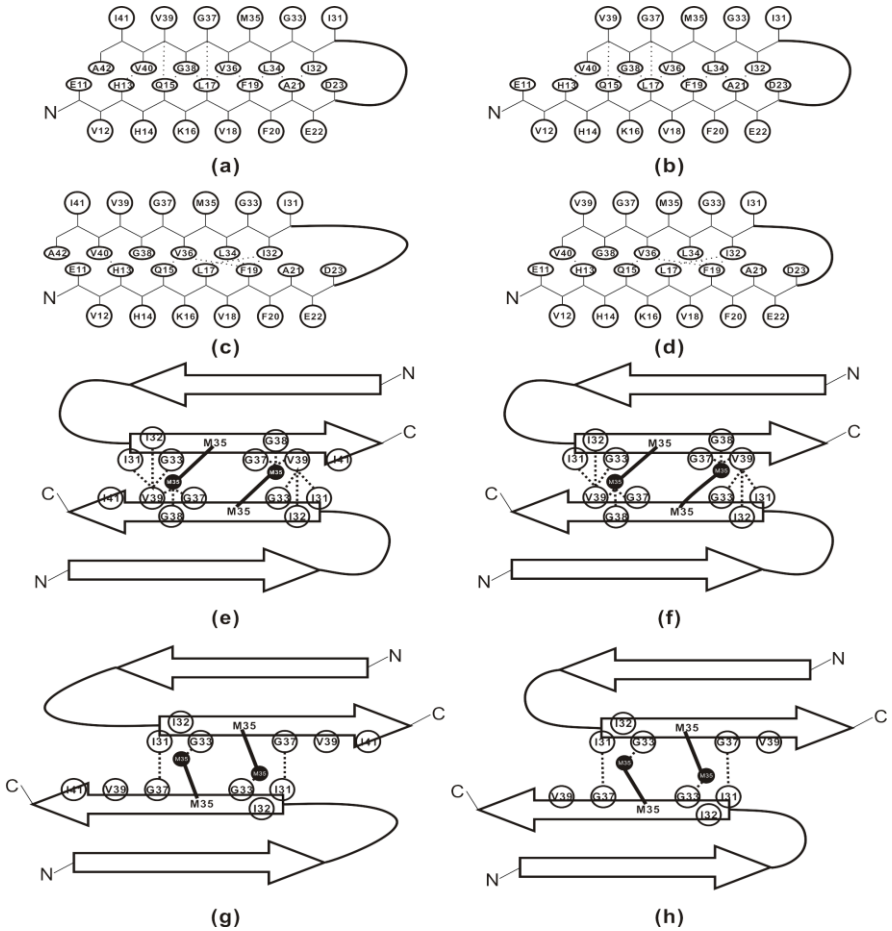

**Fig. I-2-2.** Initial structures of monomers (*84*): (a) the Bertini's model of A$\beta_{11-42}$ from protofilament, (b) the Bertini's of A$\beta_{11-40}$ from the protofilament, (c) the Tycko's of A$\beta_{11-40}$ from the protofilament, (d) the Tycko's of A$\beta_{11-40}$ from the protofilament, (e) the Bertini's model of A$\beta_{11-42}$ from protofibril, (f) the Bertini's of A$\beta_{11-40}$ from the protofibril, (g) the Tycko's of A$\beta_{11-40}$ from the protofibril, and (h) the Tycko's of A$\beta_{11-40}$ from the protofibril. Structures for A$\beta_{11-40}$ were prepared based on the Bertini's and the Tycko's works and A$\beta_{11-42}$ were made through linking the IA residues to the C-terminal of (b) or (d). In the fibrils, it has been known that the methionine residues might play the important role in the linkage of two protofilaments through the steric zipper contact.(*77-79*) Compared with the Tycko's model, more residues adjacent to the methionine residues in the Bertini's model participated in the formation of the steric zipper contact between two protofilaments.

## I-2-(3) Results and Discussions

The MD simulations for monomers were convergent based on the time evolution of the contents of the secondary structures and ones for polymers convergent based on the time evolution of RMSD (data not shown). Those two criteria showed the constant values converged as time elapsed. The $\beta$-turn-$\beta$ topologies were obviously displayed for monomers (Figure I-2-3).

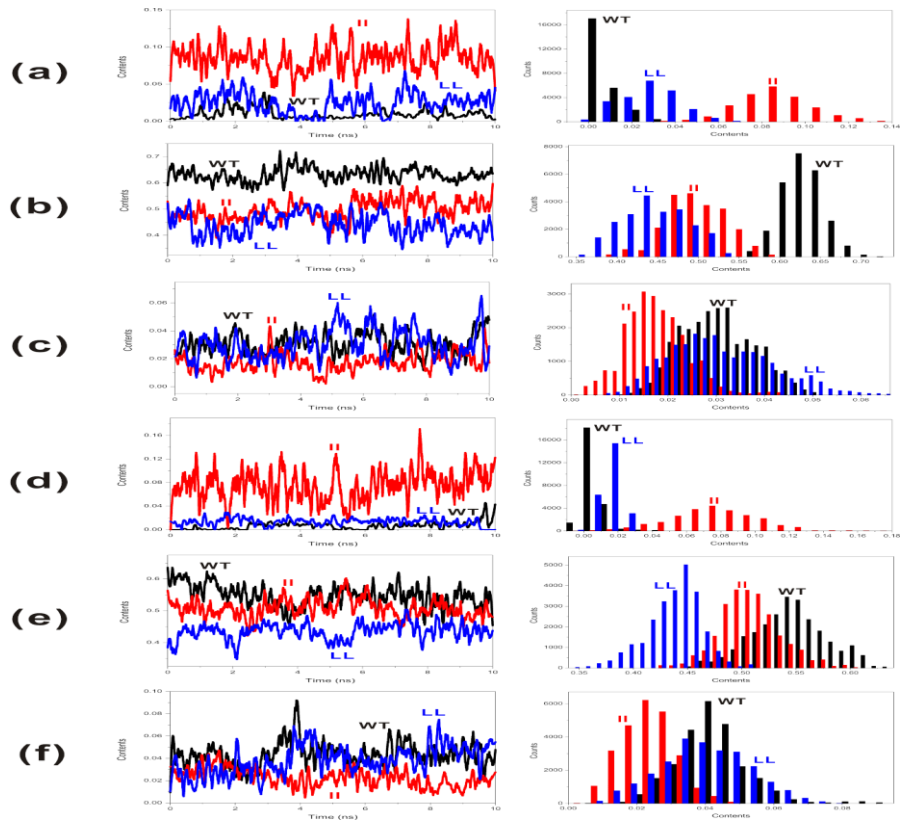


**Fig. I-2-3.** Time evolution of the contents of the secondary structures and their histograms for monomers of A$\beta_{40/42}$ at 300 K and the neutral: (a) parallel $\beta$-sheet for A$\beta_{42}$, (b) antiparallel $\beta$-sheet for A$\beta_{42}$, (c) turn for A$\beta_{42}$, (d)

parallel $\beta$-sheet for A$\beta_{40}$, (e) antiparallel $\beta$-sheet for A$\beta_{40}$, and (f) turn for A$\beta_{40}$. The II and the LL denote the F(19,20)I and the F(19,20)L mutants.

The amyloid fibrils of Aß should take various intermediates on the way to the aggregation.(*90*) Monitoring those intermediates over time could reveal invaluable insight on the pathway, but huge computing resources and long computing time could be required. However, through monitoring the stability of the expected intermediates on the way to the amyloid fibrils, the inference on the pathway could be revealed with shorter computing time because the formation of the amyloid fibrils must proceed step by step, i.e., via series of intermediates.

The N-terminal region (residues 1-10) could play a role in the formation of the amyloid fibrils, but its functionality has been controversial. For more insight on the pathway to the amyloid fibrils, the N-terminal regions were excluded in this work.

In general, the entropy has been measured in the unit of J/K and energies, such as an enthalpy, are orders of magnitude larger than the entropy. Furthermore, the entropy terms could be neglected in the enthalpy driven chemical reactions. In a condensed phase, such as a liquid or a solid, the change of the entropy could be negligible compared with a gas. Thus, the binding energy could be loosely defined as the potential energy changes for the chemical reaction in a condensed phase: $AB \leftrightharpoons A + B$. From its definition itself, the binding energy could be used

as the criterion for the structural stability.

The binding energies for the protofibrils of $A\beta_{11-42}$ from the Bertini's model showed some positive slopes, but ones from the Tycko's the constant values (Figure I-2-4). In forming 2-mer of the protofibrils of $A\beta_{11-42}$, the Tycko's model showed the positive binding energies but the Bertini's the negative. But in forming 4-mer of the protofibrils of $A\beta_{11-42}$, the Bertini's model got the jump on the Tycko's. Moreover, the binding energies for 4-mer of the protofibrils of $A\beta_{11-42}$ from the Tycko's model showed the negative values. When it is applied to the amyloid cascade hypothesis(*91*), the Tycko's model could be advantageous in the nucleation step and the Bertini's model in the elongation. However, $A\beta_{11-40}$ didn't show any obvious patterns.

Since binding energies don't depend on its pathway, the derivation from constituent monomers, not constituent protofilaments, could be calculated, too (Table I-2-1 and 2). Although the trends displayed the same patterns, it showed several significant findings. The F(19,20)I/L mutation revealed the significant effect in forming the protofibrils of $A\beta_{11-42}$, but the effect was limited to its 4-mer, which was believed to be the critical intermediate in the nucleation.

In addition, WT of $A\beta_{11-42}$ generally revealed larger slopes than those of $A\beta_{11-40}$ in forming the protofibrils without regards

to the structural models, and the Bertini's model of $A\beta_{11-42}$ showed the largest slope (Table I-2-2). Accordingly, the C-terminal added ile and ala residues of $A\beta_{11-42}$ could facilitate the formation of protofibrils. Moreover, larger binding energies (Table I-2-1) and higher contents of the secondary structures from protofibrils (Fig. AP.I-2-24~29) could be implied that the interprotofilament contacts would play an important role in forming the amyloid fibrils.

However, in forming the protofilaments, the Tycko's model showed the superiority to the Bertini's. In special, the Bertini's model of $A\beta_{11-42}$ might reveal the most insensitivity to adding its other monomers. The extra ile and ala residues in the C-terminal might exaggerate the formation of the protofilaments as shown in the protofibrils. Thus, the Tycko's model would be expected to dictate the formation of the protofilaments, which is consistent with the literature(*92, 93*).

RMSFs for the Tycko's model of $A\beta_{11-42}$ revealed more stable activity than the Bertini's in forming the protofilaments, but the Bertini's model more stable in the formation of the protofibrils. RMSFs for $A\beta_{11-40}$, irrespective of the Bertini's and the Tycko's models didn't show any obvious characteristics in forming both the protofilaments and protofibrils (Figure I-2-5).

Therefore, on the way to the formation of $A\beta_{42}$ fibrils, the Bertini's model could be advantageous in the elongation step and

the Tycko's in the nucleation, thereby indicating the conformation conversion as in the prion(*83*).

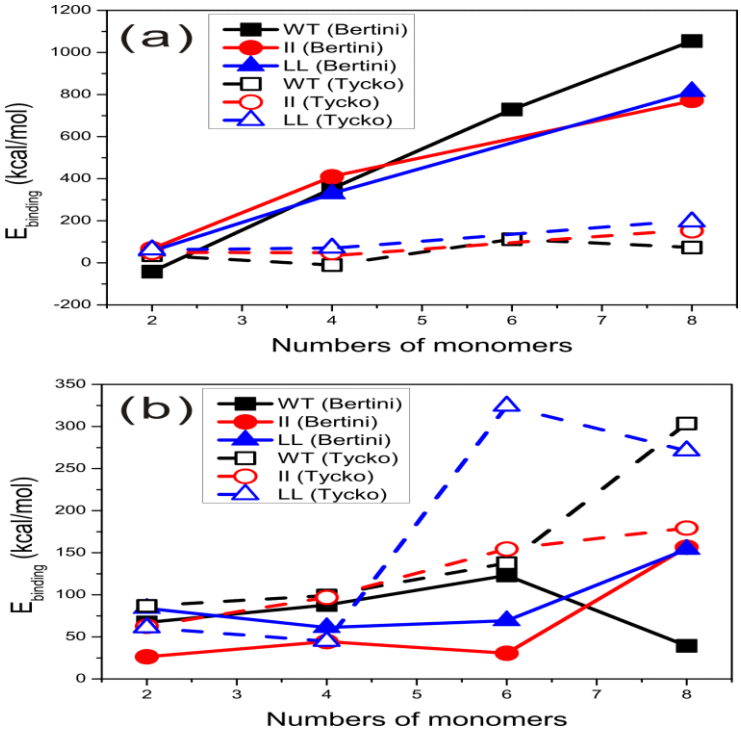


**Fig. I-2-4.** Binding energies for the protofibrils dependent on numbers of monomers at 300 K and the neutral: for (a) $A\beta_{11-42}$ and (b) $A\beta_{11-40}$. The II and LL denote the F(19,20)I and F(19,20)L mutants, respectively. Bertini and Tycko means the the Bertini's and the Tycko's model of Aβ, respectively. The binding energies are defined as the energy change for the reaction: the binding energies are defined as the potential energy difference of the chemical reaction, $A_2 \rightleftharpoons 2A$.

| Types | monomers | The Bertini's | | | The Tycko's | | |
|---|---|---|---|---|---|---|---|
| | | WT | II | LL | WT | II | LL |
| FB of $A\beta_{11-42}$ | 2 | 50.1387 | 113.3619 | 155.0771 | 89.03493 | 80.12882 | 132.3355 |
| | 4 | 358.1446 | 424.993 | 393.9386 | 271.6031 | 359.4989 | 350.9173 |
| | 6 | 728.6791 | n.a. | n.a. | 633.1044 | n.a. | n.a. |
| | 8 | 1091.286 | 960.5849 | 970.2293 | 954.7401 | 975.5861 | 1004.85 |
| FB of $A\beta_{11-40}$ | 2 | 111.9695 | 54.27372 | 103.2085 | 132.1447 | 80.68215 | 119.8877 |
| | 4 | 380.1059 | 333.1285 | 360.7375 | 343.5179 | 346.081 | 339.7906 |
| | 6 | 709.841 | 597.798 | 650.8093 | 643.4862 | 601.543 | 775.8724 |
| | 8 | 795.6517 | 867.2341 | 927.2336 | 987.3817 | 919.3421 | 1019.981 |
| FL of $A\beta_{11-42}$ | 2 | 45.90837 | 23.39792 | 49.56092 | 26.42383 | 15.29785 | 35.07203 |
| | 4 | 2.558817 | 7.7289 | 32.81798 | 141.2915 | 155.3336 | 140.4708 |
| | 6 | −0.2192 | n.a. | n.a. | 260.3909 | n.a. | n.a. |
| | 8 | 18.4587 | 94.224 | 77.998 | 441.0809 | 411.5998 | 404.7547 |
| FL of $A\beta_{11-40}$ | 2 | 22.3998 | 13.91765 | 9.6953 | 22.70483 | 9.074017 | 29.49072 |
| | 4 | 146.1069 | 144.3872 | 149.8239 | 122.1939 | 124.602 | 147.5097 |
| | 6 | 293.4258 | 283.6726 | 290.7483 | 252.9186 | 223.536 | 225.8428 |
| | 8 | 378.1735 | 355.4145 | 386.6554 | 341.9277 | 370.0328 | 374.3737 |

**Table I−2−1.** Binding energies of the protofibrils and protofilaments from monomers (kcal/mol): the binding energies are defined as the potential energy difference of the chemical reaction, $A_n \rightleftharpoons nA$. II, LL, FB, and FL denote F(19,20)I mutant, F(19,20)L mutant, protofibril, and protoflimanet, respectively. n.a.=not available

| Models | Types | $A\beta_{11-42}$ | | | $A\beta_{11-40}$ | | |
|---|---|---|---|---|---|---|---|
| | | Slope | y-intercept | $R^2$ | Slope | y-intercept | $R^2$ |
| FB of the Bertini's | WT | 174.6988 | −316.432 | 0.99756 | 119.0391 | −95.8034 | 0.93432 |
| | II | 140.1601 | −154.434 | 0.99701 | 135.1775 | −212.779 | 0.99984 |
| | LL | 137.0321 | −133.068 | 0.99605 | 138.1074 | −180.04 | 0.99923 |
| FB of the Tycko's | WT | 147.9308 | −252.534 | 0.97563 | 143.284 | −189.787 | 0.98377 |
| | II | 149.9256 | −227.915 | 0.99888 | 138.5721 | −205.948 | 0.99631 |
| | LL | 147.9997 | −194.631 | 0.98372 | 156.8181 | −220.208 | 0.97459 |
| FL of the Bertini's | WT | −4.2564 | 37.958 | 0.2699 | 60.732 | −93.634 | 0.9899 |
| | II | 13.207 | −19.85 | 0.7665 | 58.189 | −91.596 | 0.9832 |
| | LL | 5.676 | 26.971 | 0.5764 | 63.59 | −108.72 | 0.9927 |
| FL of the Tycko's | WT | 68.154 | −123.47 | 0.9867 | 54.42 | −87.162 | 0.9951 |
| | II | 65.767 | −112.84 | 0.9995 | 59.09 | −113.64 | 0.9937 |
| | LL | 62.251 | −97.07 | 0.9972 | 55.649 | −83.941 | 0.9867 |

**Table I−2−2.** Linearly fitted data for the binding energies of the protofibrils and protofilaments from monomers: II, LL, FB, and FL denote F(19,20)I mutant, F(19,20)L mutant, protofibril, and protofilament, respectively.

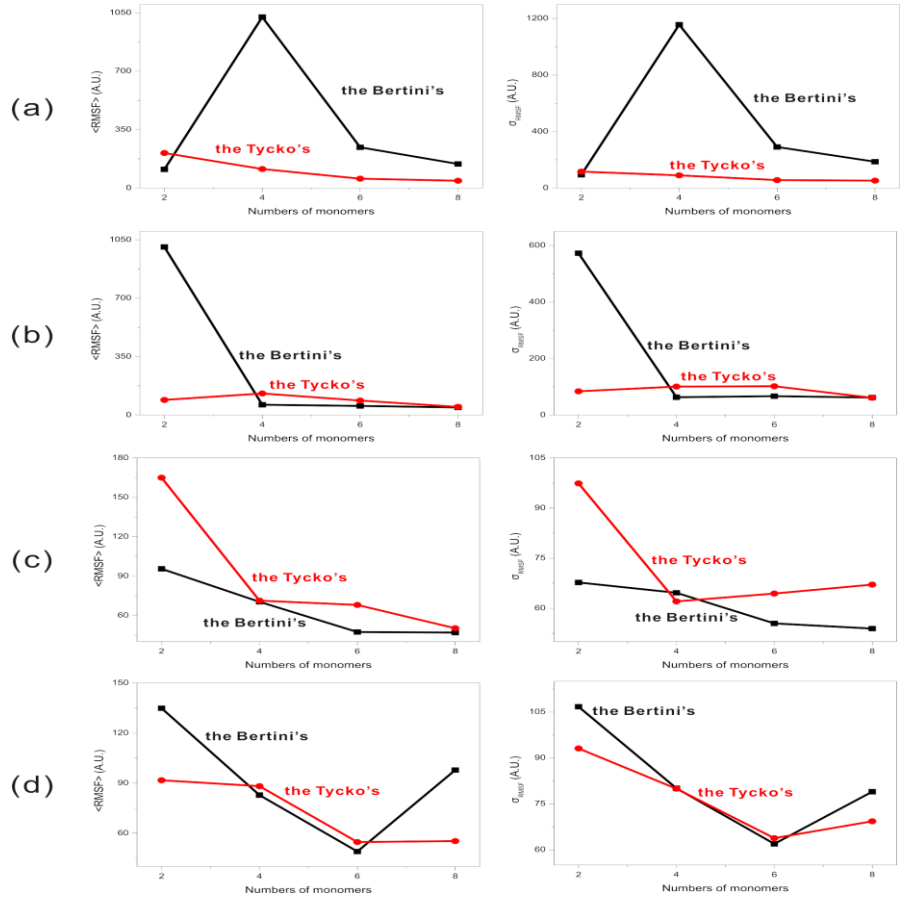


**Fig. I-2-5.** Averaged RMSF, <RMSF>, and their standard deviations dependent on numbers of monomers for the aggregation prone sequence (residues 16-20) of WT at 300 K: (a) protofilaments of A$\beta_{11-42}$, (b) protofibrils of A$\beta_{11-42}$, (c) protofilaments of A$\beta_{11-40}$, and (d) protofilbrils of A$\beta_{11-40}$.

By introducing the F(19,20)I/L mutation, the binding energies for 2-mer of the protofibrils from the Bertini's model of A$\beta_{11-42}$, and 4-mer of the protofibrils from the Tycko's model of A$\beta_{11-40}$ got changed to the positive values along their WTs. RMSFs for F(19,20)I/L mutant of A$\beta_{11-42}$ showed that it was more stable than WT in the formation of both protofilaments and

protofibrils up to the 4-mer (Figure I-2-6). But RMSFs for A$\beta_{11-40}$ didn't reveal any significant benefits in the formation of both protofilaments and protofibrils irrespective of the structural models (Figure I-2-7).

Therefore, the F(19,20)I/L mutation could make the formation of A$\beta_{42}$ fibrils more facilitated through the easier nucleation, but not of A$\beta_{40}$ fibrils.

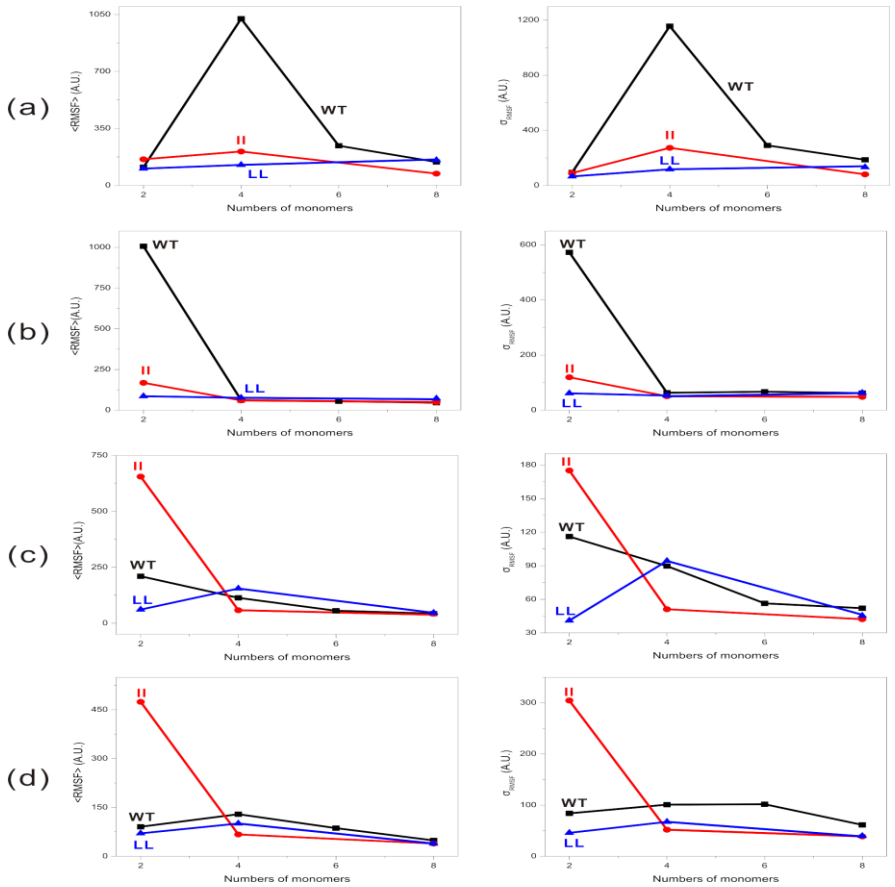


**Fig. I-2-6.** Averaged RMSF, <RMSF>, and their standard deviations dependent on numbers of monomers for the aggregation prone sequence (residues 16-20) of A$\beta_{11-42}$ at 300 K and the neutral: (a) protofilaments of the Bertini's

model, (b) protofibrils of the Bertini's, (c) protofilaments of the Tycko's, and (d) protofilbrils of the Tycko's. The II and LL denote the F(19,20)I and F(19,20)L mutants. The mutation effect shows with some certain.

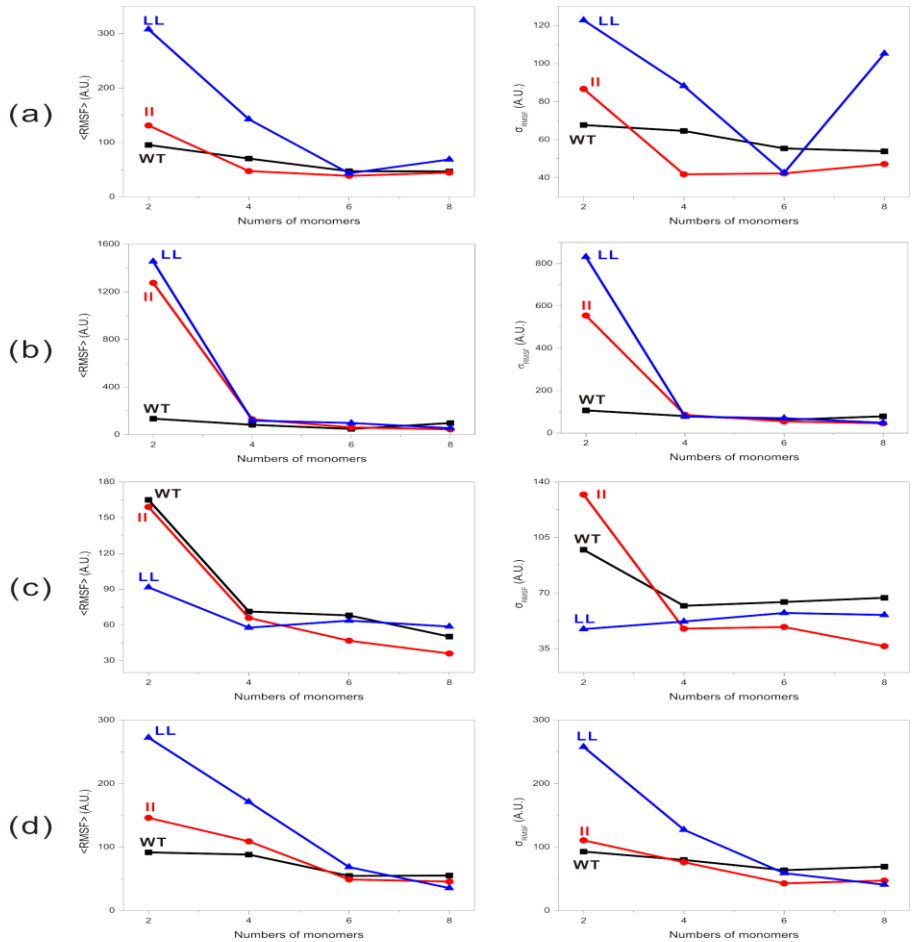


**Fig. I-2-7.** Averaged RMSF, <RMSF>, and their standard deviations dependent on numbers of monomers for the aggregation prone sequence (residues 16-20) of A$\beta_{11-40}$ at 300 K: (a) protofilaments on the Bertini's model, (b) protofibrils based on the Bertini's, (c) protofilaments based on the Tycko's, and (d) protofilbrils based on the Tycko's. The II and LL denote the F(19,20)I and F(19,20)L mutants. The mutation effect shows with no certain.

Representative conformers displayed the similar features

(Figure AP.I-2-6~29). WT of A$\beta_{42}$ from the Tycko's model has more precise contents of the $\beta$-turn-$\beta$ topologies than the Bertini's in the level of protofilaments. The F(19,20)I/L mutation might make those contents slightly increased in the formation of protofilaments from both the Bertini's and the Tycko's models compared with WT. However, WT of A$\beta_{40}$ didn't show the obvious discrimination between the Tycko's and the Bertini's models.

Potential energies of protofilaments from A$\beta_{11-42}$ showed the obvious discrimination between the Bertini's and the Tycko's models as numbers of constituents get increased (Figure I-2-8).

However, monomers of A$\beta_{11-40}$ might have less different potential energies, lower barrier energies, and more intermediates between the Tycko's and the Bertini's model than ones of A$\beta_{11-42}$, based on results from the NEB method(*88, 89*) (Figure I-2-9). Moreover, 2-mers showed more increased barrier energies and decreased numbers of intermediates (Figure I-2-10). The F(19,20)I/L mutation might make the trends more deepened for both monomers and 2-mers.

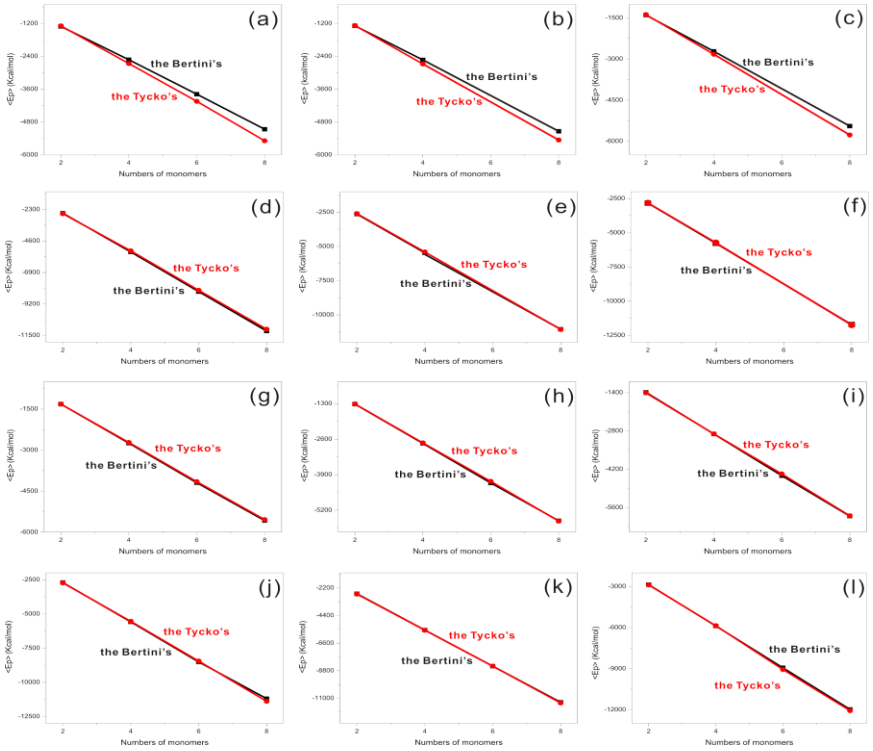


**Fig. I-2-8.** Potential energies dependent on numbers of monomers at 300 K and the neutral: (a) WT of A$\beta_{11-42}$ and protofilaments, (b) F(19,20)I mutant of A$\beta_{11-42}$ and protofilaments, (c) F(19,20)L mutant of A$\beta_{11-42}$ and protofilaments, (d) WT of A$\beta_{11-42}$ and protofibrils, (e) F(19,20)I mutant of A$\beta_{11-42}$ and protofibrils, (f) F(19,20)L mutant of A$\beta_{11-42}$ and protofibrils, (g) WT of A$\beta_{11-40}$ and protofilaments, (h) F(19,20)I mutant of A$\beta_{11-40}$ and protofilaments, (i) F(19,20)L mutant of A$\beta_{11-40}$ and protofilaments, (j) WT of A$\beta_{11-40}$ and protofibrils, (k) F(19,20)I mutant of A$\beta_{11-40}$ and protofibrils, and (l) F(19,20)L mutant of A$\beta_{11-40}$ and protofibrils. The II and LL denote the F(19,20)I and F(19,20)L mutants, respectively.

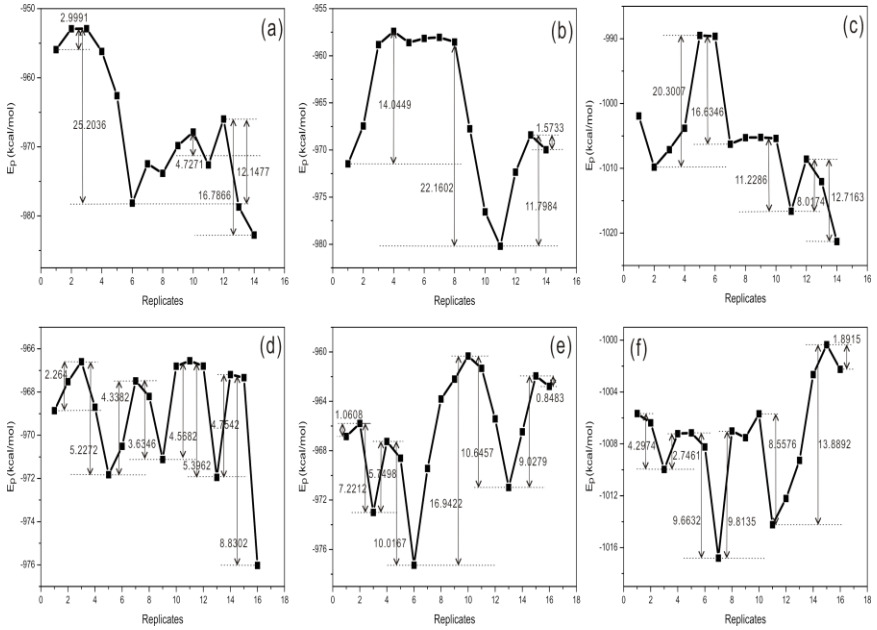


**Fig. I-2-9.** Profiles of potential energies for the monomeric transition from the Tycko's model to the Bertini's at 300 K based on the NEB method(*88, 89*): (a) WT of A$\beta_{11-42}$, (b) F(19,20)I mutant of A$\beta_{11-42}$, (c) F(19,20)L mutant of A$\beta_{11-42}$, (d) WT of A$\beta_{11-40}$, (e) F(19,20)I mutant of A$\beta_{11-40}$, and (f) F(19,20)L mutant of A$\beta_{11-40}$. The rightmost is the Tycko's model and the leftmost the Bertini's.

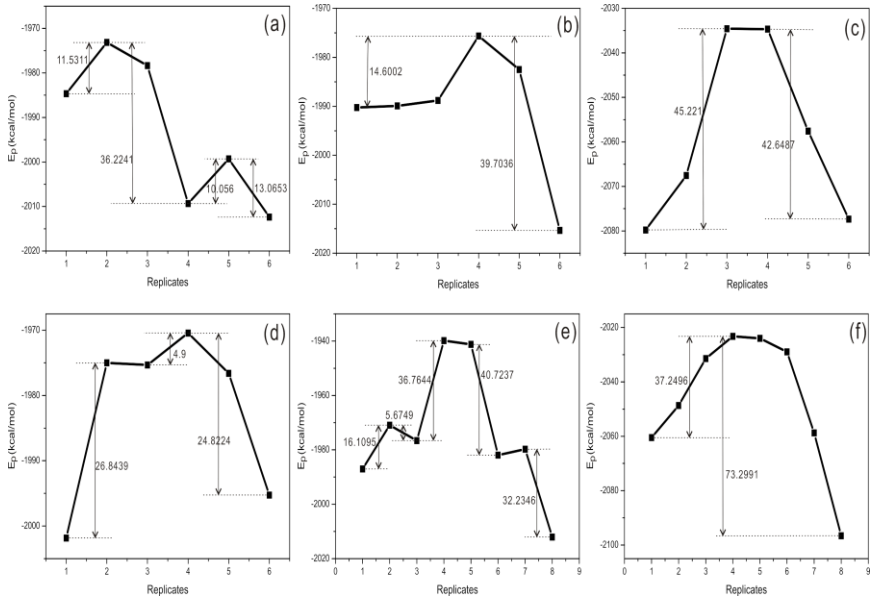


**Fig. I-2-10.** Profiles of potential energies for the dimeric transition from the Tycko's model to the Bertini's at 300 K based on the NEB method(*88, 89*): (a) WT of residues 11-42, (b) F(19,20)I mutant of residues 11-42, (c) F(19,20)L mutant of residues 11-42, (d) WT of residues 11-40, (e) F(19,20)I mutant of residues 11-40, and (f) F(19,20)L mutant of residues 11-40. The rightmost is the Tycko's model and the leftmost the Bertini's.

The nonpolar atoms were defined if the absolute values of their charges were less than 0.2 Coulomb and the polar atoms otherwise. Polar contacts for monomers of WTs from both $A\beta_{40}$ and $A\beta_{42}$ were greater than their mutants at 300 K (Figure I-2-11). It might result from higher contents of the secondary structures of WTs compared with their F(19,20)I/L mutants at 300 K (Figure I-2-3). In other words, since the phenylalanine residues have denser side chains (the phenyl rings) than the isoleucine or the leucine residues (saturated linear hydrocarbon

chains) and WTs have more contents of the secondary structures, polar contacts of WTs could be greater.

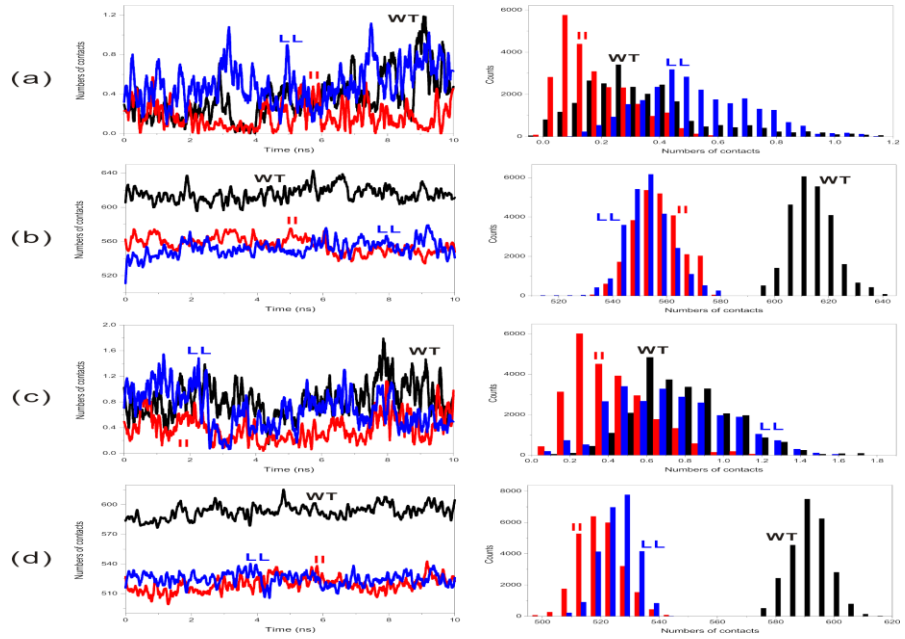


**Fig. I-2-11.** Time evolution of nonpolar/polar contacts for monomers at 300 K and the neutral: (a) nonpolar contacts for A$\beta_{11-42}$, (b) polar contacts for A$\beta_{11-42}$, (c) nonpolar contacts of A$\beta_{11-40}$, and (d) polar contacts for A$\beta_{11-40}$. The polar atoms are defined when absolute values of atomic charges are more than 0.2 and otherwise the nonpolar atoms defined. The II and LL denote the F(19,20)I and F(19,20)L mutants.

The linearly fitted data in Figure I-2-12 showed that the slopes for WTs were less than for F(19,20)I/L mutants in both A$\beta_{40}$ and A$\beta_{42}$. It might imply that the F(19,20)I/L mutation could make the sensitivity of monomers to temperatures increased. Moreover, the slopes for A$\beta_{42}$ were approximately two or three times greater than for A$\beta_{40}$ (Figure I-2-12 (e)

and (f)) and at least A$\beta_{40}$ might have two kinds of slopes, the slow and the fast responses to temperatures (Figure I-2-12). The addition of the isoleucine and the alanine residues to the N-terminal could be implied to make monomers of A$\beta_{42}$ significantly more sensitive to temperatures than monomers of A$\beta_{40}$. Therefore, monomers of A$\beta_{42}$ could play the better role in the aggregation than monomers of A$\beta_{40}$ whenever the nucleation or the elongation in the amyloid formation was proceeded, and thereby A$\beta_{42}$ oligomers might get more sensitive to temperatures than A$\beta_{40}$ oligomers, which might make the aggregation of A$\beta_{42}$ proceeded faster

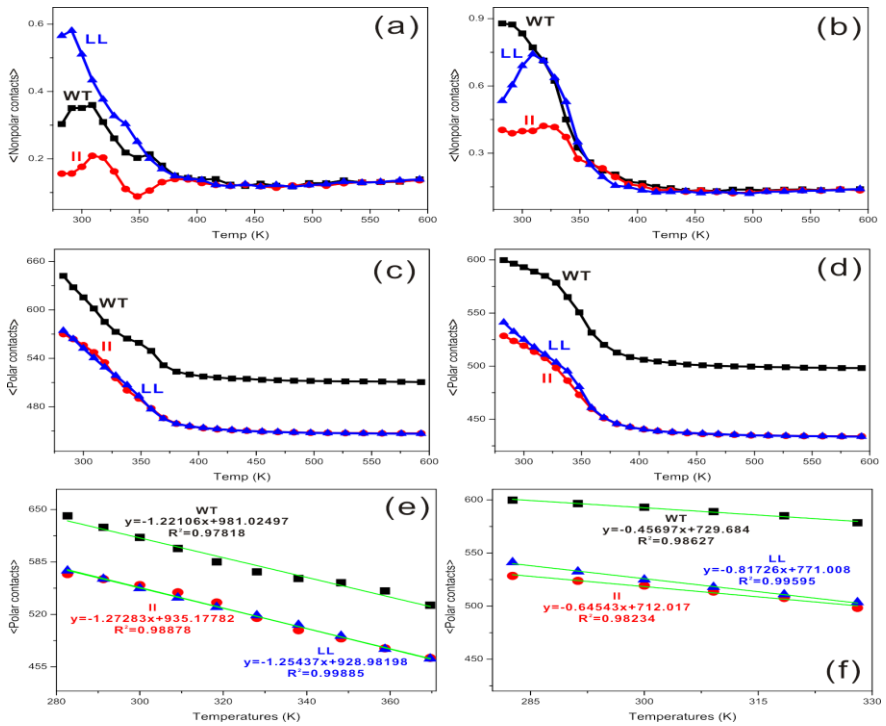


**Fig. I-2-12.** Averaged nonpolar/polar contacts, <Nonpolar/Polar contacts>,

dependent on temperatures for monomers: (a) nonpolar contacts for $A\beta_{11-42}$, (b) nonpolar contacts for $A\beta_{11-40}$, (c) polar contacts for $A\beta_{11-42}$, (d) polar contacts for $A\beta_{11-40}$, (e) fitted curves for (c), and (f) fitted curves for (d). Each value is averaged on its temperature. The II and LL denote the F(19,20)I and F(19,20)L mutants. Green lines are fitted curves.

Rgs showed the same characteristics as the polar contacts (Figure I-2-13). Rgs of $A\beta_{42}$ got more increased than ones of $A\beta_{40}$, and $A\beta_{40}$ had two kinds of characteristics as shown in polar contacts. WT of $A\beta_{42}$ obviously showed the mathematical inflection point but the F(19,20)I/L mutant didn't (Figure I-2-13 (a)). The slopes, i.e., the sensitivity to temperatures, for WTs showed the least values irrespective of the chain lengths of $A\beta$. This might imply that the F(19,20)I/L mutation make its sensitivity increased and lead to the facilitated conformation conversion.

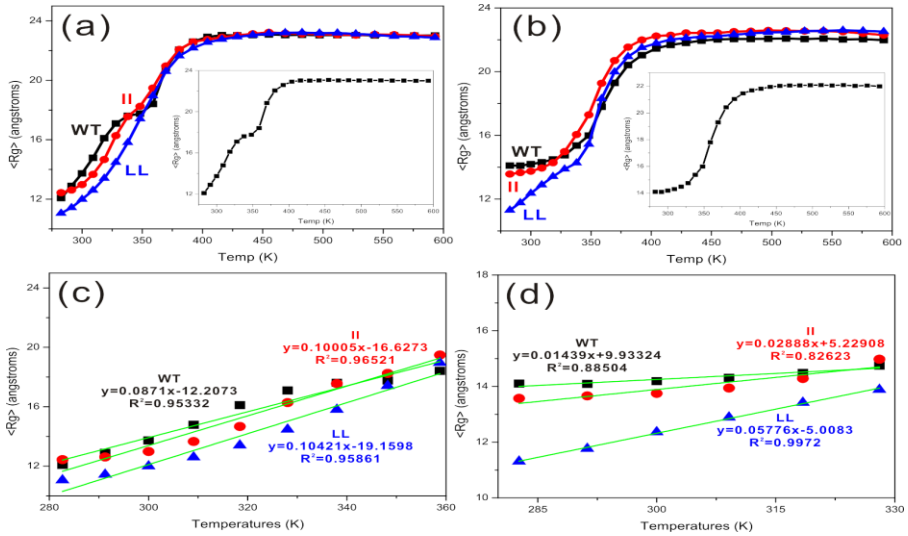


**Fig. I-2-13.** Averaged Rg, <Rg> dependent on temperatures: (a) A$\beta_{11-42}$, (b) A$\beta_{11-40}$, (c) fitted curves for (a), and (d) fitted curves for (b). Insets are for WTs. The II and the LL denote the F(19,20)I and F(19,20)L mutants.

## I-2-(4) Conclusions

We simulated the various A$\beta$ proteins under the physiological condition with the REMD and the classical MD simulation methods for the insight on the pathway to the aggregation of A$\beta$ proteins.

The pathway to the formation of the amyloid fibrils has been known to consist of the nucleation and the elongation steps.(*91*) Although the precise structures for the early onset of the aggregates have been controversial and not concrete until now, there are two popular models for monomers of A$\beta$ proteins, the Tycko's and the Bertini's which come from the crystallography for the final fibrils.

As for WT of A$\beta_{42}$, the Bertini's model showed the advantage in the elongation step of the pathway to the amyloid fibrils and the Tycko's model in the nucleation based on the binding energies of protofibrils. The F(19,20)I/L mutation could make the Bertini's model more adequate to the initial formation of aggregates. However, A$\beta_{40}$ didn't show the discriminated characteristics.

It is identified that the F(19,20)I/L mutation might make the polar contacts less frequent, the $\beta$-turn-$\beta$ topology more loosely, and numbers of intermediates suppressed. And it comes out that more dissimilar potential energies and higher barrier energies between intermediates of A$\beta_{42}$ could make the energy

landscape less rugged and the possibility led to the targeted fibrils increased.

The enhanced aggregation for $A\beta_{42}$ might result from the additional isoleucine and alanine residues, and thereby more prominent energy landscape caused by them, which might suggest the role of the extra residues of $A\beta_{42}$ in the formation of $A\beta$ fibrils as a facilitator. In addition, types of the steric zipper contact inner/into the protofilaments might reaffirm to play an important role in the pathway to amyloid fibrils.

Although we concern the implicit solvation of water, it could be believed not to swim against the tide.

# II. Bio-Mimicking Artificial Peptides

## II-1. Introduction

β-barrel peptides are usually observed in cytoplasmic and transmembrane proteins. Cytoplasmic proteins are soluble in water, but transmembrane proteins are insoluble and amphiphile. A green fluorescent protein is the best example of cytoplasmic proteins(*94*) and exhibits bright green fluorescence when exposed to light in the blue to ultraviolet range.(*95, 96*) Transmembrane β-barrel proteins are often found in the outer membranes of bacteria, mitochondria, and chloroplasts. Fewer than 20 three-dimensional β-barrel structures have been known until now, but genomic databases contain thousands of β-barrels.(*97*)

In the structural aspect, β-barrel is a closed structure which the first and the ended β-sheets in a polypeptide are linked by hydrogen bondings. And adjacent β-sheets in the β-barrel are generally arranged in the antiparallel mode. Noncovalent interactions plays an important role in the self-assembly phenomena and thereby delicately designed building blocks for the self-assembly should be one of major factors for the fabrication of the artificial bionanostructures.

Inspired by this natural organelle, many β-barrel mimicking peptides have been synthesized.(*98-101*) These artificial bionanostructures have shown the possibilities for constructing

artificial membrane pores or channels although their chemical compositions and structures are different from the nature.(*97*)

Artificial bionanostructures could mimic or exhibit much more enhanced functional properties for natural proteins and many cellular organelles. In addition, artificial bionanostructures were anticipated to show unparalleled characteristics in nature. For the construction of diverse artificial bionanostructures, designed synthetic self-assembly building blocks provide one of the most valuable candidates. In order to design optimal building blocks, one needs to understand the major driving force responsible for a noncovalent self-assembly process during the formation of a particular bionanostructures. If the pathway to the formation of the artificial bionanostructures like the $\beta$-barrels is known precisely, it could be greater breakthrough for the manipulation of the $\beta$-barrels. Unfortunately, experimental and theoretical studies could not arrive at the meaningful results yet.

Notwithstanding this misfortune, through the theoretical method, we will show major factors for designing the $\beta$-barrel mimic and suggest how to control the $\beta$-barrel.

## II-2. Simulation Details

### Polymers of T1:

A monomer of T1 (Figure II-1-(a)) was generated in the xleap module of AMBER™(*40*), and duplicated three, seven, eleven, and twenty three times to be 4-mers, 8-mers, 12-mers, and 24-mers. Orientations and distances between constituent backbones were controlled to be the structure of anti-parallel $\beta$-sheets over the Sirius program(*53*). All duplicates were minimized in the amber force field 96(*39*) and the combination of the steepest descent and the conjugate gradient algorithms(*41*), and heated up to 500 K in steps of 50 K over 150 ps with all C$\alpha$s fixed using the weak-coupling algorithm(*42*) in the implicit solvation of water (GB/SA)(*36, 37*) for the maintenance of their structures. Then, the equilibration and the production-MD were performed over the Berendsen thermostat(*42*) at 300 K without any positional restraints.

### Polymers of T3 and its mutants: oligoether dendron functionalized to the tyrosine (Y) residue of T1 and its mutants:

The oligoether dendron was capped with the N-terminal acetylation ($CH_3CHO$-) and the C-terminal amidation (-$NHCH_3$) capped tyr residue, and geometrically optimized in B3LYP/6-31G(d)(*49, 50*) (Fig. AP.II-5), because geometries in the library of the amber force field 96(*39*) are optimized in MP2/6-

31G(d) and the DFT(*102*) has been known to be comparable to the second order Møller-Plesset(*103*) perturbation.(*104, 105*) Electrostatic potentials were computed in HF/6-31G(d)(*106*) after its geometry optimization, and charges of the oligoether dendron were computed through the restrained electrostatic potential (RESP) procedure(*107, 108*) with the resp module of AMBER™(*40*). Charges of the capping groups (the acetyl and the amide groups), were supplied from the library of the amber force field 96(*39*) without any modifications. Any missing parameters were supplemented from the Generalized Amber Force Field (GAFF)(*109*). Such prepared charges and topologies were integrated into the amber force field 96(*39*) with the xleap module(*40*). Once a monomer of T3 (Figure II-1-(b)) was made in the xleap(*40*), it was replicated 11, 23, 39, 49 times to be 12-mer, 24-mer, 40-mer, and 50-mer. The orientations and the distances between constituent monomers were adjusted to be a closed anti-parallel $\beta$-sheets, i.e. nanoring, with the Sirius program(*53*). These replica were minimized in the amber force field 96(*39*) using a limited-memory BFGS quasi-Newton algorithm(*87*), heated up to 500 K, and the equilibration and production-MD were performed as done in T1.

Mutants of T3 were generated from WT of T3 by the point mutation, which was accomplished with PyMol(*86*). The minimization, the heating-up, the equilibration, and the

production MD of system were performed as done for WT of T3.

Monomers of T1, T3 and its mutants (W-to-F, and W(1,3,5)F mutants):

Monomers of T1, T3 and its mutants were reused, minimized in the combination of the steepest descent, the conjugate gradient(*41*), and a limited-memory BFGS quasi-Newton algorithms(*87*), and heated up to 500 K in 50 K-step over 150 ps with the weak-coupling algorithm(*42*). After preparing 24 replicas (maximum atoms are less than 350) whose temperatures are made up of the mathematically geometric series, all replicas were equilibrated at their respective temperatures. For each equilibrated replica, the production MD simulation was performed, i.e. MD for all replicas independently took place over the Langevin thermostat(*47*) (the collision frequency 0.5 $ps^{-1}$)for 400 fs, and after swapped their respective momenta based on the metropolitan criteria, those swapped velocities were re-scaled to be appropriate for swapped replicas. This cycle was iterated over all the production MD simulation. Distributions of potential energies for replicas were well overlapped and swapping probabilities were ~0.6. Mutants of T3 were generated from WT of T3 by the point mutation, which was accomplished with PyMol(*86*). Temperatures of replicas were extracted from those for α-

Synuclein as necessary (AP.I-1-(1)).

Polymers of the P series, P1, P1b, P1c, P2, and P3:

Tri(ethylene glycol) monomethoxy ether was capped with the N-terminal acetylation ($CH_3CHO-$) and the C-terminal amidation ($-NH_3$) capped tyr residue. Phenyldiazene ($C_6H_5-N_2$) was capped with the N-terminal acetylation and the C-terminal amidation capped phe residue.

The protocol for the derivation of the library information is the same as done in oligoether dendron functionalized to the tyrosine (Y) residue of T1. Gaussian09(*110*) was used for the quantum computation.

Polymers of T3 were used as the template for the preparation of the initial structures and the coordinates of the P series were adjusted with the Sirius(*53*). Such prepared initial structures were minimized in the AMBER force field 99SB(*111*), TIP3PBOX(*112*), and the combination of the steepest descent and the conjugated gradient algorithms(*41*), and heated up to 300 K with all C$\alpha$s fixed in the Langevin thermostat(*47*). The protocols for the equilibration and the Production MD were followed as done in T3 (*vide supra*). The W-to-F mutants were prepared as done in T3 (*vide supra*). All analyses were performed for last 1 ns.

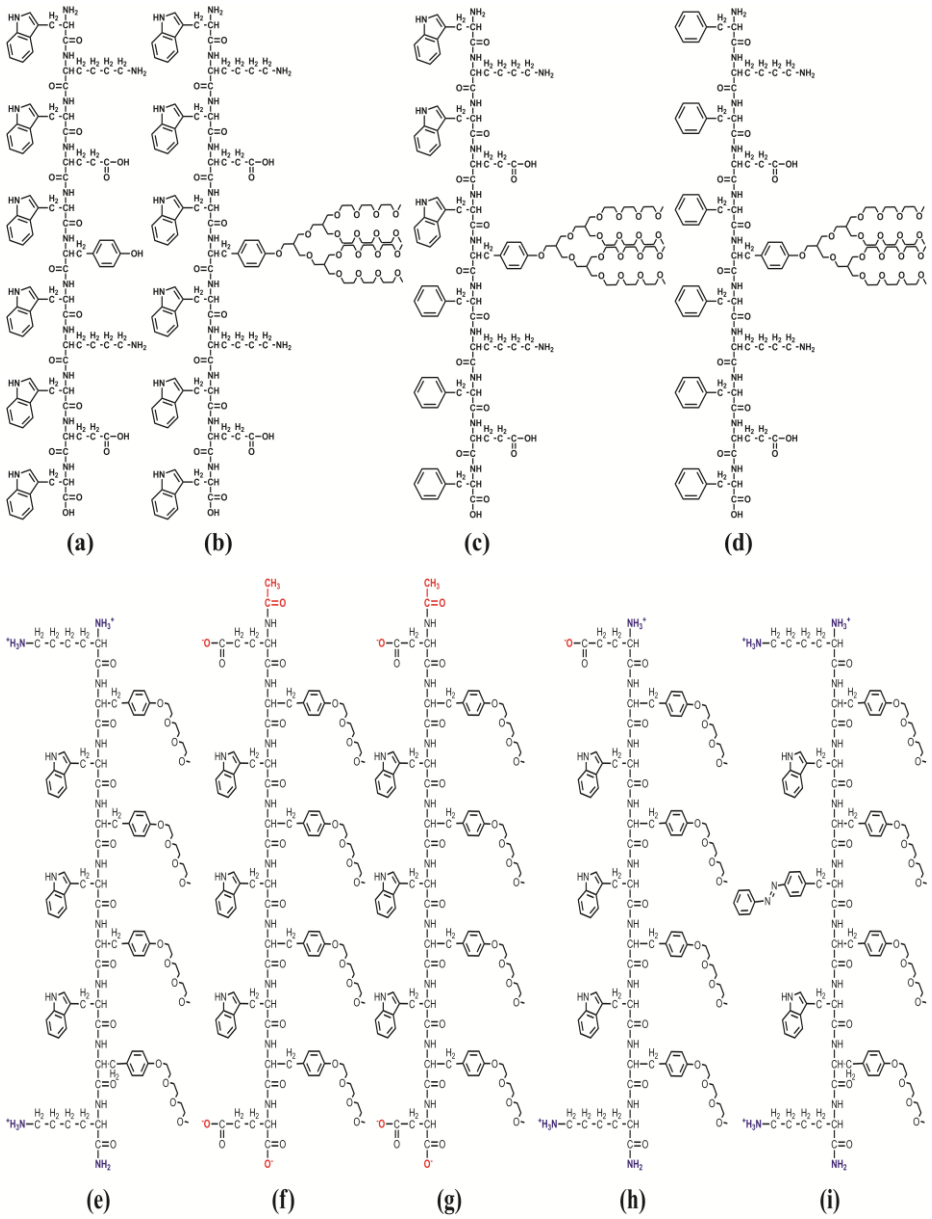


**Fig. II−1.** Primary structures of monomers(*113, 114*): (a) WT of T1, (b) WT of T3, (c) W(1,3,5)F mutant of T3, (d) W−to−F mutant of T3, (e) P1, (f) P1b, (g) P1c, (h) P2, (i) P3. WT of T1 is the 11−mer with the primary structure, WKWEW**Y**WKWEW, and WT of T3 has the oligoether dendron functionalized to the hydroxyl group (−OH) of the tyrosine residue in the middle. The primary structure of P1, P1b, P1c, P2, and P3 are KY*WY*WY*WY*K−NHE, ACE−

EY*WY*WY*WY*E, ACE-DY*WY*WY*WY*D, EY*WY*WY*WY*K-NHE, and KY*WY*F*Y*WY*K-NHE, respectively. Y* and F* are tri(ethylene glycol) monomethoxy ether functionalized tyrosine and phenyldiazene functionalized phenylalanine.

For all simulations and the quantum computations, the Amber10™(*40*) and the Gaussian03™(*52*) package programs were utilized, respectively, unless mentioned. Analyses tools were mainly utilized as supplied from the AMBER™(*40*).

## II-3. Results and Discussions

The convergence of the MD simulation was determined by the time evolution of RMSD and RMSFs with 500 ps time window over all the MD trajectories. Both RMSD and RMSFs went to the constant values as time elapsed, i.e., the RMSD and the RMSFs revealed the upper bounded and the lower bounded, respectively.

The MD simulation time for T1 (Figures II-1-(a)) is long enough because the time evolution of RMSD is convergent and RMSFs of the residues are stable compared with the broken case (Figure II-2-(a), (b) and AP.II-1). T1 got the planar structure consisting of antiparallel $\beta$ sheets. Moreover, monolayered structures could never be sustained but only the bilayered for ~5 ns.

Going in the depth of the structure, indole rings of the trp residues were alternatively arranged with respect to the plane containing all backbones of constituent monomers in a monolayer, and the orientation of indole rings of trp residues was symmetric with respect to the interface between monolayers when only the orientation of indole rings of trp residues was concerned (Figure II-2-(f) and Figure II-3).

In other words, whenever indole rings on one monolayer were arranged in the same direction to the other indole rings on the other monolayer, the structures got broken. Also, whenever all indole rings on the bilayer were located to the interface between

monolayers or to the outside, the structure wasn’ t sustained during the simulation.

RMSFs of trp residues showed the biggest of constituent residues in the T1, and trp residues have the aromatic 9-membered ring, i.e., the indole ring whose electron clouds are rigid. Thus, the stability of structures might result from restraining the outrageous mobility of the trp residues (Figure II-2-(d) and (e)). The alternative arrangement of trp residues and the double layer might make T1 sustained because the repulsion between trp residues could be optimal, i.e., the least. T1 might not have any factors for the interfacial curvature which forced its 1-D structure to be bent.

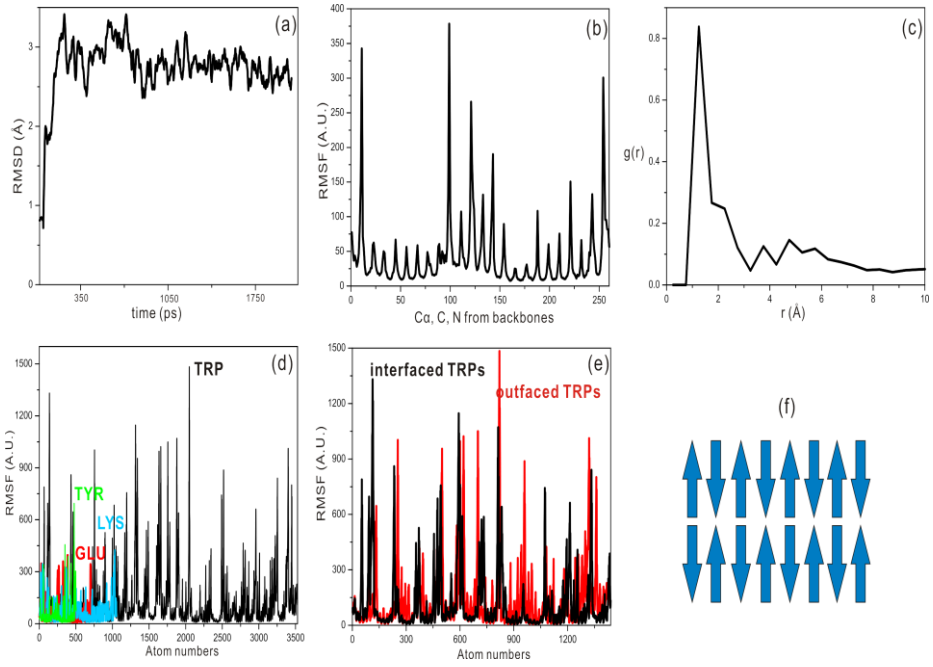


**Fig. II-2.** RMSD, RMSF, and distribution of RDF for T1 at 300 K: (a) time

evolution of RMSD, (b) RMSF for α−carbons, carbonyl carbons, and nitrogens of the amide bonds, (c) RDF, (d) RMSF for tyrosine, glutamic acid, lysine, and tryptophan residues (black for the TRP residues, green for the TYR, red for the GLU, and sky−blue for the LYS), (e) RMSF for interfaced and outfaced tryptophan residues (red is for the outfaced and black for the interfaced), and (f) diagram for the alignment of indole rings from Ws, where tips of arrows display indole rings.

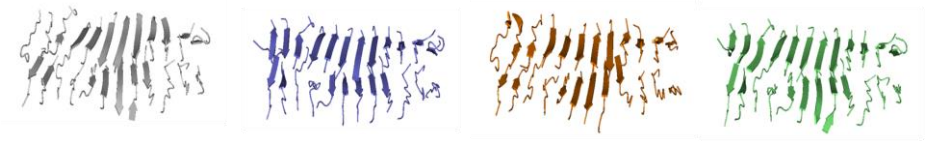


**Fig. II−3.** Representative conformers of 24−mer of T1 from clustering analyses at 300 K based on the k−means algorithm(*54*). Numbers disclose their occurrences. Structures are displayed in the cartoon type.

In the previous work, we proposed a fundamental designing principle for constructing nanoring structures from ß−peptides and hypothesized that the induction of curvature between the adjacent ß strands would force the 1−D structure to be bent. (*113*) Since designed by T−shape ß–peptide building blocks such that bulky hydrophilic dendrons placed at the central part of ß−peptides, T3 should induce the curvature at the interface between ß strands which results from nonbonding pairs of oxygens from the dendrons.

Therefore, WT of T3 (Figure II−1−(b)) is believed that the 40−mer could sustain its structure ever since because the

evolution of RMSD for the 40−mer is convergent and its RMSFs are stable during the production MD compared with the unstable structure (Figure II−4, Figure AP.II−1).

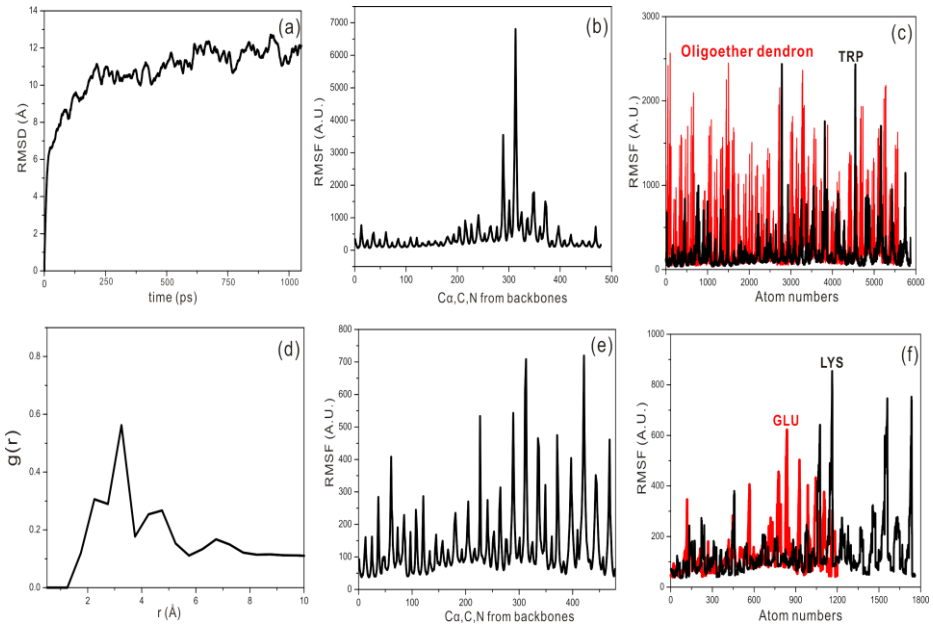


**Fig. II−4.** Analyses for WT of T3 at 300 K: (a) time evolution of RMSD, (b) RMSF of $\alpha$−carbons, carbonyl carbons, and nitrogens of the amide bonds on the backbones of monomers, (c) RMSF of oligoether dendrons and tryptophan residues, (d) RDF over simulation time, (e) RMSF of $\alpha$−carbons, carbonyl carbons, and nitrogens of the amide bonds on the backbones of monomers, and (f) RMSF of lysine and glutamic acid residues for the last 200 ps.

Of constituent residues in WT of T3, oligoether dendrons have the largest RMSFs and trp residues the second (Figure II−4−(c) and (f)). Although distances and alignments between constituent monomers in 12−mer, 24−mer and 50−mer of WT from T3 were adjusted by any means, the structures got only broken just within

100 ps after the equilibration. Only the 40-mer sustained its structure for 1 ns or more.

WT of T3 showed the nanoring shape with the arrangement which indole rings got distributed in the core region and oligoether dendrons outside (Figure II-5 (i)-(l)). It might result from the fact that indole rings of the trp residues takes the hydrophobic characteristics and oxygens of oligoether dendrons make oligoether dendron functionalized tyr residue more hydrophilic. And representative conformers of WT from T3 displayed ~3.5-4.5 nm of pore sizes and ~11 nm of diameters from projected images, which is consistent with the experimental data(*113*).

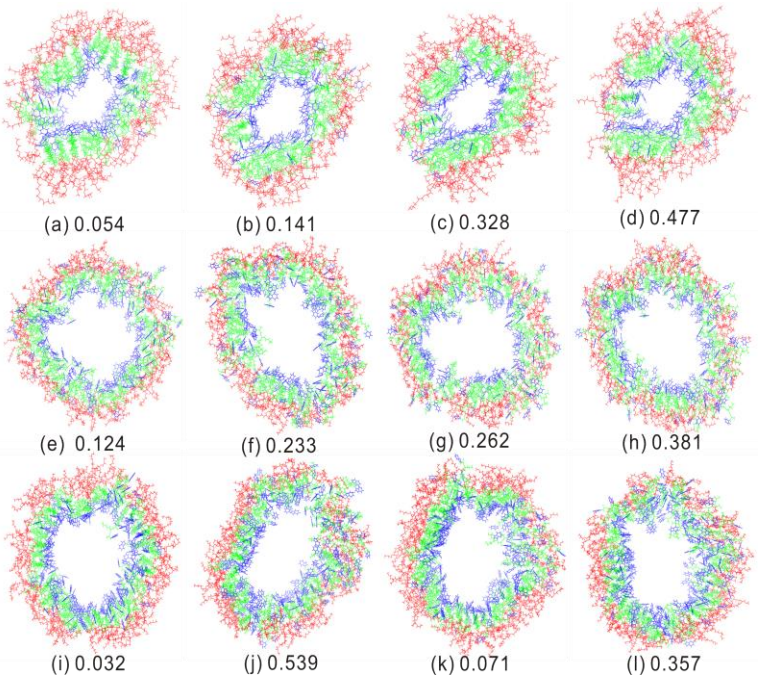

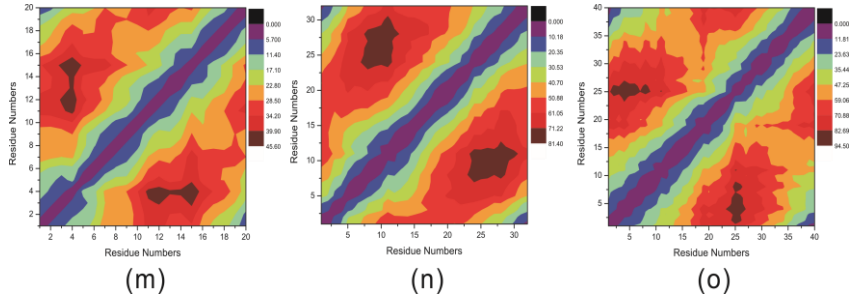


**Fig. II-5.** Representative conformers of WT of T3 and its mutants from clustering analyses at 300 K based on the k-means algorithm(*54*). (a)-(d) for W-to-F mutants, (e)-(h) for serial three W-to-F mutants, (i)-(l) for WT and (m)-(o) distance matrices between Cαs of Tyr for W-to-F mutant, W(1,3,5)F mutant and WT, respectively. W-to-F mutant, W(1,3,5)F mutant and WT have diameters of ca. 4.56, 8.14, and 9.45 nm, respectively. Reds display oligoether dendrons, blues W/F residues, and greens the others. Numbers disclose their occurrences over the MD trajectories.

Oligoether dendrons themselves showed averaged radii of gyration, 7 Å, and distances between terminal carbons, ~1.5 nm, which amounts to twice of radii of gyration at 300 K (Figure AP.II-2). It might result from the fact that oligoether dendrons have 16 oxygens and oxygen has two pairs of nonbonding electrons (Figure II-1). Thus, oligoether dendron itself has the tendency of occupying more space than the other residues of T3 in order to make the nanoring structure stabilized, leading to the main cause of the interfacial curvature. It was verified by the result that the planar WT of T3 got exploded within 100 ps after the equilibration, and the fragmentation started from the terminal regions. Thus, oligoether dendrons might be thought to dominate

the stability and the shape of the bionanostructure.

The nanoring shaped 12-mer and 24-mer of WT from T3 got only broken within 100 ps after the equilibration. Analyses of their trajectories reflect that distances between constituent backbones are unfavorable for the hydrogen bondings. The nanoring-shaped 50-mer has much shorter distances between atomic nuclei of adjacent constituents, thereby leading to the severe nucleic repulsion. But the 40-mer might have constituents suitably separated for both the hydrogen bonding and the nucleic repulsion. In addition, ~3.5-4.5 nm of pore sizes in the 40-mer might make side chains of the confronting monomers optimally separated. Thus, the 40-mer was believed to be one of the optimal numbers of monomers in the formation of the nanoring.

The W-to-F mutation could make the size of nanoring controllable because pi electrons get decreased as indole rings are changed to the benzene, which leads to decreasing the electronic repulsion between adjacent constituents in the core.

The possible cases could be categorized as a minimum, a medium, and a maximum. The minimum could be realized by all W-to-F mutation from WT and the medium by serial three W-to-F mutation. The medium was impossible by other ways, i.e., alternative mutations. Like WT, all W-to-F mutation and serial three W-to-F mutation took the nanoring and the arrangement

which oligoether dendrons were distributed outside the nanoring and the indole rings in the core (Figure II-5-(a) to (h)). Since the patterns for all W-to-F and the serial three W-to-F mutants showed the same patterns as for WT, they would sustain their structures ever since.

The trends for RMSFs of residues in the core, i.e., trp or phe residues might be very important (Figure II-6). The core of WT had RMSFs comparable to its outside but the core of the W-to-F mutants had the decreasing RMSFs as the W-to-F mutation enhanced. This implies that the reduced RMSFs from the W-to-F mutation could make the size of the nanoring controllable because localized oligoethers could induce the interfacial curvature.

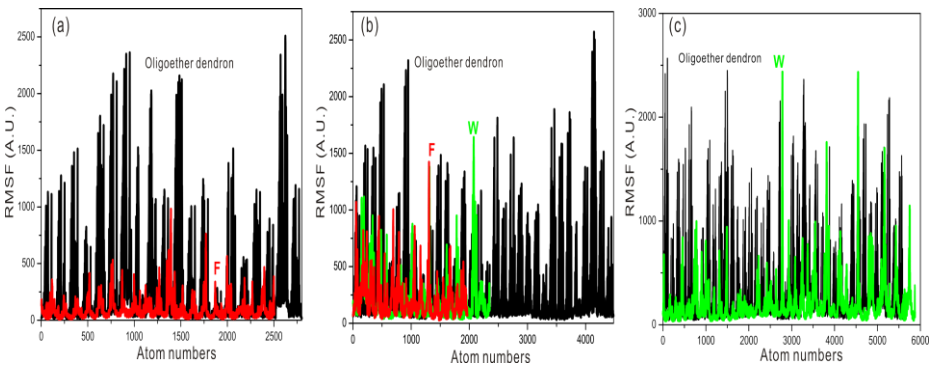


**Fig. II-6.** RMSFs for (a) all W-to-F mutant of T3, (b) W(1,3,5)F mutant of T3, and (c) WT of T3.

Of many trials, 20-mer was the optimal number for the formation of all W-to-F mutants and 32-mer for the W(1,3,5)F

mutants. Averaged Rgs, <Rg> are 20.74556 (0.2739) for all W-to-F mutation, 33.96784 Å (0.78934) for W(1,3,5)F mutation, and 37.00649 (0.37911) for WT, where numbers in parentheses are standard deviations.

The distance between adjacent Cαs of 40-mer consistent with the experimental finding(*113*) could be computed by the second cosine law, 0.222 nm after the distance between the Cα of the constituents and the origin from the structure of the 40-mer was measured, *ca.* 1.9~2 nm over the PyMol(*86*) (Fig. II-7). Based on this, distances between adjacent Cαs for 20-mer of all W-to-F and 32-mer of W(1,3,5)F mutants from T3 could be obtained: 0.71, 1.132 nm.

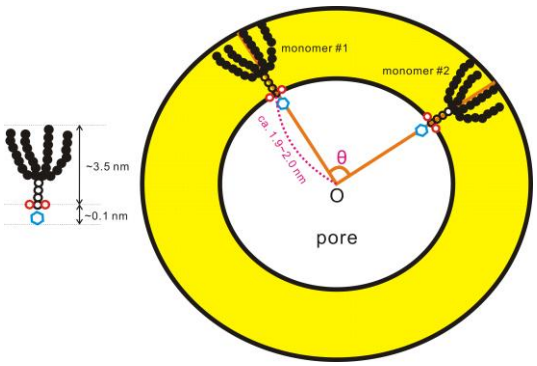


**Fig. II-7.** The simplified diagram for computing the distance between adjacent backbones.

As far as the magnitude of diameters from the nanoring is median of the possible cases from T3, W(1,3,5)F mutant could sustain its structure, but W(1,5,9)F not. WT has two indole-

indole repulsions between adjacent monomers (Fig. II-8-(a)). W(1,3,5)F mutant has one indole-benzene repulsion (Fig. II-8-(c)), but W(1,5,9)F mutant has one indole-benzene and one indole-indole repulsion (Fig. II-8-(b)). Based on RMSFs, the indole-benzene repulsion from W(1,5,9)F should be severe enough to make its nanostructure broken (data not shown), but W(1,3,5)F mutant should be suitable, leading to smaller diameters of the nanoring because indole-benzene repulsion decreases compared with WT.

Since W-to-F mutant would have only benzene-benzene repulsion, it would take smaller diameters from the nanoring than any other types of T3. Therefore, it could make the size of the nanoring controllable through the W-to-F mutation method.

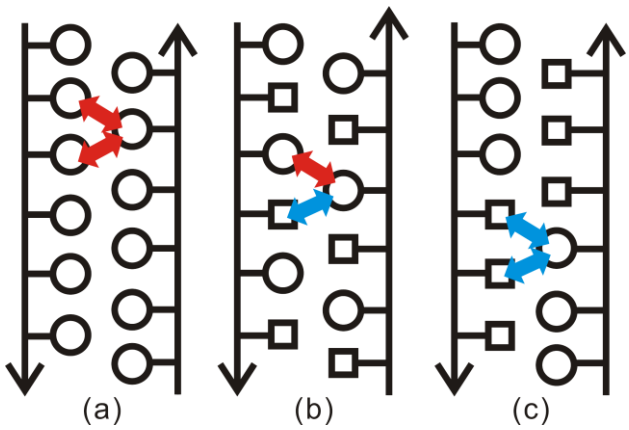


**Fig. II-8**. Arrangement of indole rings of trp residues between adjacent monomers of T3/its mutant: (a) WT, (b) W(1,5,9)F, and (c) W(1,3,5)F. Arrows display the direction from the N-terminal to the C-terminal.

As the other factors for the formation of the nanoring, the Coulombic interaction and the hydrogen bonding might contribute. The parallel alignment of constituent monomers both in T1 and T3 made the formation of the nanoring impossible because the parallel alignment would make the same charged residues drawn closely enough for the nanoring to be broken. Thus, Coulombic attractive interaction might play a role in holding monomers. As shown in Figure II-2-(c) and II-4-(d), the hydrogen bonding might play a role in the maintenance of the structure: RDFs for the mutants of T3 showed the same patterns as T1 (Figure AP.II-3).

Although the indole rings of trp residues looked as closely distributed as possible, T1 and T3 might not display the pi stacking interaction at this level (Figure II-9).

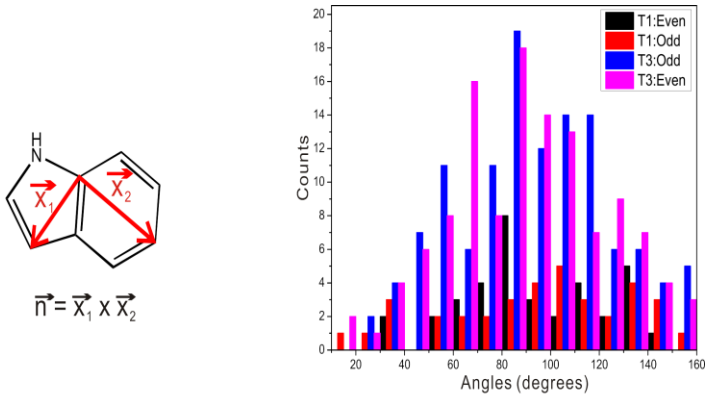


(a) (b)

**Fig. II-9.** Distribution of angles between adjacent indole rings of trp residues: (a) vectors for the computation of angles between the indole rings. (b)

distributions of angles between normal vectors of the adjacent indole rings. For T3, only WT was displayed but the mutants showed the same results. "Even" means the even numbered pairs and "odd" the odd numbered pairs.

Binding energies from monomers acted in line (Table II-1). As far as oligoether dendons are devoid of, alternatively positioned indole rings and the planar structure could result in the most optimal arrangement of indole rings, and lead to make T1 the strongest. However, as numbers of indole rings increased, the strengths for forming the nanoring of T3 got more weakened.

Since T3 and its analog got the factor for the interfacial curvature (*vide supra*), their cores should have the localized indole rings in the core which were aromatic and rigid. Such forced local crowdedness was believed to lead to weakening the forming strength.

| Types | Polymers | Binding energies |
|---|---|---|
| T3 | 20-mer of W-to-F | 747.6165 |
| | 32-mer of W(1,3,5)F | 580.8259 |
| | 40-mer of WT | 260.2651 |
| T1 | 24-mer | 1189.4883 |

**Table II-1.** Binding energies from monomers (kcal/mol)

Based on analyses from WT and mutants of T3, it's approved that the oligoether dendron could act as the factor for the interfacial curvature in the formation of the nanobiostructure.

However, unlikely to the T series, P series have the primary structure whose inner residues are uncharged and terminal ones charged with intention (Fig. II-1-(e)~(i)). Tri(ethylene glycol) monomethoxy ethers could play a role in strengthening the hydrophilicity of tyr residues. Just one tri(ethylene glycol) monomethoxy ether was functionalized to one tyr residue in the P series and such prepared derivatives were distributed over the monomer, thereby leading to only the increased hydrophilicity. The phenyldiazene functionalized phe residue had been introduced in order to strengthen the hydrophobicity over the central trp residue.(*114*)

Based on the time evolution of RMSDs and RMSFs over the MD, P1, P1b, and P1c were sustained and showed the same structure as T3 (Fig. II-10). Their diameters are similar to ones of WT from T3, ~10-11 nm from projected images of the representatives. But, from distance matrices (Fig.II-5 and 10), the diameters of P1, P1b, and P1c are different from those of WT from T3, smaller diameters: 9.45 nm of T3 vs ca 7.9 nm of the P series. It might result from the decrement of trp residues, i.e. the P series have smaller numbers of trp residues compared with WT of T3.

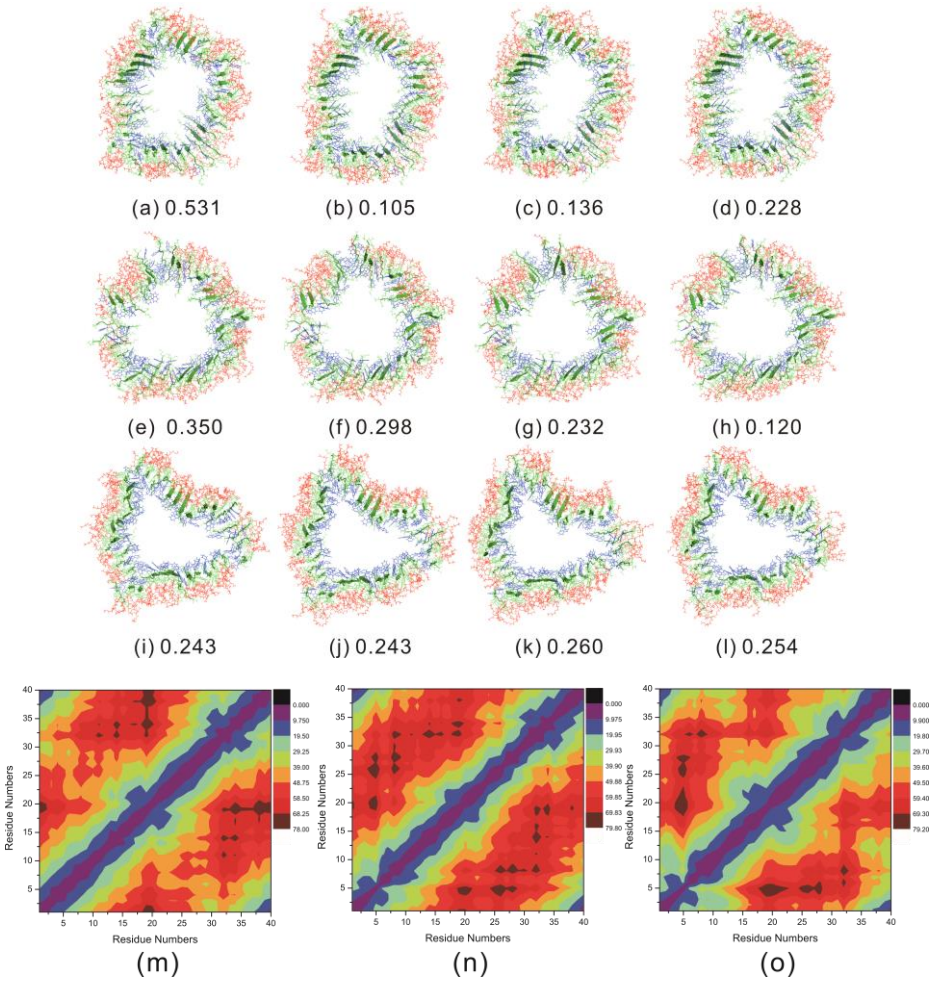


**Fig. II-10.** Representative conformers of P1, P1b, and P1c from clustering analyses at 300 K based on the k-means algorithm(*54*). Reds display tri(ethylene glycol) monomethoxy ethers, blues trp residues, and greens the others. Numbers disclose their occurrences. The 1st, 2nd, and 3rd rows are for P1, P1b, and P1c, respectively. (m)-(o) are distance matrices between Cαs of the 2nd trp residues for P1, P1b, and P1c, respectively, and their diameters are ca. 7.8, 7.98, and 7.92 nm, respectively.

Introducing all W-to-F point mutation could make diameters of the nanoring diminished only for P1. It would have 20

monomers and ca. 4.54 nm of diameters (Fig.II-11). Since the W-to-F mutation wouldn't only induce the diminished indole-indole repulsion but also the decreased distance between charged residues, it could result in the severe influence on their structural stability. Shorter carbon bridges between the backbones and the charged atoms of the side chains from P1b and P1c are believed to force the structural stability ill-conditioned because charged side chains should get closer enough to make the severe influence on both the stability and the shape (Fig.II-11).

Diameters of T3 could be decreased up to an half WT through all W-to-F mutation, but P1 couldn't. It might result from that the Coulombic repulsion between charged residues couldn't make the decrement of the diameter restricted.

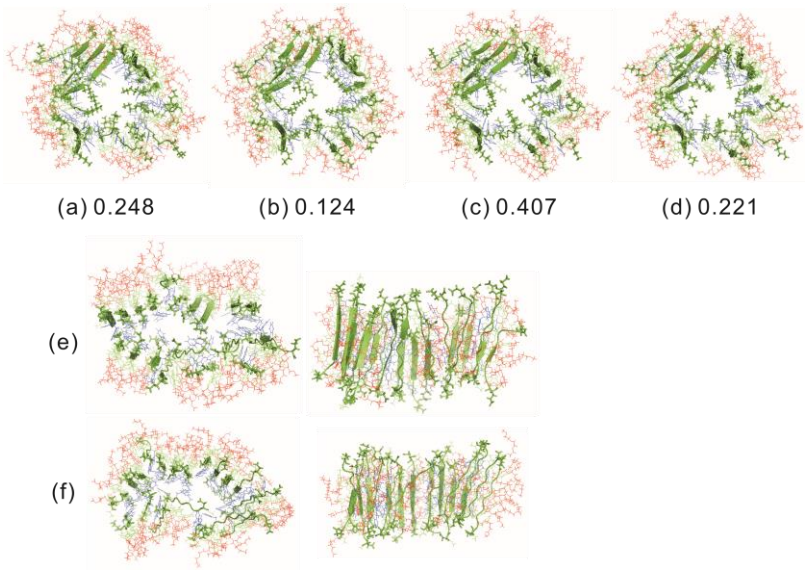

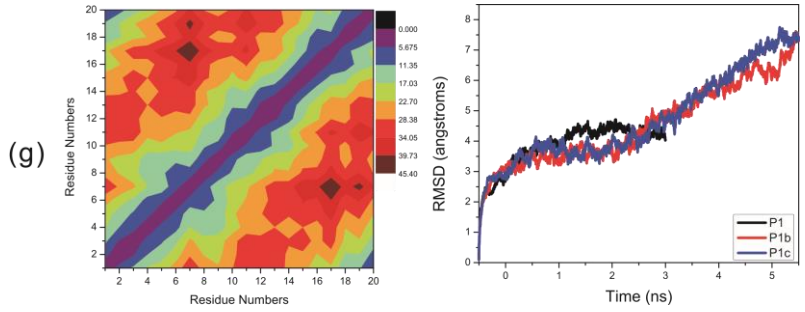


**Fig.II-11.** Representative conformers of W(1,3,5)F mutants of P1, P1b, and P1c from clustering analyses at 300 K based on the k-means algorithm(*54*). Reds display tri(ethylene glycol) monomethoxy ethers, blues trp residues, and greens the others. Numbers disclose their occurrences. (a)-(d) for P1, (e) for P1b, (f) for P1c, and (g) distance matrix between Cαs of the 2$^{nd}$ trp residues for P1 and time evolution of RMSD. Diameters of W(1,3,5)F mutant of P1 are ca. 4.54 nm which is comparable to W-to-F mutant of T3.

The solvation shell within 0.34 nm showed that charged residues would get the most solvated except for P1c (Fig.II-12). Insufficiently solvated charged residues of P1c seemed to result in the irregular shape of the nanoring. In addition, the stability of the solvation in P1b could be suggested to result in the nicest shape of the nanoring.

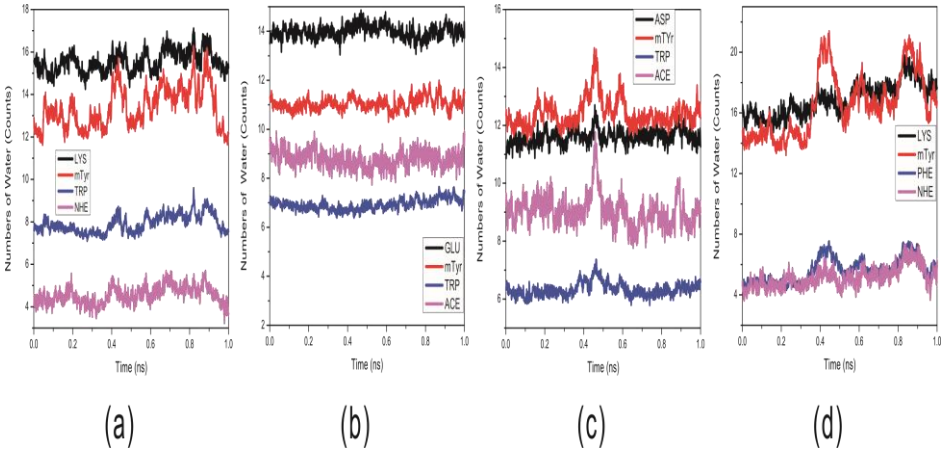


**Fig.II-12.** The solvation shell within 0.34 nm. (a)-(d) are for WT of P1, P1b, P1c and W(1,3,5)F of P1, respectively.

By the argument led from Fig. II-7 and II-8, justifying the formation for WT of P1, P1b, P1c, and W(1,3,5)F mutant of P1 could be obtained, but the major factor for the interfacial curvature seemed to be different from T3. As said in the reference(*114*), it could be the Coulombic repulsion because P1 has much more diminished ether derived tyr residue and its influence to its surrounding couldn't be as severe as T3.

Since P2 wasn't sustained in both the experiment and the simulation, absolute total charges should be 3 at least. Likely enough, P1b and P1c could be sustained (Fig. II-10-(e)~(h)) though the K-to-E and the E-to-D mutations would force the minimum distance between charged residues shorter.

P3 has the functionalized phe residue with the strengthened hydrophobicity in the middle.(*114*) Since phenyldiazene ($C_6H_5$-

$N_2H$) has 8 pi electron, it's antiaromatic by the Hueckel rule. When phenyldiazene is bonded to the benzene, its total pi electron is 14 and thereby phenyldiazene functionalized phe residue gets aromatic (Fig. II-13). Therefore, the side chain of phenyldiazene functionalized phe residue of P3 gets rigid and P3 has the more crowded core than P1.

To make matters worse, WT of T3 has trp residues with the fused heterocyclic side chain, indole rings (the longest length is ca. 0.46 nm), but P3 has nonfused side chain (the longest length is ca. 0.9 nm) which could exasperate the interior crowdedness although the reference just pointed out the increment of the hydrophobicity(*114*). That's believed to be a major obstacle to the formation of the nanoring.

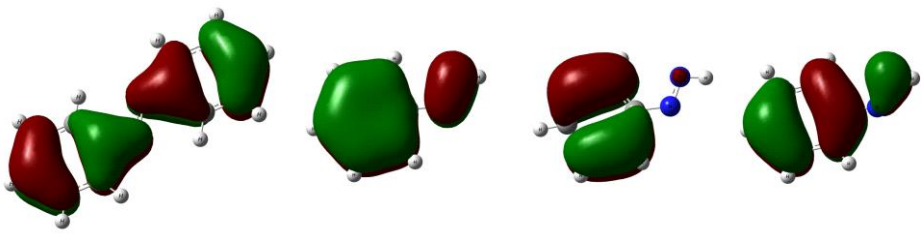


**Fig. II-13.** Molecular orbital computed by B3LYP/6-31G(d)(*49, 50*): (a) MO44 of azodibenzene ($(C_6H_5)_2N_2$), (b) MO24 of phenyldiazene ($C_6H_5-N_2H$), (c) MO26 of phenyldiazene, and (d) MO27 of phenyldiazene. The orbital of azo ($N_2$) is resonant to benzene rings in azodibenzene, but not in phenyldiazene.

Although this work was not finished and its future couldn't be expected with easy, possible minimum cases for P1b and P1c

could be suggested (Fig.II-14).

Lastly, the P series couldn't sustain their structures under the implicit solvation on no condition, which might result from the non-neutrality of the system. Thus, the solvation effect should be believed to be non-negligible in the P series because of their charged residues.

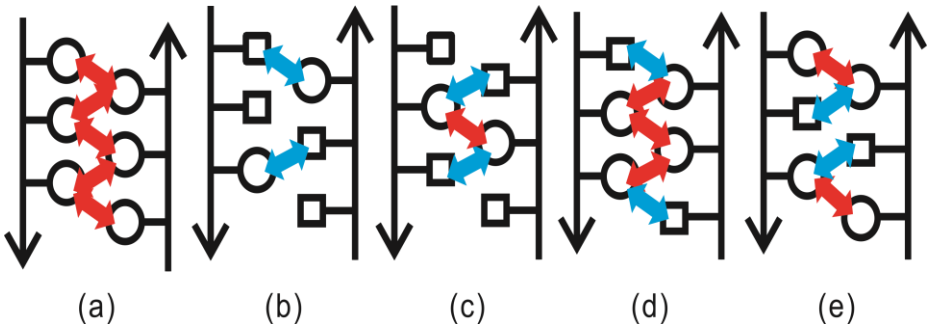


**Fig.II-14.** Possible minimum cases of P1b and P1c: (a) WT, (b)-(c) two point mutations, and (d)-(e) one point mutation. Circles and squares are indole rings and benzene rings, respectively.

## II-4. Conclusions

We classically simulated WT and several variants generated from monomer of 11-mer and capped 10-mer at the physiological condition in order to delineate the structural factors on the formation of artificial peptides mimicking the $\beta$-barrel membrane proteins.

Coulombic interaction, hydrogen bonding, hydrophobic interaction, and electronic repulsion, i.e., optimal distribution of rigid electron clouds, play the important role in the formation of the peptides mimicking the $\beta$-barrel. Of these interactions, the electronic repulsion between aromatic rings in the core dictates the structure. The careful adjustment of this electronic repulsion, i.e. through the point mutation, could make it possible to control the size of the nanobiostructure.

In addition, the electronic or the Coulombic repulsion could act as the factor for the interfacial curvature between constituent monomers, and the Coulombic should make the magnitude of the management restricted.

For the technical aspect, as far as the major factor is irrelevant to charges, just the implicit solvation could describe the experimental finding, but only explicit solvation could describe the experimental finding when the major factor is relevant to charges.

# Bibliography


1. C. Levinthal, "Are there pathways for protein folding?". *Journal de Chimie Physique et de Physico-Chimie Biologique* **65**, 44-45 (1968).
2. P. G. Wolynes, J. N. Onuchic, D. Thirumalai, Response. *Science* **268**, 960-961 (1995).
3. B. A. Berg, T. Neuhaus, Multicanonical ensemble: A new approach to simulate first-order phase transitions. *Phys. Rev. Lett.* **68**, 9-12 (1992).
4. A. P. Lyubartsev, A. A. Martsinovski, S. V. Shevkunov, P. N. Vorontsov-Velyaminov, New approach to Monte Carlo calculation of the free energy: Method of expanded ensembles. *J. Chem. Phys.* **96**, 1776-1783 (1992).
5. R. H. Swendsen, J.-S. Wang, Replica Monte Carlo Simulation of Spin-Glasses. *Phys. Rev. Lett.* **57**, 2607-2609 (1986).
6. M. G. Spillantini, R. A. Crowther, R. Jakes, M. Hasegawa, M. Goedert, α-Synuclein in filamentous inclusions of Lewy bodies from Parkinson's disease and dementia with Lewy bodies. *Proc. Natl. Acad. Sci. U.S.A.* **95**, 6469-6473 (1998).
7. A. Surguchov, in *Int. Rev. Cell. Mol. Biol.*, W. J. Kwang, Ed. (Academic Press, 2008), vol. **270**, pp. 225-317.
8. E. Ohama, F. Ikuta, Parkinson's disease: Distribution of Lewy bodies and monoamine neuron system. *Acta Neuropathol.* **34**, 311-319 (1976).

9. M. G. Spillantini et al., α-Synuclein in Lewy bodies. *Nature* **388**, 839-840 (1997).

10. K. A. Conway, J. D. Harper, P. T. Lansbury, Accelerated in vitro fibril formation by a mutant α-synuclein linked to early-onset Parkinson disease. *Nat. Med.* **4**, 1318-1320 (1998).

11. J. Li, V. N. Uversky, A. L. Fink, Effect of Familial Parkinson's Disease Point Mutations A30P and A53T on the Structural Properties, Aggregation, and Fibrillation of Human α-Synuclein†. *Biochemistry* **40**, 11604-11613 (2001).

12. P. J. McLean, H. Kawamata, S. Ribich, B. T. Hyman, Membrane Association and Protein Conformation of α-Synuclein in Intact Neurons. *J. Biol. Chem.* **275**, 8812-8816 (2000).

13. W. S. Davidson, A. Jonas, D. F. Clayton, J. M. George, Stabilization of α-Synuclein Secondary Structure upon Binding to Synthetic Membranes. *J. Biol. Chem.* **273**, 9443-9449 (1998).

14. W. Hoyer, D. Cherny, V. Subramaniam, T. M. Jovin, Impact of the Acidic C-Terminal Region Comprising Amino Acids 109-140 on α-Synuclein Aggregation in Vitro†. *Biochemistry* **43**, 16233-16242 (2004).

15. M. S. Nielsen, H. Vorum, E. Lindersson, P. H. Jensen, Ca2+ Binding to α-Synuclein Regulates Ligand Binding and

Oligomerization. *J. Biol. Chem.* **276**, 22680-22684 (2001).

16. D. F. Clayton, J. M. George, Synucleins in synaptic plasticity and neurodegenerative disorders. *J. Neurosci. Res.* **58**, 120-129 (1999).

17. V. N. Uversky, J. Li, A. L. Fink, Evidence for a Partially Folded Intermediate in α-Synuclein Fibril Formation. *J. Biol. Chem.* **276**, 10737-10744 (2001).

18. S. J. Wood et al., α-Synuclein Fibrillogenesis Is Nucleation-dependent. *J. Biol. Chem.* **274**, 19509-19512 (1999).

19. X.-J. Lin et al., Secondary structural formation of α-synuclein amyloids as revealed by g-factor of solid-state circular dichroism. *Biopolymers* **83**, 226-232 (2006).

20. M. Gerard et al., The aggregation of alpha-synuclein is stimulated by FK506 binding proteins as shown by fluorescence correlation spectroscopy. *FASEB J.* **20**, 524-544 (2006).

21. M. Gerard et al., FK506 binding protein 12 differentially accelerates fibril formation of wild type alpha-synuclein and its clinical mutants A30P or A53T. *J. Neurochem.* **106**, 121-133 (2008).

22. M. Gerard et al., Inhibition of FK506 Binding Proteins Reduces α-Synuclein Aggregation and Parkinson's Disease-Like Pathology. *J. Neurosci.* **30**, 2454-2463 (2010).

23. S. F. Göthel, M. A. Marahiel, Peptidyl-prolyl cis-trans isomerases, a superfamily of ubiquitous folding catalysts. *Cell. Mol. Life Sci.* **55**, 423-436 (1999).

24. M. Avramut, C. L. Achim, Immunophilins and their ligands: insights into survival and growth of human neurons. *Physiol. Behav.* **77**, 463-468 (2002).

25. S. Brecht et al., Changes in peptidyl-prolyl cis/trans isomerase activity and fk506 binding protein expression following neuroprotection by fk506 in the ischemic rat brain. *Neuroscience* **120**, 1037-1048 (2003).

26. M. W. Harding, A. Galat, D. E. Uehling, S. L. Schreiber, A receptor for the immuno-suppressant FK506 is a cis-trans peptidyl-prolyl isomerase. *Nature* **341**, 758-760 (1989).

27. G. Fischer, B. Wittmann-Liebold, K. Lang, T. Kiefhaber, F. X. Schmid, Cyclophilin and peptidyl-prolyl cis-trans isomerase are probably identical proteins. *Nature* **337**, 476-478 (1989).

28. N. Takahashi, T. Hayano, M. Suzuki, Peptidyl-prolyl cis-trans isomerase is the cyclosporin A-binding protein cyclophilin. *Nature* **337**, 473-475 (1989).

29. J. J. Siekierka, S. H. Y. Hung, M. Poe, C. S. Lin, N. H. Sigal, A cytosolic binding protein for the immunosuppressant FK506 has peptidyl-prolyl isomerase activity but is distinct from cyclophilin. *Nature* **341**, 755-757 (1989).

30. J. M. Souza, B. I. Giasson, V. M. Y. Lee, H. Ischiropoulos, Chaperone-like activity of synucleins. *FEBS Lett.* **474**, 116-119 (2000).

31. R. A. Crowther, R. Jakes, M. G. Spillantini, M. Goedert, Synthetic filaments assembled from C-terminally truncated α-synuclein. *FEBS Lett.* **436**, 309-312 (1998).

32. K. P. Lu, G. Finn, T. H. Lee, L. K. Nicholson, Prolyl cis-trans isomerization as a molecular timer. *Nat. Chem. Biol.* **3**, 619-629 (2007).

33. W. J. Wedemeyer, E. Welker, H. A. Scheraga, Proline Cis-Trans Isomerization and Protein Folding†. *Biochemistry* **41**, 14637-14644 (2002).

34. J. Meuvis, M. Gerard, L. Desender, V. Baekelandt, Y. Engelborghs, The Conformation and the Aggregation Kinetics of α-Synuclein Depend on the Proline Residues in Its C-Terminal Region. *Biochemistry* **49**, 9345-9352 (2010).

35. W. C. Still, A. Tempczyk, R. C. Hawley, T. Hendrickson, Semianalytical treatment of solvation for molecular mechanics and dynamics. *J. Am. Chem. Soc.* **112**, 6127-6129 (1990).

36. A. Onufriev, D. Bashford, D. A. Case, Modification of the Generalized Born Model Suitable for Macromolecules. *J. Phys. Chem. B* **104**, 3712-3720 (2000).

37. A. Onufriev, D. Bashford, D. A. Case, Exploring protein native states and large-scale conformational changes with a

modified generalized born model. *Proteins* **55**, 383-394 (2004).

38. Z. Z. Fan, J. K. Hwang, A. Warshel, Using simplified protein representation as a reference potential for all-atom calculations of folding free energy. *Theor. Chem. Acc.* **103**, 77-80 (1999).

39. P. A. D. Kollman, R.; Cornell, W.; Fox, T.; Chipot, C.; Pohorille, A., in *Computer Simulation of Biomolecular Systems*, A. W. Wilkinson, P.; van Gunsteren,W.F., Ed. (Elsevier, 1997), vol. **3**, pp. 83–96.

40. T. A. D. D.A. Case, T.E. Cheatham, III, C.L. Simmerling, J. Wang, R.E. Duke, R. Luo,, R. C. W. M. Crowley, W. Zhang, K.M. Merz, B.Wang, S. Hayik, A. Roitberg, G. Seabra, I., K. F. W. Kolossváry, F. Paesani, J. Vanicek, X.Wu, S.R. Brozell, T. Steinbrecher, H. Gohlke,, C. T. L. Yang, J. Mongan, V. Hornak, G. Cui, D.H. Mathews, M.G. Seetin, C. Sagui, V. Babin,, a. P. A. Kollman. (University of California, San Francisco., 2008).

41. A. R. Leach, in *Molecular modeling: principles and applications.* (Prentice Hall, 2001), chap. **5**, pp. 262-267.

42. H. J. C. Berendsen, J. P. M. Postma, W. F. van Gunsteren, A. DiNola, J. R. Haak, Molecular dynamics with coupling to an external bath. *J. Chem. Phys.* **81**, 3684-3690 (1984).

43. A. Mitsutake, Y. Sugita, Y. Okamoto, Generalized-ensemble algorithms for molecular simulations of biopolymers.

*Biopolymers (Pept. Sci.)* **60**, 96–123 (2001).

44. H. Nymeyer, S. Gnanakaran, A. E. García, Atomic Simulations of Protein Folding, Using the Replica Exchange Algorithm. *Meth. Enzymol.* **383**, 119–149 (2004).

45. X. Cheng, G. Cui, V. Hornak, C. Simmerling, Modified Replica Exchange Simulation Methods for Local Structure Refinement. *J. Phys. Chem. B* **109**, 8220–8230 (2005).

46. J.–P. Ryckaert, G. Ciccotti, H. J. C. Berendsen, Numerical integration of the cartesian equations of motion of a system with constraints: molecular dynamics of n–alkanes. *J. Comput. Phys.* **23**, 327–341 (1977).

47. G. S. Grest, K. Kremer, Molecular dynamics simulation for polymers in the presence of a heat bath. *Phys. Rev. A* **33**, 3628–3631 (1986).

48. J. Mongan, D. A. Case, J. A. McCammon, Constant pH molecular dynamics in generalized Born implicit solvent. *J. Comput. Chem.* **25**, 2038–2048 (2004).

49. A. D. Becke, Density–functional thermochemistry. III. The role of exact exchange. *J. Chem. Phys.* **98**, 5648–5652 (1993).

50. C. Lee, W. Yang, R. G. Parr, Development of the Colle–Salvetti correlation–energy formula into a functional of the electron density. *Phys. Rev. B* **37**, 785–789 (1988).

51. K. Fukui, The path of chemical reactions – the IRC

approach. *Acc. Chem. Res.* **14**, 363-368 (1981).

52. G. W. T. M. J. Frisch, H. B. Schlegel, G. E. Scuseria, M. A. Rob, J. R. Cheeseman, J. A. Montgomery Jr., T. Vreven, K. N. Kudin, J. C. Burant, J. M. Millam, S. S. Iyengar, J. Tomasi, V. Barone, B. Mennucci, M. Cossi, G. Scalmani, N. Rega, G. A. Petersson, H. Nakatsuji, M. Hada, M. Ehara, K. Toyota, R. Fukuda, J. Hasegawa, M. Ishida, T. Nakajima, Y. Honda, O. Kitao, H. Nakai, M. Klene, X. Li, J. E. Knox, H. P. Hratchian, J. B. Cross, V. Bakken, C. Adamo, J. Jaramillo, R. Gomperts, R. E. Stratmann, O. Yazyev, A. J. Austin, R. Cammi, C. Pomelli, J. W. Ochterski, P. Y. Ayala, K. Morokuma, G. A. Voth, P. Salvador, J. J. Dannenberg, V. G. Zakrzewski, S. Dapprich, A. D. Daniels, M. C. Strain, O. Farkas, D. K. Malick, A. D. Rabuck, K. Raghavachari, J. B. Foresman, J. V. Ortiz, Q. Cui, A. G. Baboul, S. Clifford, J. Cioslowski, B. B. Stefanov, G. Liu, A. Liashenko, P. Piskorz, I. Komaromi, R. L. Martin, D. J. Fox, T. Keith, M. A. Al-Laham, C. Y. Peng, A. Nanayakkara, M. Challacombe, P. M. W. Gill, B. Johnson, W. Chen, M. W. Wong, C. Gonzalez, and J. A. Pople. (Gaussian, Inc., Wallingford, CT, 2003).

53. O. S. Buzko. (San Diego Supercomputer Center, 2009).

54. J. Shao, S. W. Tanner, N. Thompson, T. E. Cheatham, Clustering Molecular Dynamics Trajectories: 1. Characterizing the Performance of Different Clustering Algorithms. *J. Chem.*

*Theory Comput.* **3**, 2312-2334 (2007).

55. J. Hardy, D. J. Selkoe, The Amyloid Hypothesis of Alzheimer's Disease: Progress and Problems on the Road to Therapeutics. *Science* **297**, 353-356 (2002).

56. S. Dennis J, Presenilins, β-amyloid precursor protein and the molecular basis of Alzheimer's disease. *Clin. Neurosci. Res.* **1**, 91-103 (2001).

57. T. Hartmann et al., Distinct sites of intracellular production for Alzheimer's disease Aβ40/42 amyloid peptides. *Nat. Med.* **3**, 1016-1020 (1997).

58. R. E. Tanzi, L. Bertram, Twenty Years of the Alzheimer's Disease Amyloid Hypothesis: A Genetic Perspective. *Cell* **120**, 545-555 (2005).

59. J. M. Nussbaum, M. E. Seward, G. S. Bloom, Alzheimer disease. *Prion* **7**, 14-19 (2012).

60. W. Pulawski, U. Ghoshdastider, V. Andrisano, S. Filipek, Ubiquitous Amyloids. *Appl. Biochem. Biotechnol.* **166**, 1626-1643 (2012).

61. K. Kosaka, S. Oyanagi, M. Matsushita, A. Hori, S. Iwase, Presenile dementia with Alzheimer-, Pick- and Lewy-body changes. *Acta Neuropathol.* **36**, 221-233 (1976).

62. Valerie Askanas, M. W. King Engel, Inclusion-body myositis A myodegenerative conformational disorder associated with Aβ, protein misfolding, and proteasome

inhibition. *Neurol Clin Neurophysiol* **66**, S39-S48 (2006).

63. Y. Luo et al., BACE1 (β-secretase) knockout mice do not acquire compensatory gene expression changes or develop neural lesions over time. *Neurobiol. Dis.* **14**, 81-88 (2003).

64. S. Sadigh-Eteghad et al., Beta-amyloid exhibits antagonistic effects on alpha 7 nicotinic acetylcholine receptors in orchestrated manner. *Journal of Medical Hypotheses and Ideas* **8**, 49-52 (2014).

65. Y. I. Yin et al., γ-Secretase Substrate Concentration Modulates the Aβ42/Aβ40 Ratio: IMPLICATIONS FOR ALZHEIMER DISEASE. *J. Biol. Chem.* **282**, 23639-23644 (2007).

66. N. N. Nalivaeva, N. D. Belyaev, I. A. Zhuravin, A. J. Turner, The Alzheimer's Amyloid-Degrading Peptidase, Neprilysin: Can We Control It? *International Journal of Alzheimer's Disease* **2012**, 12 (2012).

67. G. Bitan, S. S. Vollers, D. B. Teplow, Elucidation of Primary Structure Elements Controlling Early Amyloid β-Protein Oligomerization. *J. Biol. Chem.* **278**, 34882-34889 (2003).

68. S. L. Bernstein et al., Amyloid β-Protein: Monomer Structure and Early Aggregation States of A$\beta$42 and Its Pro19 Alloform. *J. Am. Chem. Soc.* **127**, 2075-2084 (2005).

69. W. L. Klein, G. A. Krafft, C. E. Finch, Targeting small Aβ

oligomers: the solution to an Alzheimer's disease conundrum? *Trends Neurosci.* **24**, 219–224 (2001).

70. D. M. Walsh et al., Naturally secreted oligomers of amyloid β protein potently inhibit hippocampal long–term potentiation in vivo. *Nature* ***416***, 535–539 (2002).

71. R. Kayed et al., Common Structure of Soluble Amyloid Oligomers Implies Common Mechanism of Pathogenesis. *Science* **300**, 486–489 (2003).

72. P. N. Lacor et al., Aβ Oligomer–Induced Aberrations in Synapse Composition, Shape, and Density Provide a Molecular Basis for Loss of Connectivity in Alzheimer's Disease. *J. Neurosci.* **27**, 796–807 (2007).

73. J. Lauren, D. A. Gimbel, H. B. Nygaard, J. W. Gilbert, S. M. Strittmatter, Cellular prion protein mediates impairment of synaptic plasticity by amyloid–β oligomers. *Nature* **457**, 1128–1132 (2009).

74. J. D. Harper, P. T. Lansbury, MODELS OF AMYLOID SEEDING IN ALZHEIMER'S DISEASE AND SCRAPIE:Mechanistic Truths and Physiological Consequences of the Time–Dependent Solubility of Amyloid Proteins. *Annu. Rev. Biochem.* **66**, 385–407 (1997).

75. O. N. Antzutkin, R. D. Leapman, J. J. Balbach, R. Tycko, Supramolecular Structural Constraints on Alzheimer's β–Amyloid Fibrils from Electron Microscopy and Solid–State

Nuclear Magnetic Resonance†. *Biochemistry* **41**, 15436–15450 (2002).

76. J. J. Balbach et al., Supramolecular Structure in Full–Length Alzheimer's β–Amyloid Fibrils: Evidence for a Parallel β–Sheet Organization from Solid–State Nuclear Magnetic Resonance. *Biophys. J.* **83**, 1205–1216.

77. L. Esposito, C. Pedone, L. Vitagliano, Molecular dynamics analyses of cross–β–spine steric zipper models: β–Sheet twisting and aggregation. *Proc. Natl. Acad. Sci. U.S.A.* **103**, 11533–11538 (2006).

78. M. R. Sawaya et al., Atomic structures of amyloid cross–β spines reveal varied steric zippers. *Nature* **447**, 453–457 (2007).

79. S. A. Sievers et al., Structure–based design of non–natural amino–acid inhibitors of amyloid fibril formation. *Nature* **475**, 96–100 (2011).

80. L. K. Thompson, Unraveling the secrets of Alzheimer's β–amyloid fibrils. *Proc. Natl. Acad. Sci. U.S.A.* **100**, 383–385 (2003).

81. B. Ma, R. Nussinov, Stabilities and conformations of Alzheimer's β–amyloid peptide oligomers (Aβ16–22, Aβ16–35, and Aβ10–35): Sequence effects. *Proc. Natl. Acad. Sci. U.S.A.* **99**, 14126–14131 (2002).

82. A. T. Petkova et al., A structural model for Alzheimer's

β-amyloid fibrils based on experimental constraints from solid state NMR. *Proc. Natl. Acad. Sci. U.S.A.* **99**, 16742-16747 (2002).

83. T. R. Serio et al., Nucleated Conformational Conversion and the Replication of Conformational Information by a Prion Determinant. *Science* **289**, 1317-1321 (2000).

84. I. Bertini, L. Gonnelli, C. Luchinat, J. Mao, A. Nesi, A New Structural Model of Aβ40 Fibrils. *J. Am. Chem. Soc.* **133**, 16013-16022 (2011).

85. C. K. Fisher, C. M. Stultz, Constructing ensembles for intrinsically disordered proteins. *Curr. Opin. Struct. Biol.* **21**, 426-431 (2011).

86. Schrodinger, LLC. (2010).

87. D. C. Liu, J. Nocedal, On the limited memory BFGS method for large scale optimization. *Math. Program.* **45**, 503-528 (1989).

88. H. Jónsson, G. Mills, K. Jacobsen, in *Classical and Quantum Dynamics in Condensed Phase Simulations*, B. Berne, G. Ciccoti, D. Coker, Eds. (World Scientific, Singapore, 1998), chap. **16**, pp. 385-404.

89. J.-W. Chu, B. L. Trout, B. R. Brooks, A super-linear minimization scheme for the nudged elastic band method. *J. Chem. Phys.* **119**, 12708-12717 (2003).

90. J. Nasica-Labouze et al., Amyloid β Protein and

Alzheimer's Disease: When Computer Simulations Complement Experimental Studies. *Chem. Rev.* **115**, 3518-3563 (2015).

91. in *Protein Folding, Misfolding and Aggregation Classical Themes and Novel Approaches*, V. Muňoz, Ed. (Royal Society of Chemistry, 2008), chap. **10**, pp. 220-221.

92. S. Jang, S. Shin, Amyloid β-Peptide Oligomerization in Silico: Dimer and Trimer. *J. Phys. Chem. B* **110**, 1955-1958 (2006).

93. S. Jang, S. Shin, Computational Study on the Structural Diversity of Amyloid Beta Peptide (Aβ10-35) Oligomers. *J. Phys. Chem. B* **112**, 3479-3484 (2008).

94. R. K. Wierenga, The TIM-barrel fold: a versatile framework for efficient enzymes. *FEBS Lett.* **492**, 193-198 (2001).

95. F. G. Prendergast, K. G. Mann, Chemical and physical properties of aequorin and the green fluorescent protein isolated from Aequorea forskalea. *Biochemistry* **17**, 3448-3453 (1978).

96. R. Y. Tsien, THE GREEN FLUORESCENT PROTEIN. *Annu. Rev. Biochem.* **67**, 509-544 (1998).

97. W. C. Wimley, The versatile β-barrel membrane protein. *Curr. Opin. Struct. Biol.* **13**, 404-411 (2003).

98. N. Sakai, J. Mareda, S. Matile, Rigid-Rod Molecules in

Biomembrane Models: From Hydrogen-Bonded Chains to Synthetic Multifunctional Pores. *Acc. Chem. Res.* **38**, 79-87 (2005).

99. M. S. Kaucher et al., Selective Transport of Water Mediated by Porous Dendritic Dipeptides. *J. Am. Chem. Soc.* **129**, 11698-11699 (2007).

100. V. Percec et al., Self-assembly of amphiphilic dendritic dipeptides into helical pores. *Nature* **430**, 764-768 (2004).

101. W.-Y. Yang, J.-H. Ahn, Y.-S. Yoo, N.-K. Oh, M. Lee, Supramolecular barrels from amphiphilic rigid-flexible macrocycles. *Nat Mater* **4**, 399-402 (2005).

102. R. G. Parr, W. Yang, *Density-Functional Theory of Atoms and Molecules.* (Oxford University Press: Oxford, 1989).

103. C. Møller, M. S. Plesset, Note on an Approximation Treatment for Many-Electron Systems. *Phys. Rev.* **46**, 618-622 (1934).

104. W. Koch, M. C. A. Holthausen, *Chemist's Guide to Density Functional Theory.* (Wiley-VCH: Weinheim, 2000), vol. **2nd**.

105. C. J. Cramer, *Essentials of Computational Chemistry.* (Wiley: New York, 2002).

106. A. Szabo, N. S. Ostlund, *Modern Quantum Chemistry.* (Mineola, New York: Dover Publishing, 1996).

107. C. I. Bayly, P. Cieplak, W. Cornell, P. A. Kollman, A well-

behaved electrostatic potential based method using charge restraints for deriving atomic charges: the RESP model. *J. Phys. Chem.* **97**, 10269-10280 (1993).

108. W. D. Cornell, P. Cieplak, C. I. Bayly, P. A. Kollmann, Application of RESP charges to calculate conformational energies, hydrogen bond energies, and free energies of solvation. *J. Am. Chem. Soc.* **115**, 9620-9631 (1993).

109. J. Wang, R. M. Wolf, J. W. Caldwell, P. A. Kollman, D. A. Case, Development and testing of a general amber force field. *J. Comput. Chem.* **25**, 1157-1174 (2004).

110. G. W. T. M. J. Frisch, H. B. Schlegel, G. E. Scuseria, M. A. Robb, J. R. Cheeseman, G. Scalmani, V. Barone, B. Mennucci, G. A. Petersson, H. Nakatsuji, M. Caricato, X. Li, H. P. Hratchian, A. F. Izmaylov, J. Bloino, G. Zheng, J. L. Sonnenberg, M. Hada, M. Ehara, K. Toyota, R. Fukuda, J. Hasegawa, M. Ishida, T. Nakajima, Y. Honda, O. Kitao, H. Nakai, T. Vreven, J. A. Montgomery, Jr., J. E. Peralta, F. Ogliaro, M. Bearpark, J. J. Heyd, E. Brothers, K. N. Kudin, V. N. Staroverov, R. Kobayashi, J. Normand, K. Raghavachari, A. Rendell, J. C. Burant, S. S. Iyengar, J. Tomasi, M. Cossi, N. Rega, J. M. Millam, M. Klene, J. E. Knox, J. B. Cross, V. Bakken, C. Adamo, J. Jaramillo, R. Gomperts, R. E. Stratmann, O. Yazyev, A. J. Austin, R. Cammi, C. Pomelli, J. W. Ochterski, R. L. Martin, K. Morokuma, V. G. Zakrzewski, G. A. Voth, P.

Salvador, J. J. Dannenberg, S. Dapprich, A. D. Daniels, Ö. Farkas, J. B. Foresman, J. V. Ortiz, J. Cioslowski, and D. J. Fox. (Gaussian, Inc., Wallingford CT, 2009).

111. V. Hornak et al., Comparison of multiple Amber force fields and development of improved protein backbone parameters. *Proteins* **65**, 712–725 (2006).

112. W. L. Jorgensen, J. Chandrasekhar, J. D. Madura, R. W. Impey, M. L. Klein, Comparison of simple potential functions for simulating liquid water. *J. Chem. Phys.* **79**, 926–935 (1983).

113. I.-S. Park et al., Designer Nanorings with Functional Cavities from Self-Assembling β-Sheet Peptides. *Chem. Asian. J.* **6**, 452–458 (2011).

114. W. Li, J. Li, M. Lee, Fabrication of artificial toroid nanostructures by modified [small beta]-sheet peptides. *Chem. Commun. (Camb.)* **49**, 8238–8240 (2013).

115. R. K. Dennington, Todd; Millam, John. (Semichem Inc., Shawnee Mission, KS, 2009).

# Appendix

## AP.I-1. Temperatures (K) for REMD

(1) For residues 101-140:

290.000, 294.500, 300.000, 306.200, 313.400, 321.500, 330.500, 340.400, 351.200, 362.900, 375.500, 389.000, 403.400, 418.700, 434.900, 452.000, 470.000, 488.900, 508.700, 529.400, 551.000, 573.500, 596.900, 621.200

(2) For residues 61-140:

282.779, 291.262, 300.000, 309.000, 318.270, 327.818, 337.653, 347.782, 358.216, 368.962, 380.031, 391.432, 403.175, 415.270, 427.728, 440.560, 453.777, 467.390, 481.412, 495.854, 510.730, 526.052, 541.833, 558.088, 574.831, 592.076, 609.838, 628.134, 646.978, 666.387, 686.378, 706.969, 728.178, 750.023

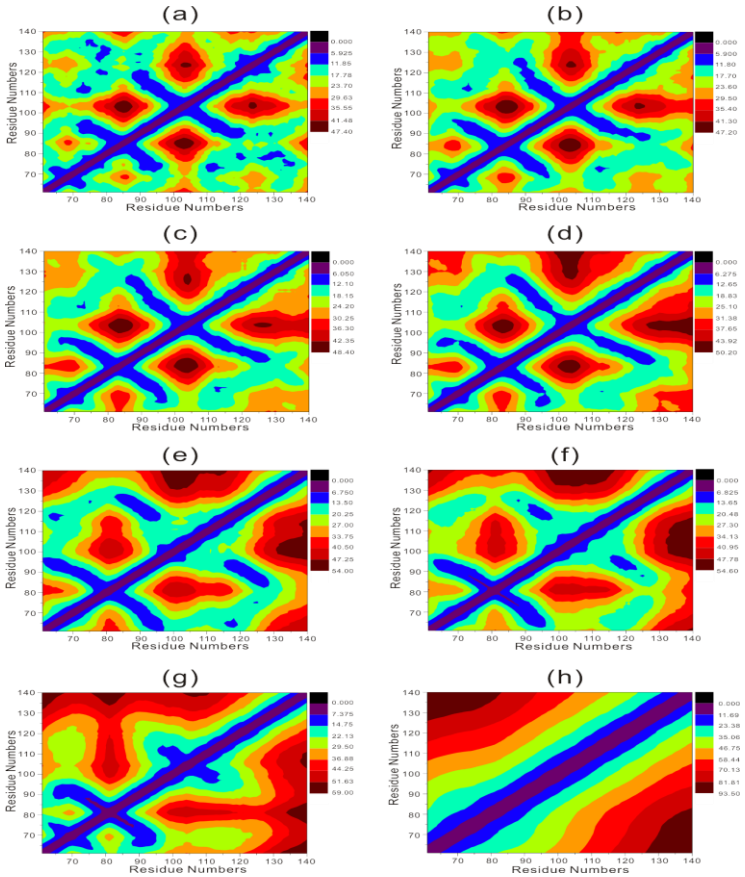


**Fig. AP.I−1−1.** Distance matrices for WT of residues 61−140 at the neutral in accordance with temperatures: (a) 283 K, (b) 291 K, (c) 300 K, (d) 309 K, (e) 318 K, (f) 328 K, (g) 338 K, and (h) 348 K. Cross points between abscissas and ordinates denote distances between $\alpha$−carbons of residues. Unit is the angstrom.

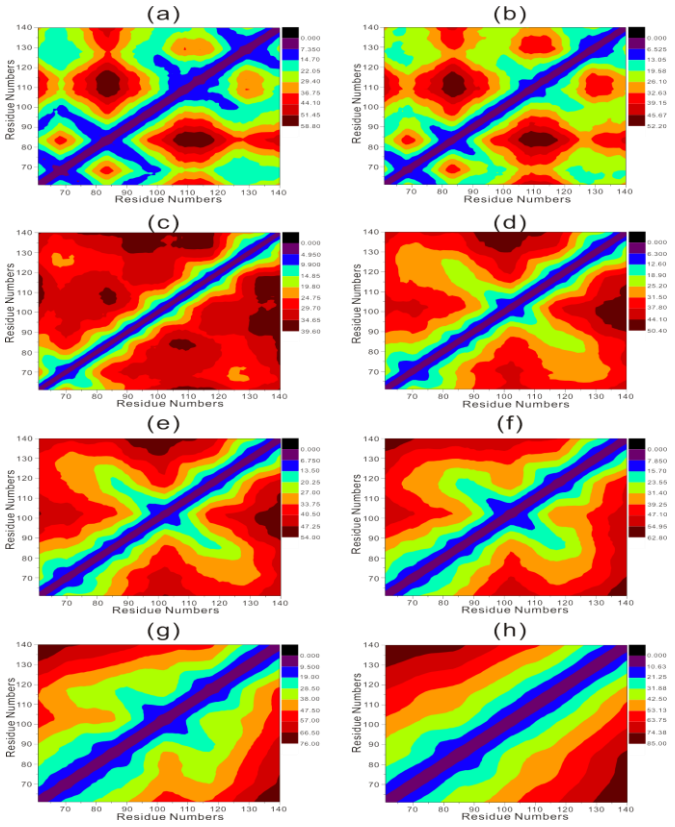


**Fig. AP.I−1−2.** Distance matrices for WT of residues 61−140 at the acidic in accordance with temperatures: (a) 283 K, (b) 291 K, (c) 300 K, (d) 309 K, (e) 318 K, (f) 328 K, (g) 338 K, and (h) 348 K. Cross points between abscissas and ordinates denote distances between $\alpha$−carbons of residues. Unit is the angstrom.

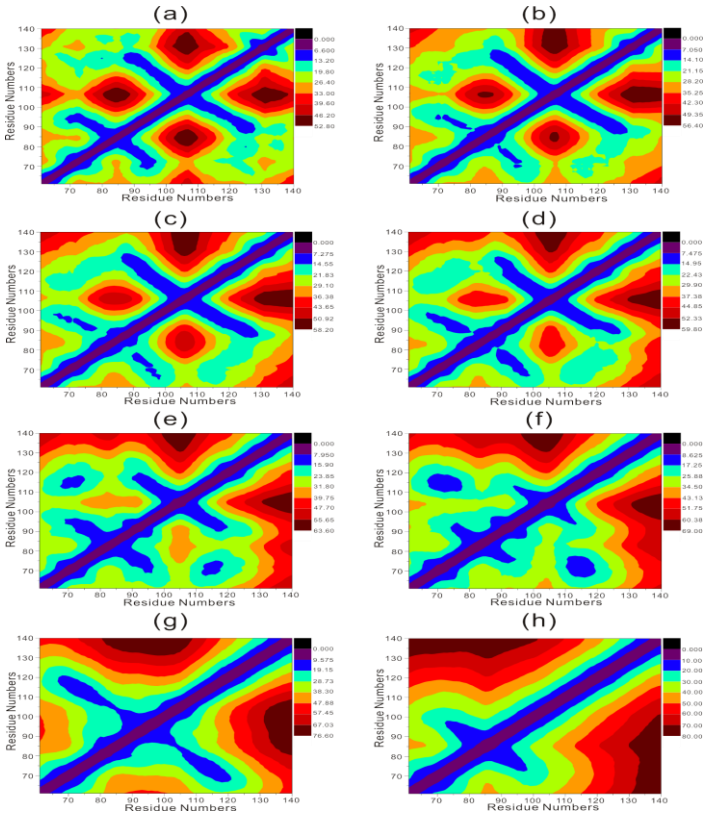


**Fig. AP.I-1-3.** Distance matrices for P(108,117,120,128,138)A mutant of residues 61-140 at the neutral in accordance with temperatures: (a) 283 K, (b) 291 K, (c) 300 K, (d) 309 K, (e) 318 K, (f) 328 K, (g) 338 K, and (h) 348 K. Cross points between abscissas and ordinates denote distances between $\alpha$-carbons of residues. Unit is the angstrom.

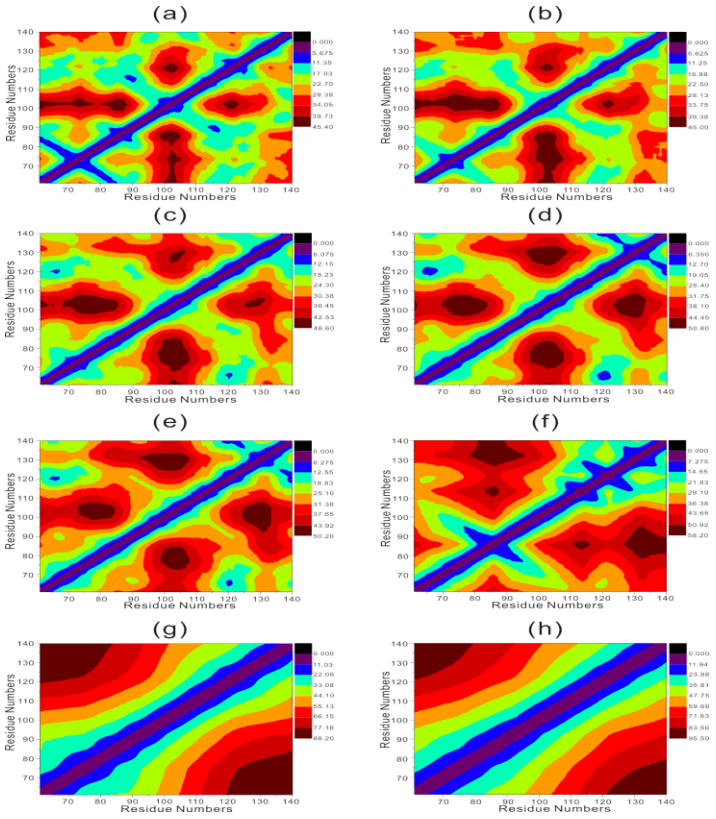


**Fig. AP.I−1−4.** Distance matrices for P(108,117,120,128,138)A mutant of residues 61−140 at the acidic in accordance with temperatures: (a) 283 K, (b) 291 K, (c) 300 K, (d) 309 K, (e) 318 K, (f) 328 K, (g) 338 K, and (h) 348 K. Cross points between abscissas and ordinates denote distances between $\alpha$−carbons of residues. Unit is the angstrom.

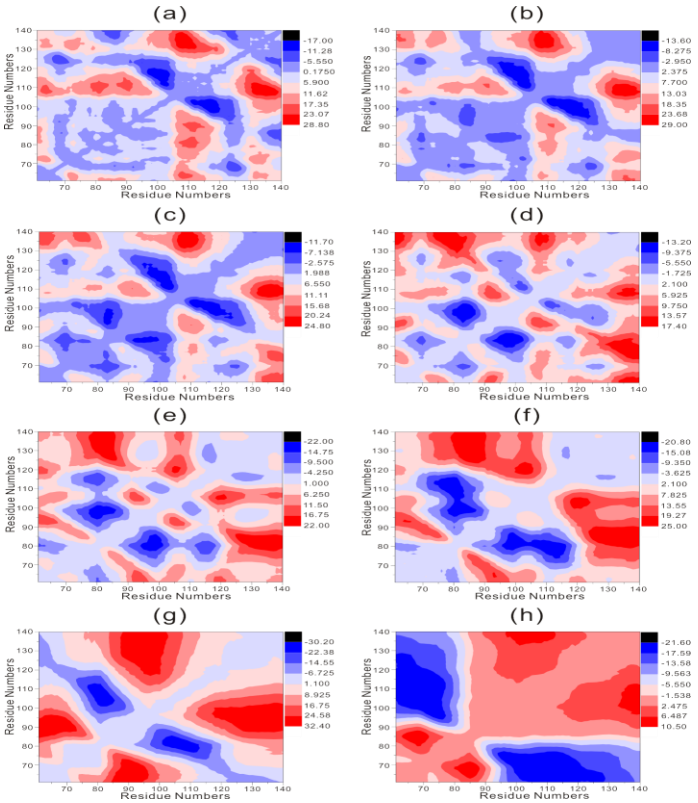


**Fig. AP.I−1−5.** Difference matrices of distance matrices, subtraction of P(108,117,120,128,138)A mutant from WT for residues 61−140 at the neutral in accordance with temperatures: (a) 283 K, (b) 291 K, (c) 300 K, (d) 309 K, (e) 318 K, (f) 328 K, (g) 338 K, and (h) 348 K. Cross points between abscissas and ordinates denote distances between $\alpha$−carbons of residues. Unit is the angstrom. Reds display regions for P(108,117,120,128,138)A mutant and blues for WT.

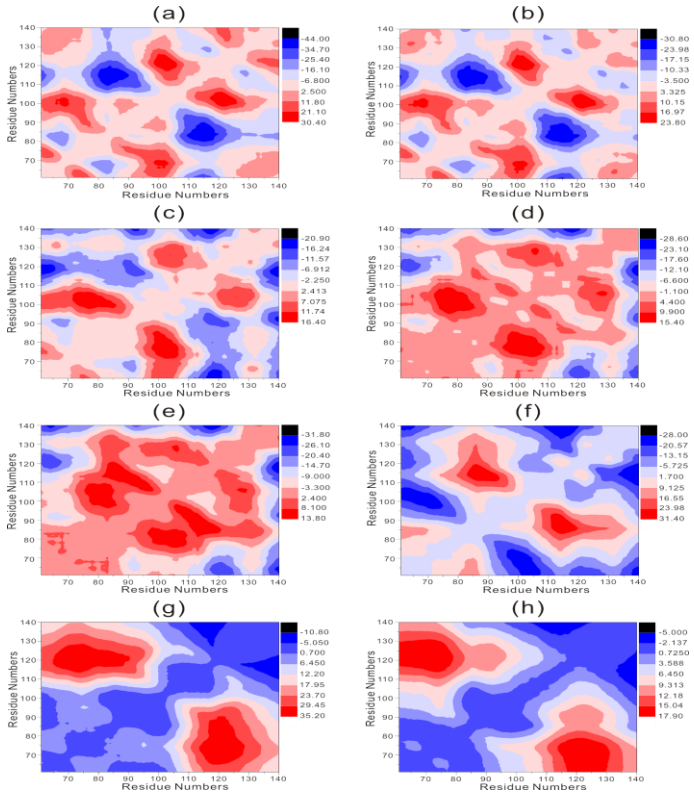


**Fig. AP.I-1-6.** Difference matrices of distance matrices, subtraction of P(108,117,120,128,138)A mutant from WT for residues 61-140 at the acidic in accordance with temperatures: (a) 283 K, (b) 291 K, (c) 300 K, (d) 309 K, (e) 318 K, (f) 328 K, (g) 338 K, and (h) 348 K. Cross points between abscissas and ordinates denote distances between $\alpha$-carbons of residues. Unit is the angstrom. Reds display regions for P(108,117,120,128,138)A mutant and blues for WT.

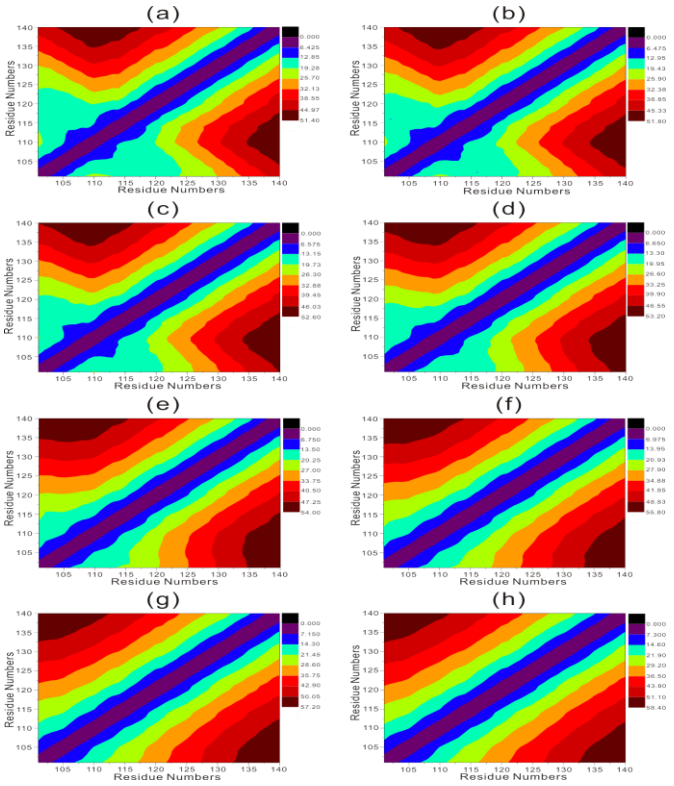


**Fig. AP.I−1−7.** Distance matrices for WT of residues 101−140 at the neutral in accordance with temperatures: (a) 290 K, (b) 294 K, (c) 300 K, (d) 306 K, (e) 313 K, (f) 322 K, (g) 330 K, and (h) 340 K. Cross points between abscissas and ordinates denote distances between $\alpha$−carbons of residues. Unit is the angstrom.

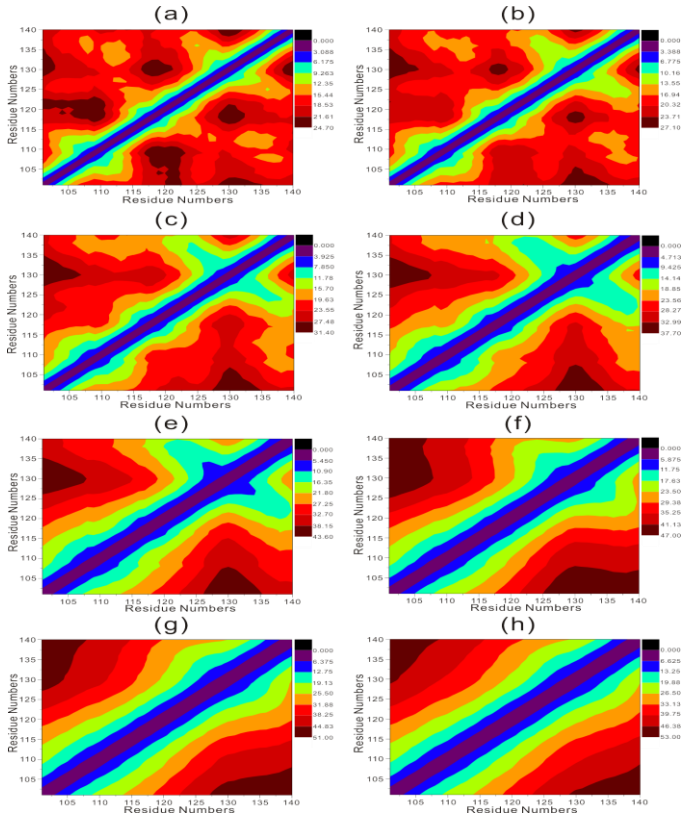


**Fig. AP.I-1-8.** Distance matrices for WT of residues 101-140 at the acidic in accordance with temperatures: (a) 290 K, (b) 294 K, (c) 300 K, (d) 306 K, (e) 313 K, (f) 322 K, (g) 330 K, and (h) 340 K. Cross points between abscissas and ordinates denote distances between $\alpha$-carbons of residues. Unit is the angstrom.

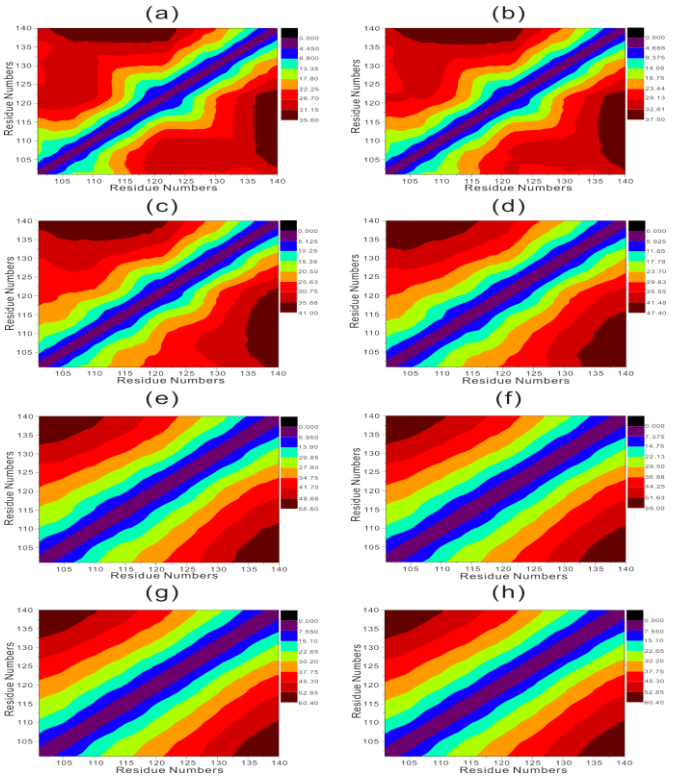


**Fig. AP.I-1-9.** Distance matrices for P(108,117,120,128,138)A mutant of 101-140 at the neutral in accordance with temperatures: (a) 290 K, (b) 294 K, (c) 300 K, (d) 306 K, (e) 313 K, (f) 322 K, (g) 330 K, and (h) 340 K. Cross points between abscissas and ordinates denote distances between $\alpha$-carbons of residues. Unit is the angstrom.

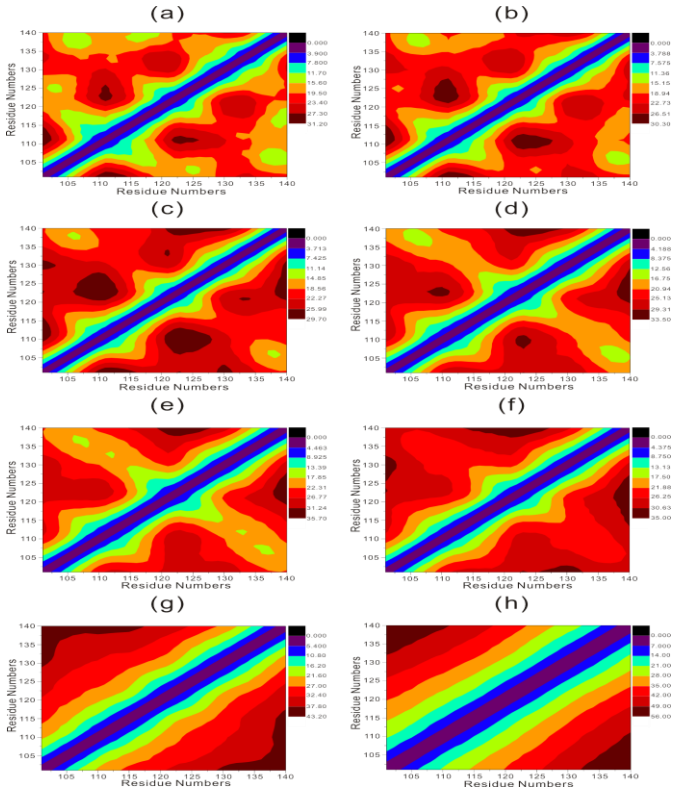


**Fig. AP.I−1−10.** Distance matrices for P(108,117,120,128,138)A mutant of residues 101−140 at the acidic in accordance with temperatures: (a) 290 K, (b) 294 K, (c) 300 K, (d) 306 K, (e) 313 K, (f) 322 K, (g) 330 K, and (h) 340 K. Cross points between abscissas and ordinates denote distances between $\alpha$−carbons of residues. Unit is the angstrom.

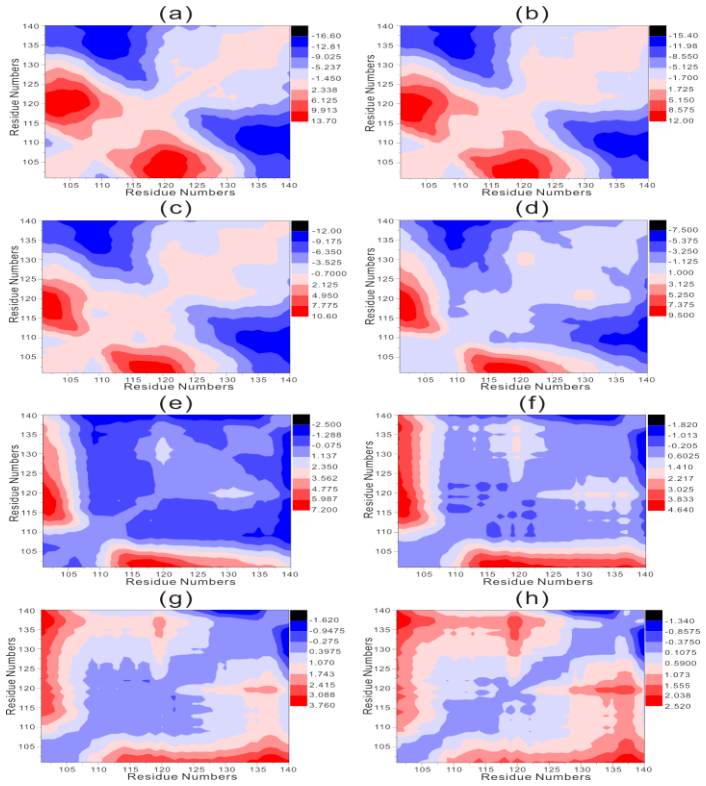


**Fig. AP.I−1−11.** Difference matrices of distance matrices, subtraction of P(108,117,120,128,138)A mutant from WT for residues 101−140 at the neutral in accordance with temperatures: (a) 290 K, (b) 294 K, (c) 300 K, (d) 306 K, (e) 313 K, (f) 322 K, (g) 330 K, and (h) 340 K. Cross points between abscissas and ordinates denote distances between $\alpha$−carbons of residues. Unit is the angstrom. Reds display regions for P(108,117,120,128,138)A mutant and blues for WT.

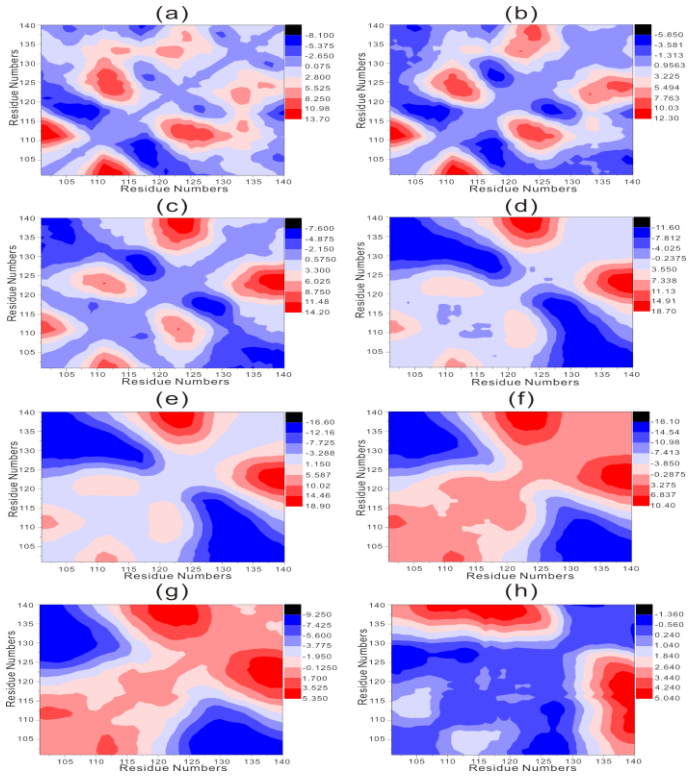


**Fig. AP.I-1-12.** Difference matrices of distance matrices, subtraction of P(108,117,120,128,138)A mutant from WT for residues 101-140 at the acidic in accordance with temperatures: (a) 290 K, (b) 294 K, (c) 300 K, (d) 306 K, (e) 313 K, (f) 322 K, (g) 330 K, and (h) 340 K. Cross points between abscissas and ordinates denote distances between $\alpha$-carbons of residues. Unit is the angstrom. Reds display regions for P(108,117,120,128,138)A mutant and blues for WT.

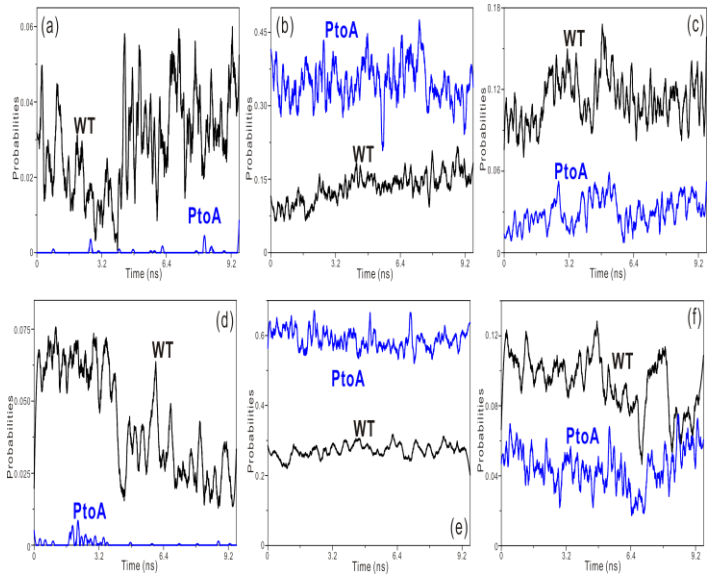


**Fig. AP.I−1−13.** Time evolution of the contents of the secondary structures for only the NAC domains (residues 101−140): (a) parallel $\beta$−sheet at the neutral condition, (b) antiparallel $\beta$−sheet at the neutral, (c) turn at the neutral, (d) parallel $\beta$−sheet at the acidic, (e) antiparallel $\beta$−sheet at the acidic, and (f) turn at the acidic. P−to−A means P(108,117,120,128,138)A mutant.

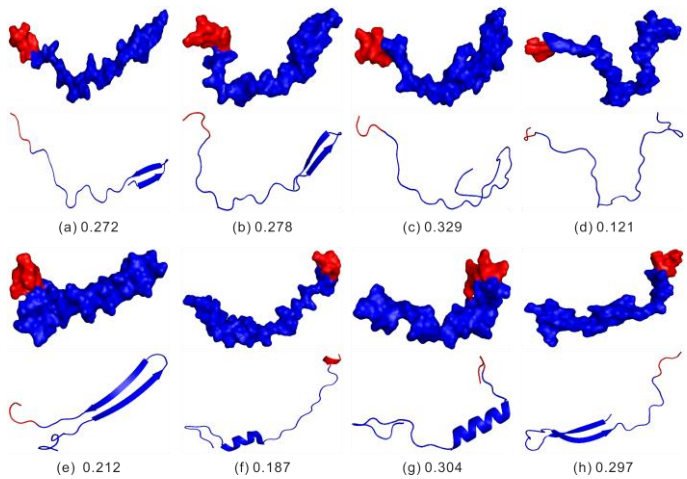


**Fig. AP.I−1−14.** Representative conformers of only the acidic domains (residues 101−140) at the neutral from clustering analyses at 300 K based on

the k-means algorithm(*54*): (a)-(d) for WT, (e)-(h) for P(108,117,120,128,138)A mutant. Reds display the N-terminal groups and numbers occurrence. The first row is the surface representation and the second row the cartoon in each conformer.

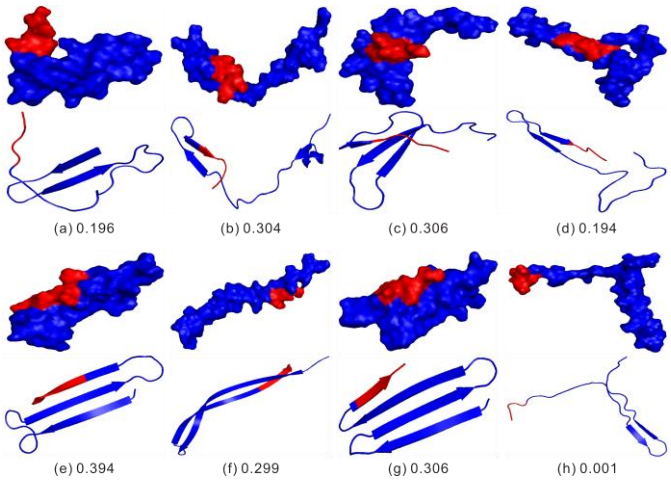


**Fig. AP.I-1-15.** Representative conformers of only the acidic domains (residues 101-140) at the acidic from clustering analyses at 300 K based on the k-means algorithm(*54*): (a)-(d) for WT, (e)-(h) for P(108,117,120,128,138)A mutant. Reds display the N-terminal groups and numbers occurrence. The first row is the surface representation and the second row the cartoon in each conformer.

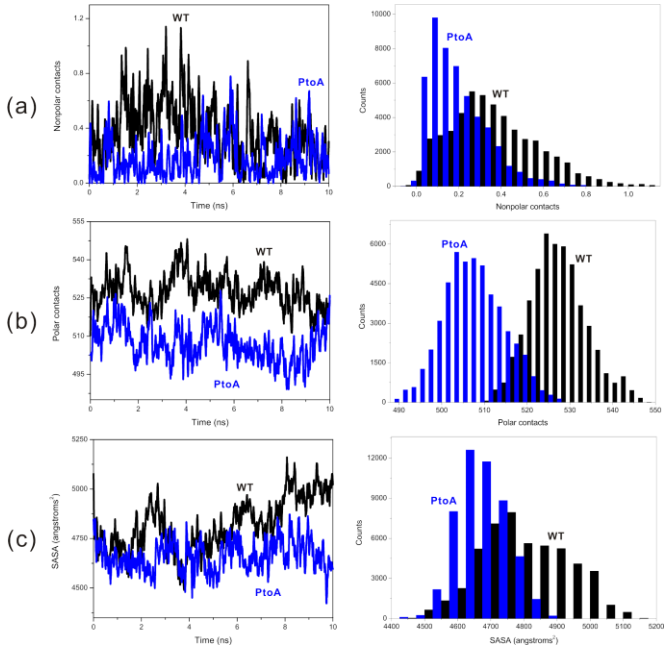


**Fig. AP.I-1-16.** Time evolution of nonpolar/polar contacts and SASA for only the NAC domains (residue 101-140) at the neutral and 300 K: (a) nonpolar contacts, (b) polar contacts, and (c) SASA. P-to-A means P(108,117,120,128,138)A mutant.

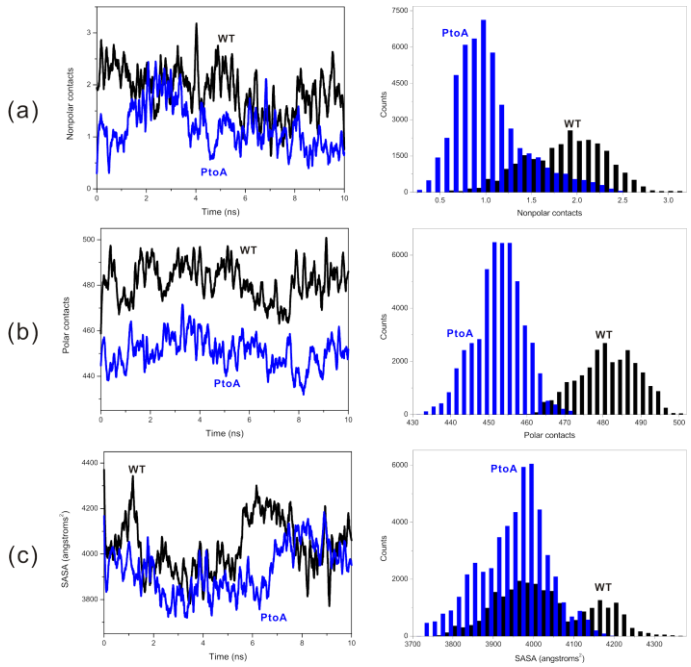


**Fig. AP.I-1-17.** Time evolution of nonpolar/polar contacts and SASA for only the NAC domains (residues 101-140) at the acidic and 300 K: (a) nonpolar contacts, (b) polar contacts, and (c) SASA. P-to-A means P(108,117,120,128,138)A mutant.

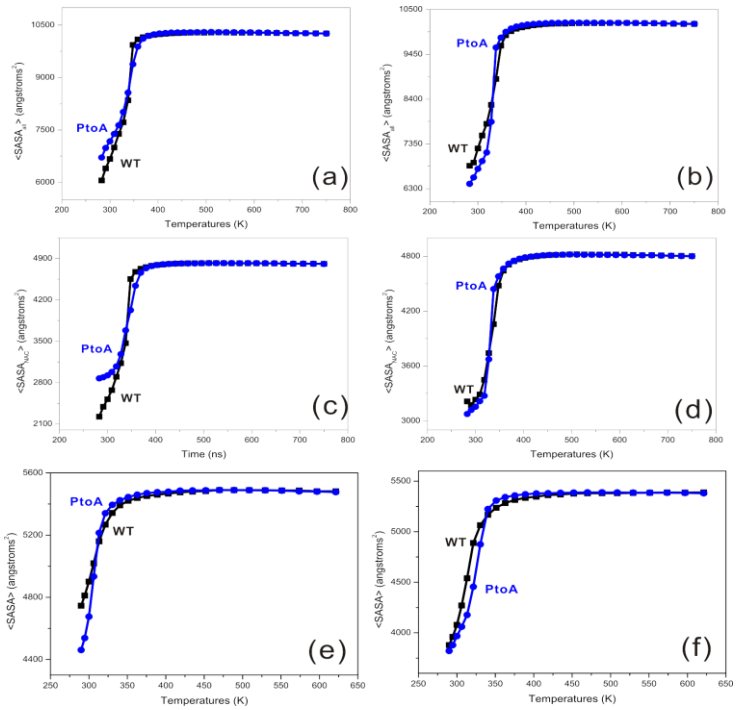


**Fig. AP.I-1-18.** SASA dependent on temperatures: (a) residues 61-140 at the neutral, (b) residues 61-140 at the acidic, (c) only the NAC domain of residues 61-140 at the neutral (d) only the NAC domain of residues 61-140 at the acidic, (e) residues 101-140 at the neutral, and (f) residues 101-140 at the acidic. P-to-A means P(108,117,120,128,138)A mutant.

## AP.I-2. Temperatures (K) for REMD: ($A\beta_{40/42}$)

282.65, 291.25, 300.00, 309.11, 318.42, 328.06, 338.00, 348.23, 358.75, 369.59, 380.74, 392.22, 404.03, 416.18, 428.93, 441.74, 454.99, 468.62, 482.64, 497.08, 511.93, 527.19, 542.91, 559.09, 575.73, 592.92

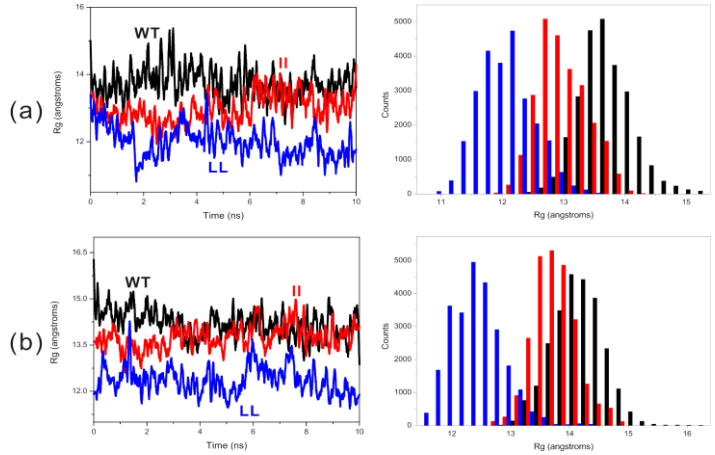


**Fig. AP.I−2−1.** Rg for monomers at 300 K and the neutral: (a) residues 11−42 and (b) residues 11−40. The II and LL denote the F(19,20)I and F(19,20)L mutants.

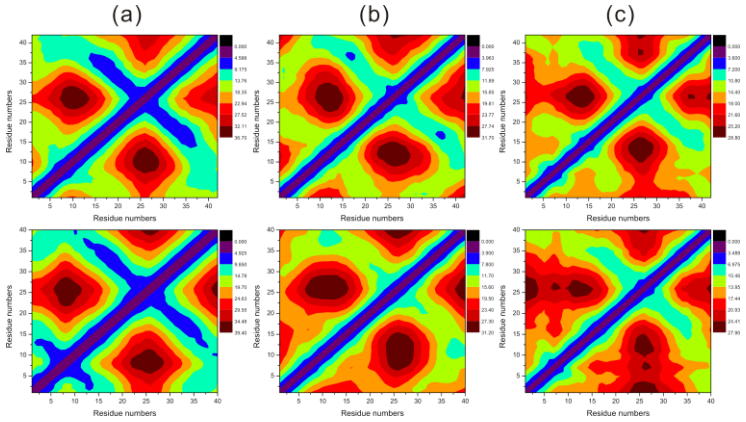


**Fig. AP.I−2−2.** Distance matrices for monomers at 300 K and the neutral: (a) WT, (b) F(19,20)I mutant, and (c) F(19,20)L mutant. The first row is for A$\beta_{42}$ and the second for A$\beta_{40}$. Unit of length is angstrom.

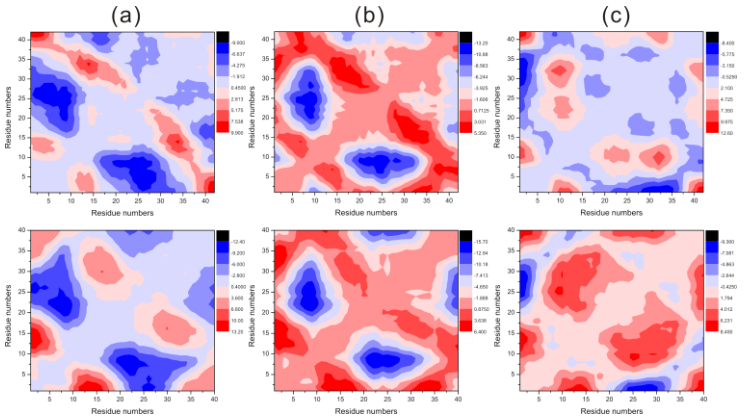


**Fig. AP.I-2-3.** Difference matrices of distance matrices for monomers at 300 K and the neutral: (a) subtraction of distance matrix of F(19,20)I mutant from distance matrix of WT, (b) subtraction of distance matrix of F(19,20)L mutant from distance of WT, and (c) subtraction of distance matrix of F19,20)I mutant from distance matrix of F(19,20)L mutant. The first row is for A$\beta_{42}$ and the second for A$\beta_{40}$. Unit of length is angstrom.

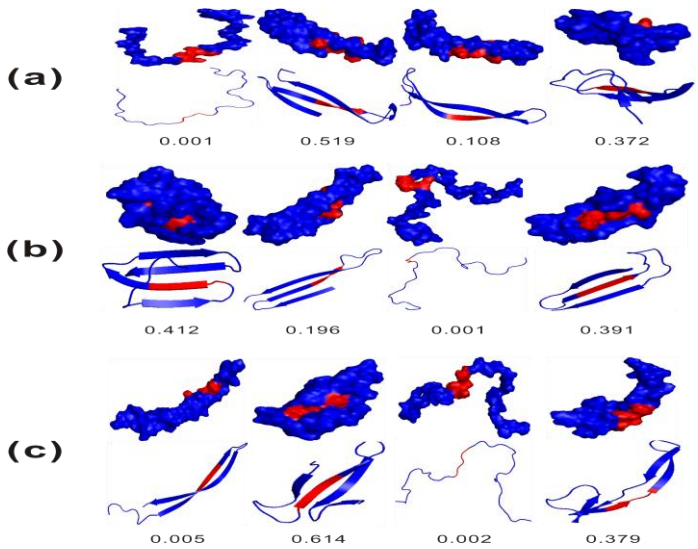


**Fig. AP.I-2-4.** Representative conformers of monomers of A$\beta_{42}$ at 300 K and the neutral: (a) WT, (b) F(19,20)I mutant, and (c) F(19,20)L mutant. In each conformer, the first rows are represented by the surface representation, the seconds by the cartoon, and the thirds their occurrences. Reds are for residues

16-20.

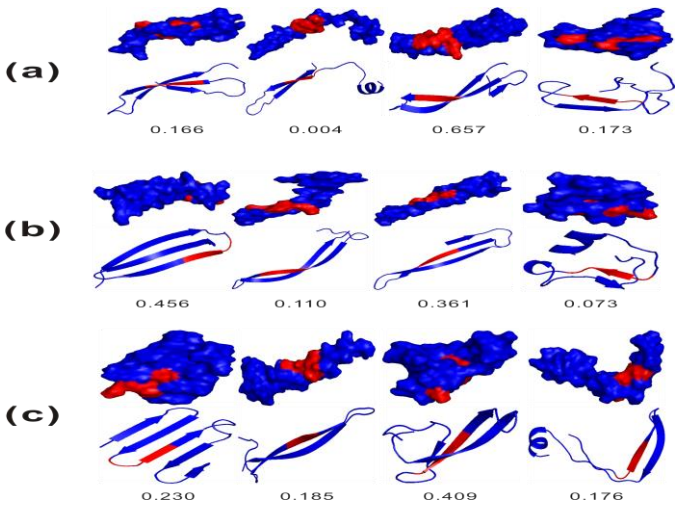


**Fig. AP.I-2-5.** Representative conformers of monomers of A$\beta_{40}$ at 300 K and the neutral: (a) WT, (b) F(19,20)I mutant, and (c) F(19,20)L mutant. In each conformer, the first rows are represented by the surface representation, the seconds by the cartoon, and the thirds their occurrences. Reds are for residues 16-20.

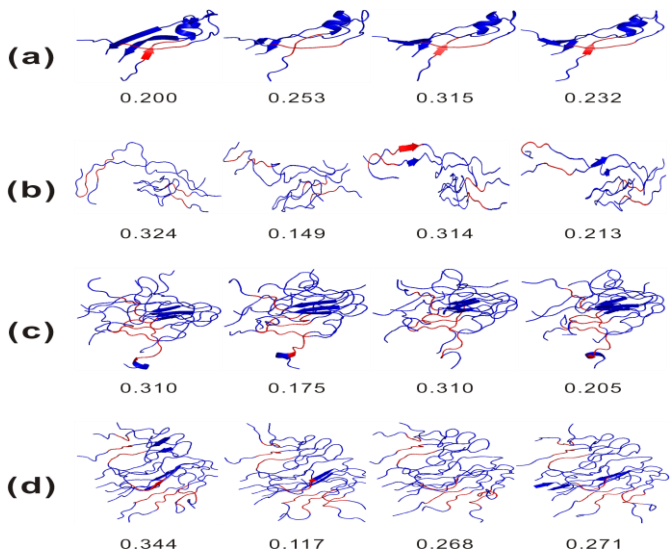


**Fig. AP.I-2-6.** Representative conformers of protofilaments of the Bertini's

model from WT of A$\beta_{11-42}$ at 300 K and the neutral: (a) 2−mer, (b) 4−mer, (c) 6−mer, and (d) 8−mer. In each conformer, digits are their occurrences. Reds are for residues 16−20.

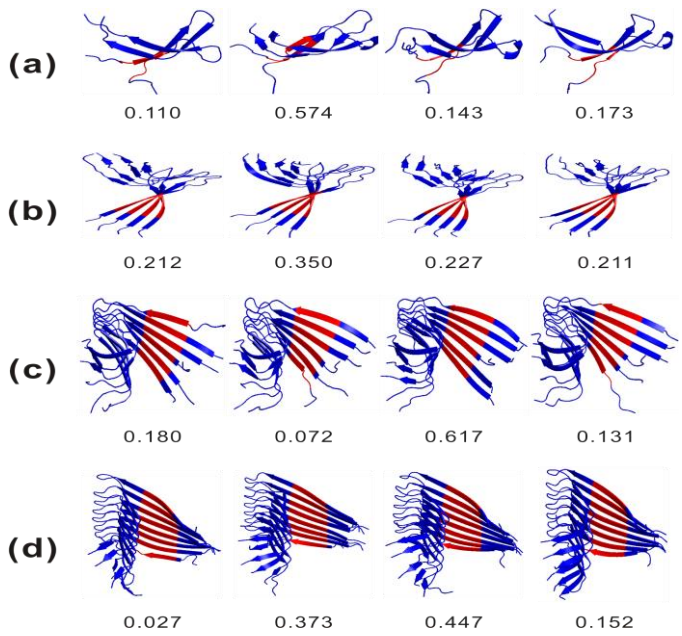


**Fig. AP.I−2−7.** Representative conformers of protofilaments of the Tycko's model from WT of A$\beta_{11-42}$ at 300 K and the neutral: (a) 2−mer, (b) 4−mer, (c) 6−mer, and (d) 8−mer. In each conformer, digits are their occurrences. Reds are for residues 16−20.

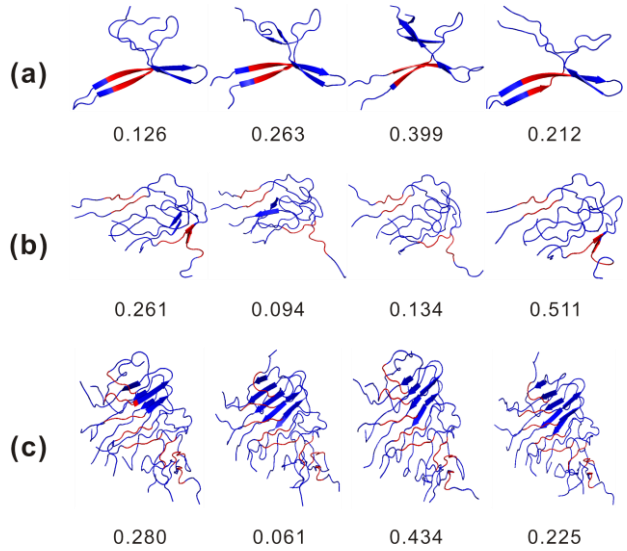


**Fig. AP.I-2-8.** Representative conformers of protofilaments of the Bertini's model from F(19,20)I mutant of A$\beta_{11-42}$ at 300 K and the neutral: (a) 2-mer, (b) 4-mer, and (c) 8-mer. In each conformer, digits are their occurrences. Reds are for residues 16-20.

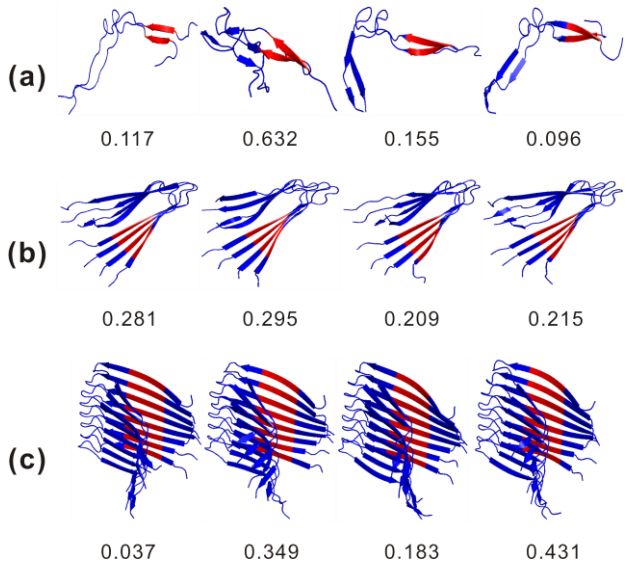


**Fig. AP.I-2-9.** Representative conformers of protofilaments of the Tycko's model from F(19,20)I mutant of A$\beta_{11-42}$ at 300 K and the neutral: (a) 2-mer, (b) 4-mer, and (c) 8-mer. In each conformer, digits are their occurrences.

Reds are for residues 16−20.

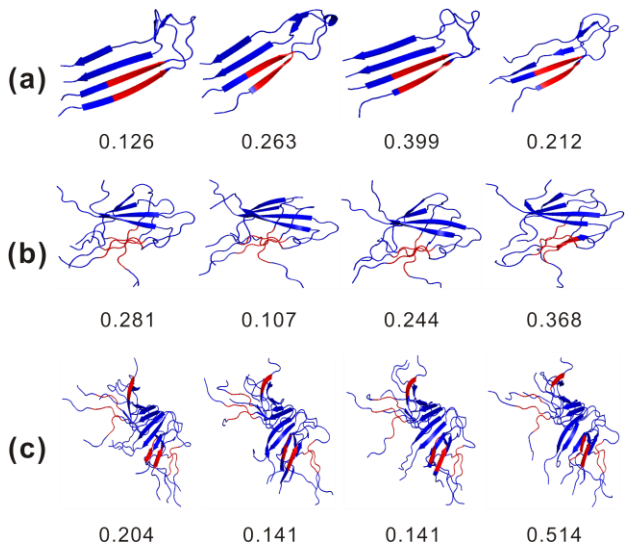


**Fig. AP.I−2−10.** Representative conformers of protofilaments of the Bertini's model from F(19,20)L mutant of A$\beta_{11-42}$ at 300 K and the neutral: (a) 2−mer, (b) 4−mer, and (c) 8−mer. In each conformer, digits are their occurrences. Reds are for residues 16−20.

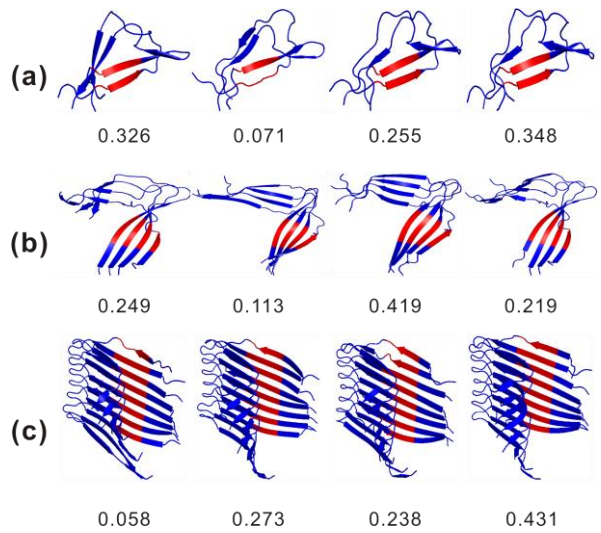


**Fig. AP.I−2−11.** Representative conformers of protofilaments of the Tycko's

model from F(19,20)L mutant of A$\beta_{11-42}$ at 300 K and the neutral: (a) 2−mer, (b) 4−mer, and (c) 8−mer. In each conformer, digits are their occurrences. Reds are for residues 16−20.

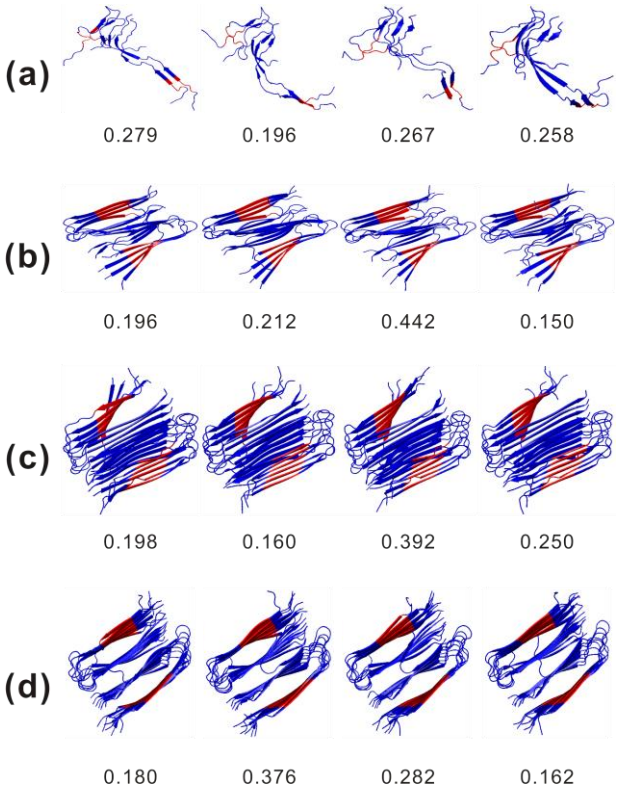


**Fig. AP.I−2−12.** Representative conformers of protofibrils of the Bertini's model from WT of A$\beta_{11-42}$ at 300 K and the neutral: (a) 2−mer, (b) 4−mer, (c) 6−mer, and (d) 8−mer. In each conformer, digits are their occurrences. Reds are for residues 16−20.

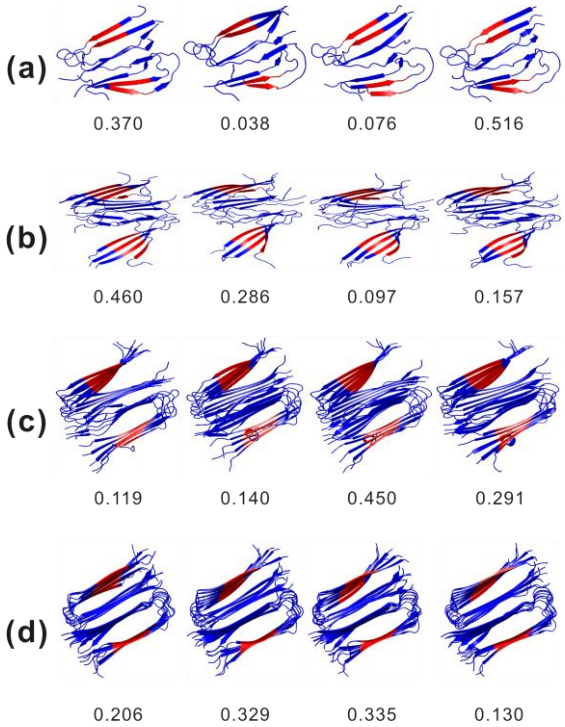


**Fig. AP.I-2-13.** Representative conformers of protofibrils of the Tycko's model from WT of A$\beta_{11-42}$ at 300 K and the neutral: (a) 2-mer, (b) 4-mer, (c) 6-mer, and (d) 8-mer. In each conformer, digits are their occurrences. Reds are for residues 16-20.

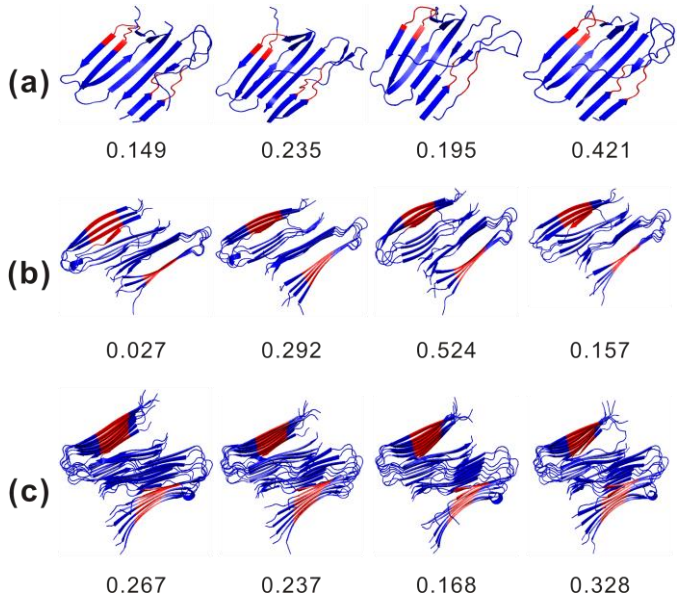


**Fig. AP.I-2-14.** Representative conformers of protofibrils of the Bertini's model from F(19,20)I mutant of A$\beta_{11-42}$ at 300 K and the neutral: (a) 2-mer, (b) 4-mer, and (c) 8-mer. In each conformer, digits are their occurrences. Reds are for residues 16-20.

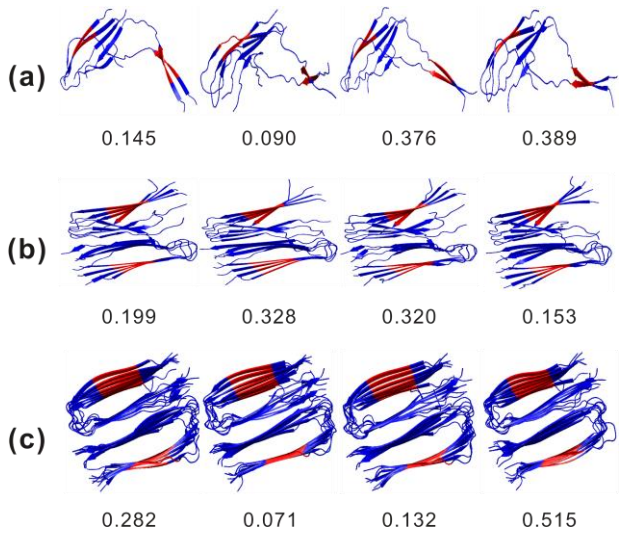


**Fig. AP.I-2-15.** Representative conformers of protofibrils of the Tycko's model from F(19,20)I mutant of A$\beta_{11-42}$ at 300 K and the neutral: (a) 2-mer, (b) 4-mer, and (c) 8-mer. In each conformer, digits are their occurrences.

Reds are for residues 16−20.

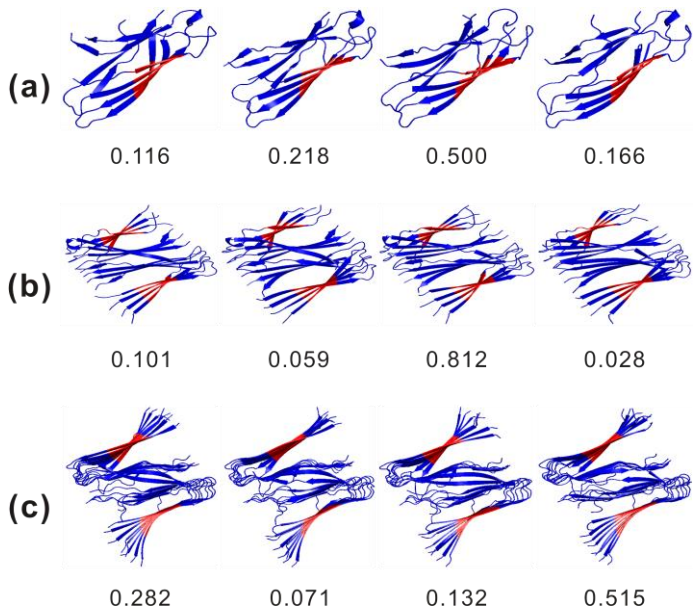


**Fig. AP.I−2−16.** Representative conformers of protofibrils of the Bertini's model from F(19,20)L mutant of A$\beta_{11-42}$ at 300 K and the neutral: (a) 2−mer, (b) 4−mer, and (c) 8−mer. In each conformer, digits are their occurrences. Reds are for residues 16−20.

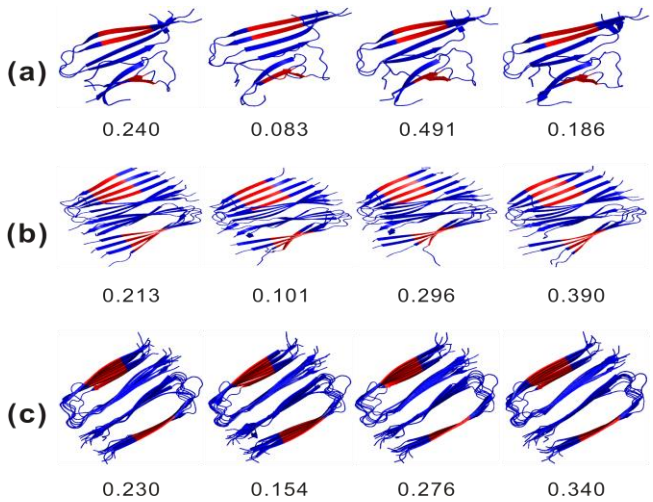


**Fig. AP.I−2−17.** Representative conformers of protofibrils of the Tycko's

model from F(19,20)L mutant of A$\beta_{11-42}$ at 300 K and the neutral: (a) 2−mer, (b) 4−mer, and (c) 8−mer. In each conformer, digits are their occurrences. Reds are for residues 16−20.

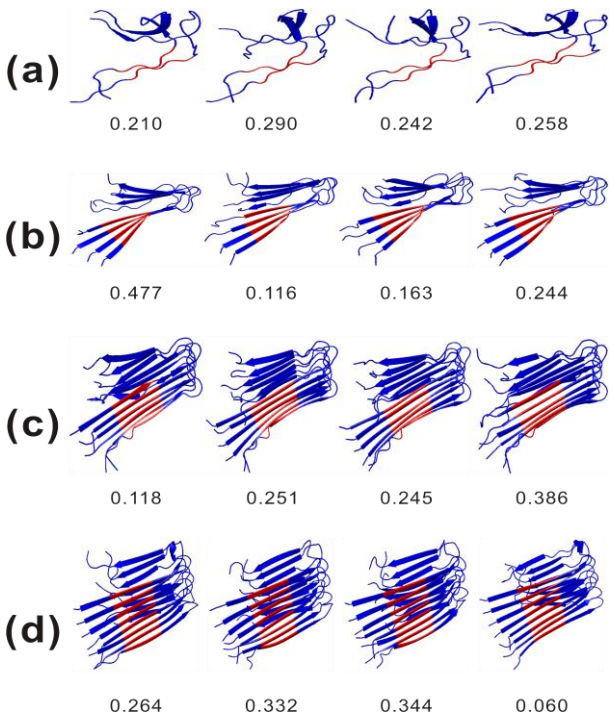


**Fig. AP.I−2−18.** Representative conformers of protofilaments of the Bertini's model from WT of A$\beta_{11-40}$ at 300 K and the neutral: (a) 2−mer, (b) 4−mer, (c) 6−mer, and (d) 8−mer. In each conformer, digits are their occurrences. Reds are for residues 16−20.

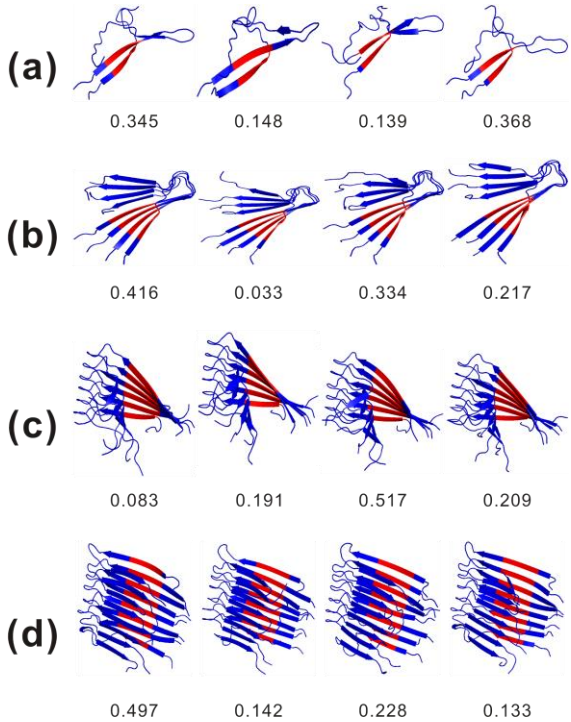


**Fig. AP.I-2-19.** Representative conformers of protofilaments of the Tycko's model from WT of A$\beta_{11-40}$ at 300 K and the neutral: (a) 2-mer, (b) 4-mer, (c) 6-mer, and (d) 8-mer. In each conformer, digits are their occurrences. Reds are for residues 16-20.

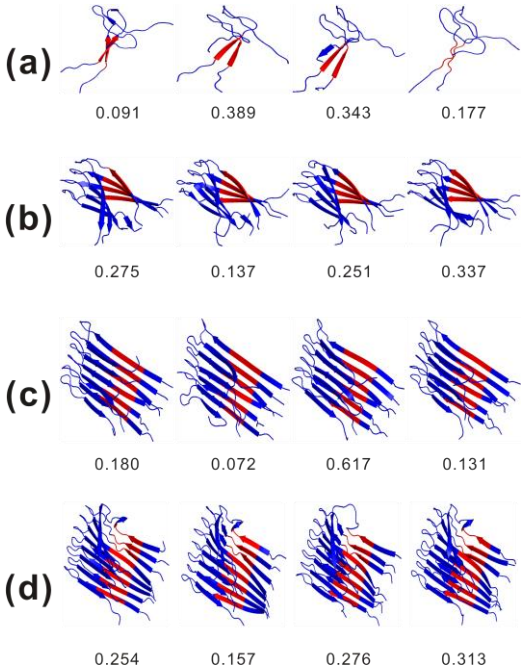


**Fig. AP.I-2-20.** Representative conformers of protofilaments of the Bertini's model from F(19,20)I mutant of A$\beta_{11-40}$ at 300 K and the neutral: (a) 2-mer, (b) 4-mer, (c) 6-mer, and (d) 8-mer. In each conformer, digits are their occurrences. Reds are for residues 16-20.

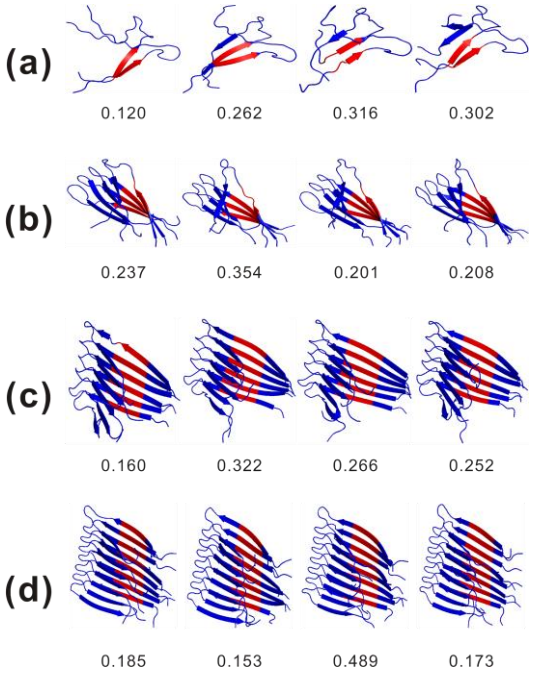


**Fig. AP.I-2-21.** Representative conformers of protofilaments of the Tycko's model from F(19,20)I mutant of A$\beta_{11-40}$ at 300 K and the neutral: (a) 2-mer, (b) 4-mer, (c) 6-mer, and (d) 8-mer. In each conformer, digits are their occurrences. Reds are for residues 16-20.

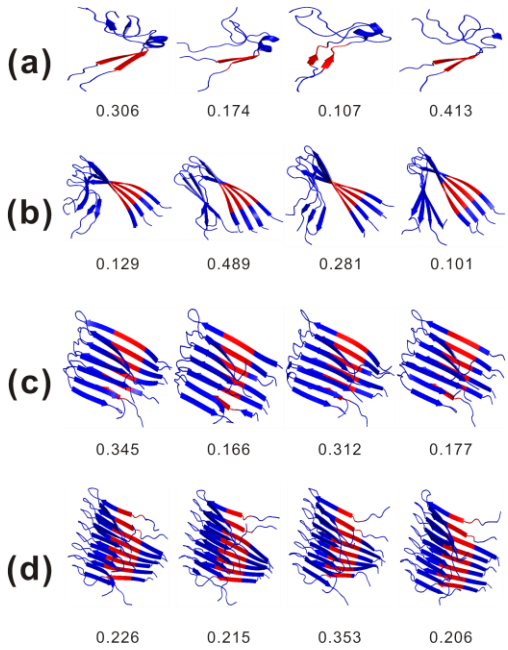


**Fig. AP.I-2-22.** Representative conformers of protofilaments of the Bertini's model from F(19,20)L mutant of A$\beta_{11-40}$ at 300 K and the neutral: (a) 2-mer, (b) 4-mer, (c) 6-mer, and (d) 8-mer. In each conformer, digits are their occurrences. Reds are for residues 16-20.

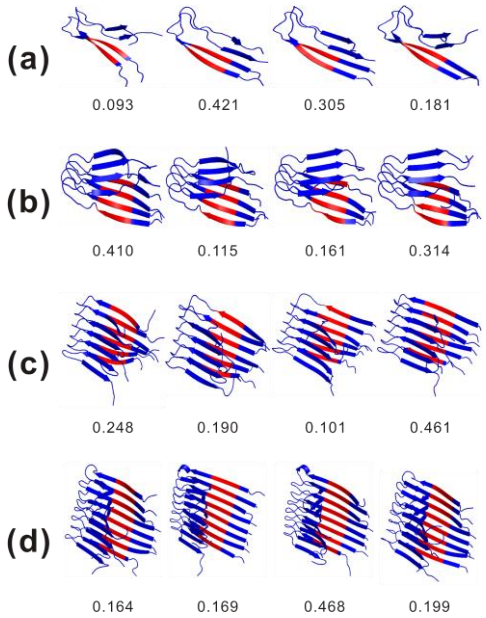

**Fig. AP.I-2-23.** Representative conformers of protofilaments of the Tycko's model from F(19,20)L mutant of A$\beta_{11-40}$ at 300 K and the neutral: (a) 2-mer, (b) 4-mer, (c) 6-mer, and (d) 8-mer. In each conformer, digits are their occurrences. Reds are for residues 16-20.

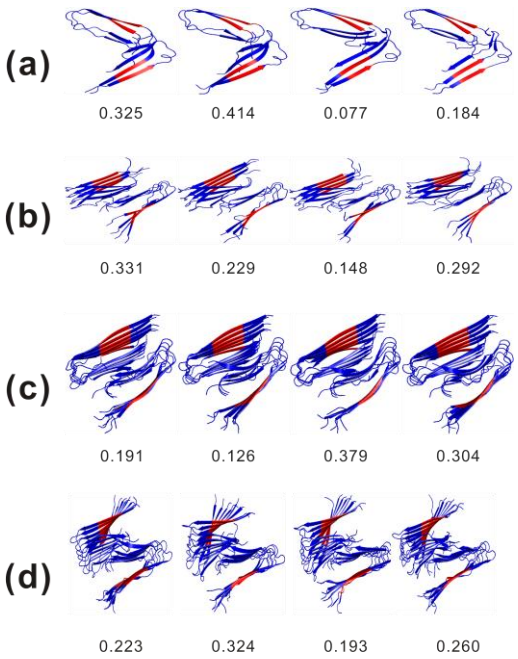


**Fig. AP.I-2-24.** Representative conformers of protofibrils of the Bertini's model from WT of A$\beta_{11-40}$ at 300 K and the neutral: (a) 2-mer, (b) 4-mer, (c) 6-mer, and (d) 8-mer. In each conformer, digits are their occurrences. Reds are for residues 16-20.

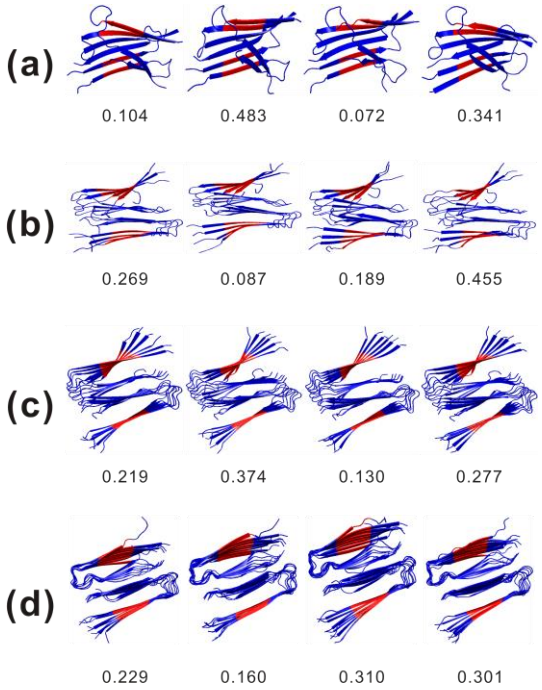


**Fig. AP.I-2-25.** Representative conformers of protofibrils of the Tycko's model from WT of A$\beta_{11-40}$ at 300 K and the neutral: (a) 2-mer, (b) 4-mer, (c) 6-mer, and (d) 8-mer. In each conformer, digits are their occurrences. Reds are for residues 16-20.

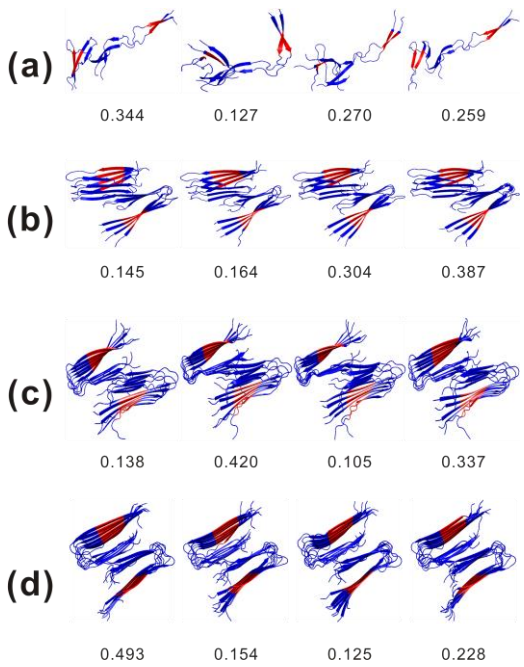


**Fig. AP.I-2-26.** Representative conformers of protofibrils of the Bertini's model from F(19,20)I mutant of A$\beta_{11-40}$ at 300 K and the neutral: (a) 2-mer, (b) 4-mer, (c) 6-mer, and (d) 8-mer. In each conformer, digits are their occurrences. Reds are for residues 16-20.

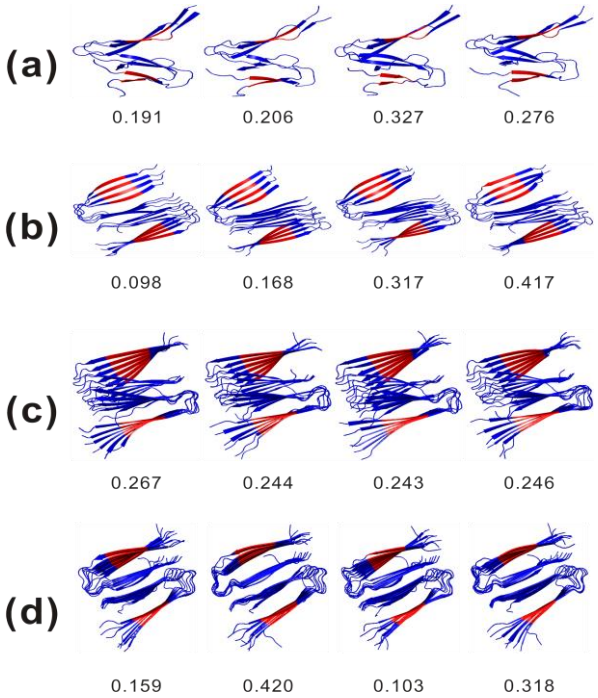


**Fig. AP.I-2-27.** Representative conformers of protofibrils of the Tycko's model from F(19,20)I mutant of A$\beta_{11-40}$ at 300 K and the neutral: (a) 2-mer, (b) 4-mer, (c) 6-mer, and (d) 8-mer. In each conformer, digits are their occurrences. Reds are for residues 16-20.

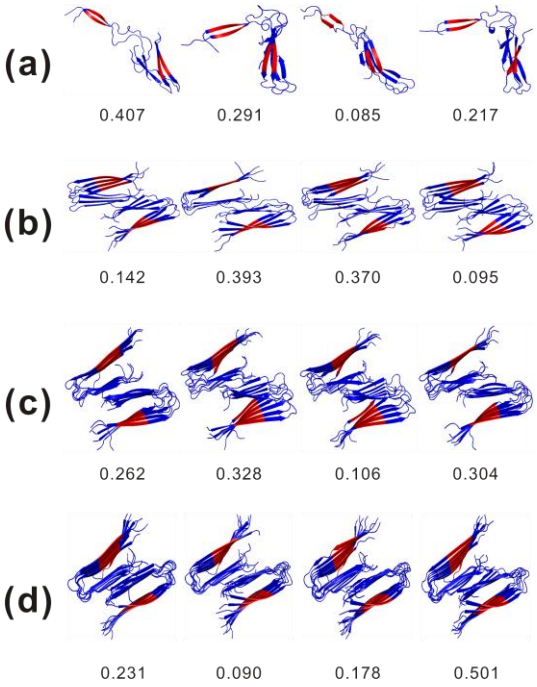


**Fig. AP.I-2-28.** Representative conformers of protofibrils of the Bertini's model from F(19,20)L mutant of A$\beta_{11-40}$ at 300 K and the neutral: (a) 2-mer, (b) 4-mer, (c) 6-mer, and (d) 8-mer. In each conformer, digits are their occurrences. Reds are for residues 16-20.

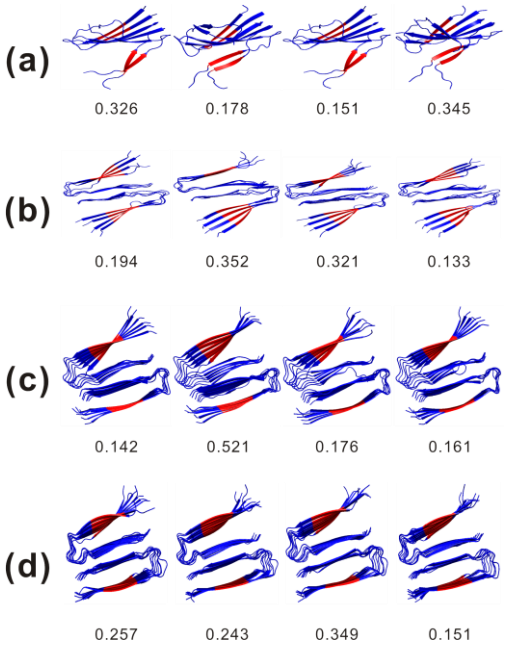


**Fig. AP.I−2−29.** Representative conformers of protofibrils of the Tycko's model from F(19,20)L mutant of A$\beta_{11-40}$ at 300 K and the neutral: (a) 2−mer, (b) 4−mer, (c) 6−mer, and (d) 8−mer. In each conformer, digits are their occurrences. Reds are for residues 16−20.

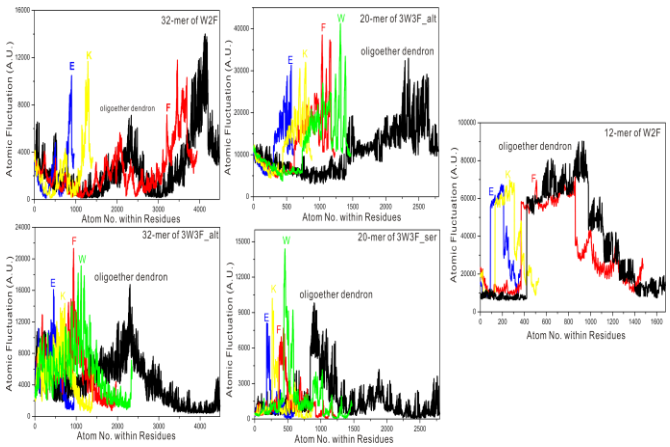


**Fig. AP.II−1.** RMSFs for broken structures of T3

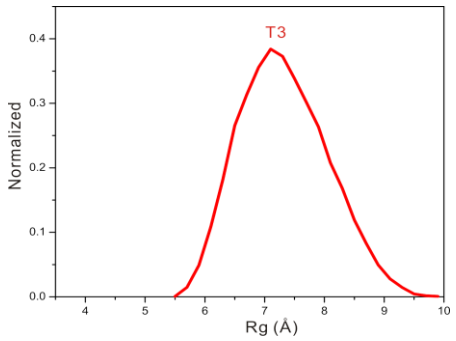


**Fig. AP.II-2.** Distribution of Rg for only oligoeher dendrons of T3.

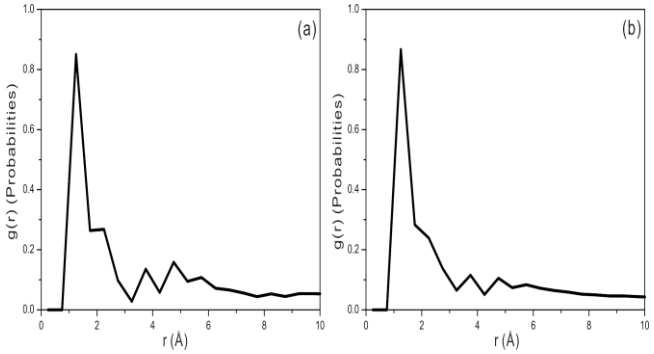


**Fig. AP.II-3.** RDF for the W-to-F mutants of T3: (a) all W-to-F mutant, and (b) serial three W-to-F mutant.

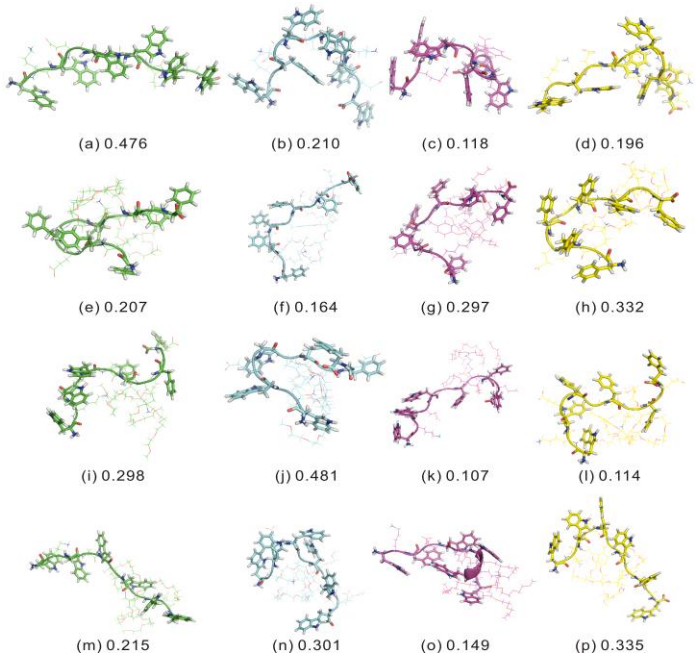


**Fig. AP.II-4.** Representative conformers of monomers of T1/T3: (a)-(d) for T1, (e)-(h) for W-to-F of T3, (i)-(l) for W(1,3,5)F of T3, and (m)-(p) for WT of T3.

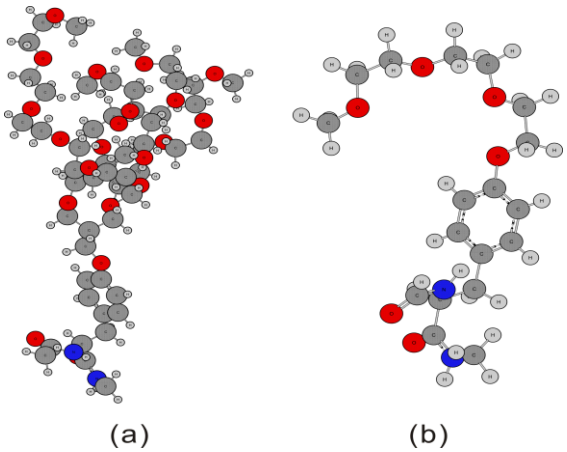


**Fig.AP.II-5**. Geometrically optimized structures of ACE-Tyr-NME capped oligoether dendron and tri(ethylene glycol) monomethoxy ether based on B3LYP/6-31G(d) (*49, 50*): (a) oligoether dendron, and (b) tri(ethylene glycol) monomethoxy ether. The visualization was done with the GaussView (*115*).

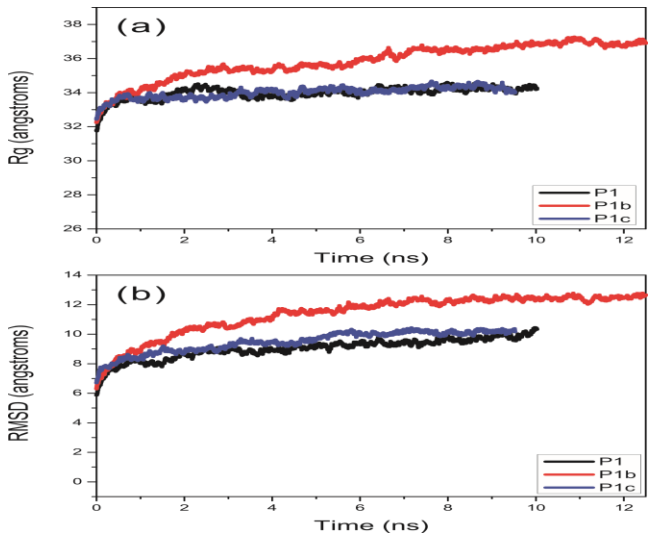


**Fig.AP.II-6.** The time evolution of Rg and RMSD for the P1, P1b, and P1c. P1, P1b, and P1c seemed to converge to the equilibria.

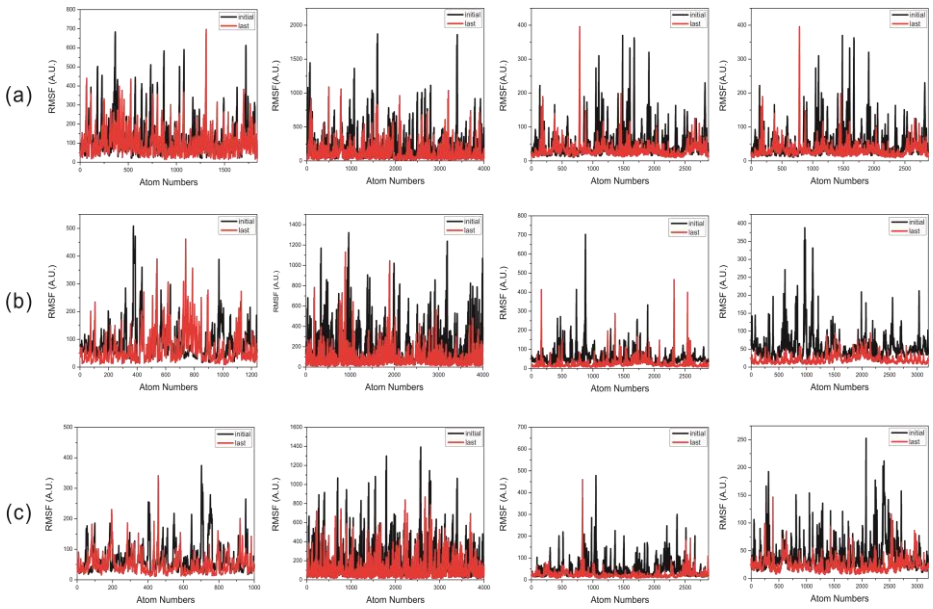


**Fig.AP.II-7.** RMSF of P1, P1b, and P1c: (a) P1, (b) P1b, and (c) P1c. The 1$^{st}$, 2$^{nd}$, 3$^{rd}$, and 4$^{th}$ are for charged residues, tri(ethylene glycol) monomethoxy ether, trp residues, and tyr residues, respectively. As time elapsed, RMSF for

P1, P1b, and P1c decreased, which implied their nanobiostructures were sustained ever since.

## AP.II-1. Parameter and topology information of the oligoether dendron for the MD simulation

### (1) frcmod file:

```
MASS

BOND
C-OS   411.3     1.343          SOURCE1   1044     0.0114     0.0171 (gaff c -os)

ANGLE
CA-C-OS     68.8       115.54     SOURCE3     5    2.1366    2.6708 (gaff ca-c -os)
C-OS-CT     63.6       115.14     SOURCE3    17    1.5416    1.8967 (gaff c -os-c3)

DIHE
CA-C-OS-CT     2     5.400         180.000              2.000         Junmei et al, 1999
(gaff X -c -os-X)

IMPROPER

NONBON
```

### (2) library file:

```
!!index array str
 "MTY"
!entry.MTY.unit.atoms table  str name  str type  int typex  int resx  int flags  int seq
int elmnt  dbl chg
 "C1" "CT" 0 1 196611 1 6 0.106672
 "C2" "CT" 0 1 196611 2 6 -0.049157
```

"O1" "OS" 0 1 196611 3 8 −0.302167

"C3" "CT" 0 1 196611 4 6 0.012491

"C4" "CT" 0 1 196611 5 6 −0.049157

"C5" "CT" 0 1 196611 6 6 0.016967

"C6" "CT" 0 1 196611 7 6 0.016967

"C7" "CT" 0 1 196611 8 6 0.016967

"C8" "CT" 0 1 196611 9 6 0.016967

"O2" "OS" 0 1 196611 10 8 −0.365417

"O3" "OS" 0 1 196611 11 8 −0.365417

"C9" "CT" 0 1 196611 12 6 0.098896

"C10" "CT" 0 1 196611 13 6 0.103787

"C11" "CT" 0 1 196611 14 6 0.098896

"C12" "CT" 0 1 196611 15 6 0.103787

"O4" "OS" 0 1 196611 16 8 −0.365417

"O5" "OS" 0 1 196611 17 8 −0.365417

"C13" "CT" 0 1 196611 18 6 0.098896

"C14" "CT" 0 1 196611 19 6 0.098896

"C15" "CT" 0 1 196611 20 6 0.103787

"C16" "CT" 0 1 196611 21 6 0.103787

"O6" "OS" 0 1 196611 22 8 −0.407742

"O7" "OS" 0 1 196611 23 8 −0.407742

"O8" "OS" 0 1 196611 24 8 −0.407742

"O9" "OS" 0 1 196611 25 8 −0.407742

"C17" "CT" 0 1 196611 26 6 0.136191

"C18" "CT" 0 1 196611 27 6 0.045692

"C19" "CT" 0 1 196611 28 6 0.131691

"C20" "CT" 0 1 196611 29 6 0.045692

"C21" "CT" 0 1 196611 30 6 0.131691

"C22" "CT" 0 1 196611 31 6 0.045692

"C23" "CT" 0 1 196611 32 6 0.131691

"C24" "CT" 0 1 196611 33 6 0.045692

"O10" "OS" 0 1 196611 34 8 −0.372057

"O11" "OS" 0 1 196611 35 8 −0.372057

"O12" "OS" 0 1 196611 36 8 −0.372057

"O13" "OS" 0 1 196611 37 8 −0.372057

"C25" "CT" 0 1 196611 38 6 0.085372

"C26" "CT" 0 1 196611 39 6 0.016295

"C27" "CT" 0 1 196611 40 6 0.085372

"C28" "CT" 0 1 196611 41 6 0.016295

"C29" "CT" 0 1 196611 42 6 0.085372

"C30" "CT" 0 1 196611 43 6 0.016295

"C31" "CT" 0 1 196611 44 6 0.085372

"C32" "CT" 0 1 196611 45 6 0.016295

"O14" "OS" 0 1 196611 46 8 −0.372884

"O15" "OS" 0 1 196611 47 8 −0.372884

"O16" "OS" 0 1 196611 48 8 −0.372884

"O17" "OS" 0 1 196611 49 8 −0.372884

"C33" "CT" 0 1 196611 50 6 −0.029532

"C34" "CT" 0 1 196611 51 6 −0.029532

"C35" "CT" 0 1 196611 52 6 −0.029532

"C36" "CT" 0 1 196611 53 6 −0.029532

"H1" "H1" 0 1 196611 54 1 0.038623

"H2" "H1" 0 1 196611 55 1 0.038623

"H3" "H1" 0 1 196611 56 1 0.077090

"H4" "H1" 0 1 196611 57 1 0.077090

"H5" "H1" 0 1 196611 58 1 0.055170

"H6" "H1" 0 1 196611 59 1 0.055170

"H7" "H1" 0 1 196611 60 1 0.071812

"H8" "H1" 0 1 196611 61 1 0.065752

"H9" "H1" 0 1 196611 62 1 0.065752

"H10" "H1" 0 1 196611 63 1 0.071812

"H11" "H1" 0 1 196611 64 1 0.071812

"H12" "H1" 0 1 196611 65 1 0.072951

"H13" "H1" 0 1 196611 66 1 0.072951

"H14" "H1" 0 1 196611 67 1 0.049574

"H15" "H1" 0 1 196611 68 1 0.049574

"H16" "H1" 0 1 196611 69 1 0.055170

"H17" "H1" 0 1 196611 70 1 0.065752

"H18" "H1" 0 1 196611 71 1 0.072951

"H19" "H1" 0 1 196611 72 1 0.071812

"H20" "H1" 0 1 196611 73 1 0.071812

"H21" "H1" 0 1 196611 74 1 0.065752

"H22" "H1" 0 1 196611 75 1 0.049574

"H23" "H1" 0 1 196611 76 1 0.055170

"H24" "H1" 0 1 196611 77 1 0.045683

"H25" "H1" 0 1 196611 78 1 0.077090

"H26" "HC" 0 1 196611 79 1 0.092125

"H27" "H1" 0 1 196611 80 1 0.043314

"H28" "H1" 0 1 196611 81 1 0.043314

"H29" "H1" 0 1 196611 82 1 0.055170

"H30" "H1" 0 1 196611 83 1 0.049574

"H31" "H1" 0 1 196611 84 1 0.071812

"H32" "H1" 0 1 196611 85 1 0.071812

"H33" "HC" 0 1 196611 86 1 0.092125

"H34" "H1" 0 1 196611 87 1 0.077090

"H35" "H1" 0 1 196611 88 1 0.077090

"H36" "H1" 0 1 196611 89 1 0.045683

"H37" "H1" 0 1 196611 90 1 0.045683

"H38" "H1" 0 1 196611 91 1 0.045683

"H39" "H1" 0 1 196611 92 1 0.049574

"H40" "H1" 0 1 196611 93 1 0.055170

"H41" "H1" 0 1 196611 94 1 0.049574

"H42" "H1" 0 1 196611 95 1 0.045683

"H43" "H1" 0 1 196611 96 1 0.065752

"H44" "H1" 0 1 196611 97 1 0.072951

"H45" "H1" 0 1 196611 98 1 0.072951

"H46" "H1" 0 1 196611 99 1 0.071812

"H47" "H1" 0 1 196611 100 1 0.072951

"H48" "H1" 0 1 196611 101 1 0.072951

"H49" "H1" 0 1 196611 102 1 0.071812

"H50" "H1" 0 1 196611 103 1 0.071812

"H51" "H1" 0 1 196611 104 1 0.071812

"H52" "H1" 0 1 196611 105 1 0.065752

"H53" "H1" 0 1 196611 106 1 0.043314

"H54" "H1" 0 1 196611 107 1 0.045683

"H55" "H1" 0 1 196611 108 1 0.049574

"H56" "H1" 0 1 196611 109 1 0.045683

"H57" "H1" 0 1 196611 110 1 0.072951

"H58" "H1" 0 1 196611 111 1 0.071812

"H59" "H1" 0 1 196611 112 1 0.043314

"H60" "H1" 0 1 196611 113 1 0.043314

"H61" "H1" 0 1 196611 114 1 0.065752

"H62" "H1" 0 1 196611 115 1 0.055170

"H63" "H1" 0 1 196611 116 1 0.049574

"H64" "H1" 0 1 196611 117 1 0.077090

"H65" "H1" 0 1 196611 118 1 0.043314

"H66" "H1" 0 1 196611 119 1 0.077090

"H67" "H1" 0 1 196611 120 1 0.066015

"H68" "H1" 0 1 196611 121 1 0.043314

"H69" "H1" 0 1 196611 122 1 0.077090

"H70" "H1" 0 1 196611 123 1 0.055170

"H71" "H1" 0 1 196611 124 1 0.065752

"H72" "H1" 0 1 196611 125 1 0.066015

"H73" "H1" 0 1 196611 126 1 0.043314

"H74" "H1" 0 1 196611 127 1 0.045683

"C37" "CT" 0 1 196611 128 6 0.012491

"O18" "OS" 0 1 196611 129 8 −0.302167

"C38" "CT" 0 1 196611 130 6 0.106672

"H75" "H1" 0 1 196611 131 1 0.066015

"H76" "H1" 0 1 196611 132 1 0.066015

"H77" "H1" 0 1 196611 133 1 0.038623

"H78" "H1" 0 1 196611 134 1 0.038623

"C39" "CT" 0 1 196611 135 6 −0.255856

"C40" "CT" 0 1 196611 136 6 −0.121876

"H79" "HC" 0 1 196611 137 1 0.083980

"H80" "H1" 0 1 196611 138 1 0.165720

"H81" "H1" 0 1 196611 139 1 0.165720

"O19" "OS" 0 1 196611 140 8 −0.136462

!entry.MTY.unit.atomspertinfo table str pname str ptype int ptypex int pelmnt dbl pchg

"C1" "CT" 0 −1 0.0

"C2" "CT" 0 −1 0.0

"O1" "OS" 0 −1 0.0

"C3" "CT" 0 −1 0.0

"C4" "CT" 0 −1 0.0

"C5" "CT" 0 −1 0.0

"C6" "CT" 0 −1 0.0

"C7" "CT" 0 −1 0.0

"C8" "CT" 0 −1 0.0

"O2" "OS" 0 −1 0.0

"O3" "OS" 0 −1 0.0

"C9" "CT" 0 −1 0.0

"C10" "CT" 0 −1 0.0

"C11" "CT" 0 −1 0.0

"C12" "CT" 0 −1 0.0

"O4" "OS" 0 −1 0.0

"O5" "OS" 0 −1 0.0

"C13" "CT" 0 −1 0.0

"C14" "CT" 0 −1 0.0

"C15" "CT" 0 −1 0.0

"C16" "CT" 0 −1 0.0

"O6" "OS" 0 −1 0.0

"O7" "OS" 0 −1 0.0

"O8" "OS" 0 −1 0.0

"O9" "OS" 0 −1 0.0

"C17" "CT" 0 −1 0.0

"C18" "CT" 0 −1 0.0

"C19" "CT" 0 −1 0.0

"C20" "CT" 0 −1 0.0

"C21" "CT" 0 −1 0.0

"C22" "CT" 0 -1 0.0

"C23" "CT" 0 -1 0.0

"C24" "CT" 0 -1 0.0

"O10" "OS" 0 -1 0.0

"O11" "OS" 0 -1 0.0

"O12" "OS" 0 -1 0.0

"O13" "OS" 0 -1 0.0

"C25" "CT" 0 -1 0.0

"C26" "CT" 0 -1 0.0

"C27" "CT" 0 -1 0.0

"C28" "CT" 0 -1 0.0

"C29" "CT" 0 -1 0.0

"C30" "CT" 0 -1 0.0

"C31" "CT" 0 -1 0.0

"C32" "CT" 0 -1 0.0

"O14" "OS" 0 -1 0.0

"O15" "OS" 0 -1 0.0

"O16" "OS" 0 -1 0.0

"O17" "OS" 0 -1 0.0

"C33" "CT" 0 -1 0.0

"C34" "CT" 0 -1 0.0

"C35" "CT" 0 -1 0.0

"C36" "CT" 0 -1 0.0

"H1" "H1" 0 -1 0.0

"H2" "H1" 0 -1 0.0

"H3" "H1" 0 -1 0.0

"H4" "H1" 0 -1 0.0

"H5" "H1" 0 -1 0.0

"H6" "H1" 0 -1 0.0

"H7" "H1" 0 -1 0.0

"H8" "H1" 0 -1 0.0

"H9" "H1" 0 -1 0.0

"H10" "H1" 0 -1 0.0

"H11" "H1" 0 -1 0.0

"H12" "H1" 0 −1 0.0

"H13" "H1" 0 −1 0.0

"H14" "H1" 0 −1 0.0

"H15" "H1" 0 −1 0.0

"H16" "H1" 0 −1 0.0

"H17" "H1" 0 −1 0.0

"H18" "H1" 0 −1 0.0

"H19" "H1" 0 −1 0.0

"H20" "H1" 0 −1 0.0

"H21" "H1" 0 −1 0.0

"H22" "H1" 0 −1 0.0

"H23" "H1" 0 −1 0.0

"H24" "H1" 0 −1 0.0

"H25" "H1" 0 −1 0.0

"H26" "HC" 0 −1 0.0

"H27" "H1" 0 −1 0.0

"H28" "H1" 0 −1 0.0

"H29" "H1" 0 −1 0.0

"H30" "H1" 0 −1 0.0

"H31" "H1" 0 −1 0.0

"H32" "H1" 0 −1 0.0

"H33" "HC" 0 −1 0.0

"H34" "H1" 0 −1 0.0

"H35" "H1" 0 −1 0.0

"H36" "H1" 0 −1 0.0

"H37" "H1" 0 −1 0.0

"H38" "H1" 0 −1 0.0

"H39" "H1" 0 −1 0.0

"H40" "H1" 0 −1 0.0

"H41" "H1" 0 −1 0.0

"H42" "H1" 0 −1 0.0

"H43" "H1" 0 −1 0.0

"H44" "H1" 0 −1 0.0

"H45" "H1" 0 −1 0.0

"H46" "H1" 0 -1 0.0

"H47" "H1" 0 -1 0.0

"H48" "H1" 0 -1 0.0

"H49" "H1" 0 -1 0.0

"H50" "H1" 0 -1 0.0

"H51" "H1" 0 -1 0.0

"H52" "H1" 0 -1 0.0

"H53" "H1" 0 -1 0.0

"H54" "H1" 0 -1 0.0

"H55" "H1" 0 -1 0.0

"H56" "H1" 0 -1 0.0

"H57" "H1" 0 -1 0.0

"H58" "H1" 0 -1 0.0

"H59" "H1" 0 -1 0.0

"H60" "H1" 0 -1 0.0

"H61" "H1" 0 -1 0.0

"H62" "H1" 0 -1 0.0

"H63" "H1" 0 -1 0.0

"H64" "H1" 0 -1 0.0

"H65" "H1" 0 -1 0.0

"H66" "H1" 0 -1 0.0

"H67" "H1" 0 -1 0.0

"H68" "H1" 0 -1 0.0

"H69" "H1" 0 -1 0.0

"H70" "H1" 0 -1 0.0

"H71" "H1" 0 -1 0.0

"H72" "H1" 0 -1 0.0

"H73" "H1" 0 -1 0.0

"H74" "H1" 0 -1 0.0

"C37" "CT" 0 -1 0.0

"O18" "OS" 0 -1 0.0

"C38" "CT" 0 -1 0.0

"H75" "H1" 0 -1 0.0

"H76" "H1" 0 -1 0.0

"H77" "H1" 0 -1 0.0

"H78" "H1" 0 -1 0.0

"C39" "CT" 0 -1 0.0

"C40" "CT" 0 -1 0.0

"H79" "HC" 0 -1 0.0

"H80" "H1" 0 -1 0.0

"H81" "H1" 0 -1 0.0

"O19" "OS" 0 -1 0.0

!entry.MTY.unit.boundbox array dbl

-1.000000

0.0

0.0

0.0

0.0

!entry.MTY.unit.childsequence single int

2

!entry.MTY.unit.connect array int

0

0

!entry.MTY.unit.connectivity table int atom1x int atom2x int flags

1 135 1

1 3 1

1 55 1

1 54 1

2 128 1

2 8 1

2 9 1

2 79 1

3 4 1

4 5 1

4 120 1

4 125 1

5 7 1

5 6 1

5 86 1

6 11 1

6 117 1

6 87 1

7 10 1

7 119 1

7 88 1

8 56 1

8 17 1

8 57 1

9 16 1

9 78 1

9 122 1

10 12 1

11 14 1

12 13 1

12 121 1

12 81 1

13 22 1

13 90 1

13 91 1

14 15 1

14 118 1

14 126 1

15 23 1

15 89 1

15 95 1

16 19 1

17 18 1

18 20 1

18 106 1

18 112 1

19 21 1

19 113 1

19 80 1

20 25 1

20 127 1

20 107 1

21 24 1

21 109 1

21 77 1

22 30 1

23 32 1

24 28 1

25 26 1

26 27 1

26 68 1

26 67 1

27 37 1

27 58 1

27 59 1

28 29 1

28 108 1

28 75 1

29 36 1

29 76 1

29 69 1

30 31 1

30 92 1

30 83 1

31 35 1

31 82 1

31 123 1

32 33 1

32 94 1

32 116 1

33 34 1

33 115 1

33 93 1

34 44 1

35 42 1

36 40 1

37 38 1

38 39 1

38 62 1

38 61 1

39 48 1

39 66 1

39 65 1

40 41 1

40 70 1

40 74 1

41 47 1

41 110 1

41 71 1

42 43 1

42 105 1

42 124 1

43 46 1

43 100 1

43 101 1

44 45 1

44 96 1

44 114 1

45 49 1

45 97 1

45 98 1

46 52 1

47 51 1

48 50 1

49 53 1

50 63 1

50 64 1

50 60 1

51 72 1

51 111 1

51 73 1

52 103 1

52 104 1

52 102 1

53 85 1

53 84 1

53 99 1

128 129 1

128 131 1

128 132 1

129 130 1

130 135 1

130 133 1

130 134 1

135 136 1

135 137 1

136 140 1

136 139 1

136 138 1

!entry.MTY.unit.hierarchy table  str abovetype  int abovex  str belowtype  int belowx

"U" 0 "R" 1

"R" 1 "A" 1

"R" 1 "A" 2

"R" 1 "A" 3

"R" 1 "A" 4

"R" 1 "A" 5

"R" 1 "A" 6

"R" 1 "A" 7

"R" 1 "A" 8

"R" 1 "A" 9

"R" 1 "A" 10

"R" 1 "A" 11

"R" 1 "A" 12

"R" 1 "A" 13

"R" 1 "A" 14

"R" 1 "A" 15

"R" 1 "A" 16

"R" 1 "A" 17

"R" 1 "A" 18

"R" 1 "A" 19

"R" 1 "A" 20

"R" 1 "A" 21

"R" 1 "A" 22

"R" 1 "A" 23

"R" 1 "A" 24

"R" 1 "A" 25

"R" 1 "A" 26

"R" 1 "A" 27

"R" 1 "A" 28

"R" 1 "A" 29

"R" 1 "A" 30

"R" 1 "A" 31

"R" 1 "A" 32

"R" 1 "A" 33

"R" 1 "A" 34

"R" 1 "A" 35

"R" 1 "A" 36

"R" 1 "A" 37

"R" 1 "A" 38

"R" 1 "A" 39

"R" 1 "A" 40

"R" 1 "A" 41

"R" 1 "A" 42

"R" 1 "A" 43

"R" 1 "A" 44

"R" 1 "A" 45

"R" 1 "A" 46

"R" 1 "A" 47

"R" 1 "A" 48

"R" 1 "A" 49

"R" 1 "A" 50

"R" 1 "A" 51

"R" 1 "A" 52

"R" 1 "A" 53

"R" 1 "A" 54

"R" 1 "A" 55

"R" 1 "A" 56

"R" 1 "A" 57

"R" 1 "A" 58

"R" 1 "A" 59

"R" 1 "A" 60

"R" 1 "A" 61

"R" 1 "A" 62

"R" 1 "A" 63

"R" 1 "A" 64

"R" 1 "A" 65

"R" 1 "A" 66

"R" 1 "A" 67

"R" 1 "A" 68

"R" 1 "A" 69

"R" 1 "A" 70

"R" 1 "A" 71

"R" 1 "A" 72

"R" 1 "A" 73

"R" 1 "A" 74

"R" 1 "A" 75

"R" 1 "A" 76

"R" 1 "A" 77

"R" 1 "A" 78

"R" 1 "A" 79

"R" 1 "A" 80

"R" 1 "A" 81

"R" 1 "A" 82

"R" 1 "A" 83

"R" 1 "A" 84

"R" 1 "A" 85

"R" 1 "A" 86

"R" 1 "A" 87

"R" 1 "A" 88

"R" 1 "A" 89

"R" 1 "A" 90

"R" 1 "A" 91

"R" 1 "A" 92

"R" 1 "A" 93

"R" 1 "A" 94

"R" 1 "A" 95

"R" 1 "A" 96

"R" 1 "A" 97

"R" 1 "A" 98

"R" 1 "A" 99

"R" 1 "A" 100

"R" 1 "A" 101

"R" 1 "A" 102

"R" 1 "A" 103

"R" 1 "A" 104

"R" 1 "A" 105

"R" 1 "A" 106

"R" 1 "A" 107

"R" 1 "A" 108

"R" 1 "A" 109

"R" 1 "A" 110

"R" 1 "A" 111

"R" 1 "A" 112

"R" 1 "A" 113

"R" 1 "A" 114

"R" 1 "A" 115

"R" 1 "A" 116

"R" 1 "A" 117

"R" 1 "A" 118

"R" 1 "A" 119

"R" 1 "A" 120

"R" 1 "A" 121

"R" 1 "A" 122

"R" 1 "A" 123

"R" 1 "A" 124

"R" 1 "A" 125

"R" 1 "A" 126

"R" 1 "A" 127

"R" 1 "A" 128

"R" 1 "A" 129

"R" 1 "A" 130

"R" 1 "A" 131

"R" 1 "A" 132

"R" 1 "A" 133

"R" 1 "A" 134

"R" 1 "A" 135

"R" 1 "A" 136

"R" 1 "A" 137

"R" 1 "A" 138

"R" 1 "A" 139

"R" 1 "A" 140

!entry.MTY.unit.name single str

""

!entry.MTY.unit.positions table dbl x dbl y dbl z

4.534000 −3.687000 −0.854000

3.754000 1.166000 −0.791000

3.299000 −4.014000 −0.228000

2.259000 −3.077000 −0.514000

1.086000 −3.384000 0.409000

−0.109000 −2.517000 0.018000

1.482000 −3.131000 1.858000

4.906000 1.632000 −1.681000

2.706000 0.396000 −1.586000

0.402000 −3.591000 2.667000

−0.713000 −2.990000 −1.181000

0.622000 −3.422000 4.065000

−0.582000 −2.696000 4.661000

−1.705000 −3.985000 −0.954000

−2.120000 −4.558000 −2.302000

2.148000 1.281000 −2.559000

5.319000 2.930000 −1.253000

5.164000 3.956000 −2.223000

0.771000 1.047000 −2.818000

3.707000 4.304000 −2.508000

−0.114000 1.746000 −1.789000

−0.345000 −1.296000 4.742000

−2.458000 −3.604000 −3.294000

−0.259000 0.861000 −0.679000

3.207000 5.296000 −1.619000

2.923000 4.792000 −0.315000

2.444000 5.969000 0.528000

−1.361000 1.171000 0.161000

−1.096000 2.427000 0.986000

−0.670000 −0.580000 3.558000

−2.174000 −0.348000 3.443000

−3.370000 −2.593000 −2.899000

−4.725000 −3.168000 −2.497000

−5.702000 −2.214000 −2.910000

−2.658000 −1.249000 2.444000

−2.157000 2.656000 1.902000

1.029000 6.096000 0.489000

0.550000 6.729000 −0.698000

−0.956000 6.503000 −0.754000

−3.267000 3.344000 1.327000

−4.395000 3.285000 2.351000

−4.075000 −1.173000 2.305000

−4.430000 −1.973000 1.056000

−7.020000 −2.610000 −2.537000

−7.948000 −1.501000 −3.023000

−5.812000 −1.839000 0.758000

−5.183000 2.139000 2.032000

−1.680000 7.526000 −0.089000

−9.297000 −1.794000 −2.694000

−1.603000 7.451000 1.326000

−6.245000 1.938000 2.949000

−6.131000 −0.650000 0.049000

−9.634000 −1.521000 −1.345000

4.910000 −4.659000 −1.275000

4.400000 −2.942000 −1.681000

5.802000 0.967000 −1.549000

4.594000 1.629000 −2.757000

2.665000 5.769000 1.611000

2.939000 6.918000 0.199000

−0.538000 7.447000 1.666000

1.048000 6.279000 −1.598000

0.786000 7.825000 −0.646000

−2.134000 8.368000 1.684000

−2.121000 6.529000 1.691000

−1.217000 5.498000 −0.326000

−1.307000 6.576000 −1.819000

3.855000 4.344000 0.122000

2.123000 4.007000 −0.385000

−0.933000 3.318000 0.324000

−2.973000 4.412000 1.137000

−3.984000 3.188000 3.391000

−5.849000 1.780000 3.983000

−6.760000 1.015000 2.581000

−3.580000 2.859000 0.367000

−1.457000 0.271000 0.834000

−0.195000 2.281000 1.641000

0.368000 2.697000 −1.437000

1.910000 0.013000 −0.891000

3.268000 2.080000 −0.342000

0.545000 −0.050000 −2.851000

0.697000 −4.455000 4.500000

−2.684000 −0.554000 4.420000

−0.144000 0.404000 3.684000

−9.053000 −2.175000 −0.648000

−10.727000 −1.753000 −1.280000

0.810000 −4.469000 0.299000

0.215000 −1.469000 −0.238000

2.416000 −3.704000 2.107000

−2.989000 −5.249000 −2.136000

−1.507000 −2.911000 4.063000

−0.721000 −3.012000 5.729000

−0.285000 −1.118000 2.650000

−4.913000 −4.148000 −3.010000

−3.473000 −1.955000 −3.820000

−1.264000 −5.117000 −2.770000

−7.280000 −3.587000 −3.021000

−7.940000 −1.445000 −4.144000

−7.630000 −0.516000 −2.591000

−9.447000 −0.446000 −1.100000

−3.794000 −1.651000 0.190000

−4.289000 −3.072000 1.238000

−5.801000 0.259000 0.610000

−7.248000 −0.674000 −0.041000

−5.664000 −0.676000 −0.970000

−4.561000 −1.618000 3.213000

5.695000 4.834000 −1.764000

3.624000 4.793000 −3.516000

−2.299000 1.283000 −0.444000

−1.115000 1.973000 −2.241000

−5.031000 4.207000 2.276000

−6.945000 2.810000 2.939000

5.671000 3.660000 −3.179000

0.603000 1.511000 −3.827000

−7.076000 −2.720000 −1.419000

−4.788000 −3.310000 −1.383000

−2.936000 −1.983000 −2.064000

−0.851000 −2.481000 0.862000

−2.582000 −3.516000 −0.427000

1.659000 −2.037000 2.041000

1.940000 −3.198000 −1.584000

1.564000 −2.856000 4.280000

3.175000 −0.465000 −2.132000

−2.385000 0.708000 3.119000

−4.402000 −0.102000 2.203000

2.631000 −2.028000 −0.352000

−1.295000 −4.809000 −0.311000

3.064000 3.383000 −2.473000

4.255000 0.307000 0.365000

4.745000 −0.920000 −0.176000

5.047000 −1.872000 0.845000

3.416000 0.095000 1.081000

5.087000 0.830000 0.906000

4.119000 −2.083000 1.445000

5.848000 −1.462000 1.515000

5.529000 −3.153000 0.176000

6.872000 −2.940000 −0.510000

5.648000 −3.919000 0.994000

7.128000 −3.791000 −1.193000

6.893000 −1.976000 −1.082000

7.854000 −2.880000 0.540000

!entry.MTY.unit.residueconnect table int c1x int c2x int c3x int c4x int c5x int c6x

0 0 0 0 0 0

!entry.MTY.unit.residues table str name int seq int childseq int startatomx str restype int imagingx

"MTY" 1 141 1 "?" 0

!entry.MTY.unit.residuesPdbSequenceNumber array int

1

!entry.MTY.unit.solventcap array dbl

−1.000000

0.0

0.0

0.0

0.0

!entry.MTY.unit.velocities table dbl x dbl y dbl z

0.0 0.0 0.0

0.0 0.0 0.0

0.0 0.0 0.0

0.0 0.0 0.0

0.0 0.0 0.0

0.0 0.0 0.0

0.0 0.0 0.0

0.0 0.0 0.0

0.0 0.0 0.0

0.0 0.0 0.0

0.0 0.0 0.0

0.0 0.0 0.0

0.0 0.0 0.0

0.0 0.0 0.0

0.0 0.0 0.0

0.0 0.0 0.0

0.0 0.0 0.0

0.0 0.0 0.0

0.0 0.0 0.0

0.0 0.0 0.0

0.0 0.0 0.0

0.0 0.0 0.0

0.0 0.0 0.0

0.0 0.0 0.0

0.0 0.0 0.0

0.0 0.0 0.0

0.0 0.0 0.0

0.0 0.0 0.0

0.0 0.0 0.0

0.0 0.0 0.0

0.0 0.0 0.0

0.0 0.0 0.0

0.0 0.0 0.0

0.0 0.0 0.0

0.0 0.0 0.0

0.0 0.0 0.0

0.0 0.0 0.0

0.0 0.0 0.0

0.0 0.0 0.0

0.0 0.0 0.0

0.0 0.0 0.0

0.0 0.0 0.0

0.0 0.0 0.0

0.0 0.0 0.0

0.0 0.0 0.0

0.0 0.0 0.0

0.0 0.0 0.0

0.0 0.0 0.0

0.0 0.0 0.0

0.0 0.0 0.0

0.0 0.0 0.0

0.0 0.0 0.0

0.0 0.0 0.0

0.0 0.0 0.0

0.0 0.0 0.0

0.0 0.0 0.0

0.0 0.0 0.0

0.0 0.0 0.0

0.0 0.0 0.0

0.0 0.0 0.0

0.0 0.0 0.0

0.0 0.0 0.0

0.0 0.0 0.0

0.0 0.0 0.0

0.0 0.0 0.0

0.0 0.0 0.0

0.0 0.0 0.0

0.0 0.0 0.0

0.0 0.0 0.0

0.0 0.0 0.0

0.0 0.0 0.0

0.0 0.0 0.0

0.0 0.0 0.0

0.0 0.0 0.0

0.0 0.0 0.0

0.0 0.0 0.0

0.0 0.0 0.0

0.0 0.0 0.0

0.0 0.0 0.0

0.0 0.0 0.0

0.0 0.0 0.0

0.0 0.0 0.0

0.0 0.0 0.0

0.0 0.0 0.0

0.0 0.0 0.0

```
0.0 0.0 0.0
0.0 0.0 0.0
0.0 0.0 0.0
0.0 0.0 0.0
0.0 0.0 0.0
0.0 0.0 0.0
0.0 0.0 0.0
0.0 0.0 0.0
0.0 0.0 0.0
0.0 0.0 0.0
0.0 0.0 0.0
0.0 0.0 0.0
0.0 0.0 0.0
0.0 0.0 0.0
0.0 0.0 0.0
0.0 0.0 0.0
0.0 0.0 0.0
0.0 0.0 0.0
0.0 0.0 0.0
0.0 0.0 0.0
0.0 0.0 0.0
0.0 0.0 0.0
0.0 0.0 0.0
0.0 0.0 0.0
0.0 0.0 0.0
0.0 0.0 0.0
0.0 0.0 0.0
0.0 0.0 0.0
0.0 0.0 0.0
0.0 0.0 0.0
0.0 0.0 0.0
0.0 0.0 0.0
0.0 0.0 0.0
0.0 0.0 0.0
```

0.0 0.0 0.0

0.0 0.0 0.0

0.0 0.0 0.0

0.0 0.0 0.0

0.0 0.0 0.0

0.0 0.0 0.0

0.0 0.0 0.0

0.0 0.0 0.0

0.0 0.0 0.0

0.0 0.0 0.0

0.0 0.0 0.0

0.0 0.0 0.0

0.0 0.0 0.0

0.0 0.0 0.0

0.0 0.0 0.0

0.0 0.0 0.0

0.0 0.0 0.0

0.0 0.0 0.0

0.0 0.0 0.0

0.0 0.0 0.0

0.0 0.0 0.0

AP.II-2. Parameter and topology information of tri(ethylene glycol) monomethyl ether for the MD simulation

(1) frcmod file:

MASS

BOND

C-OS 411.3 1.343 SOURCE1 1044 0.0114 0.0171 (gaff c -os)

ANGLE

CA-C-OS 68.8 115.54 SOURCE3 5 2.1366 2.6708 (gaff ca-c -

os)

C-OH-CT 63.6 115.14 SOURCE3 17 1.5416 1.8967 (gaff c -os-c3)

DIHE

CA-C-OS-CT 2 5.400 180.000 2.000 Junmei et al, 1999 (gaff X -c -os-X)

IMPROPER

NONBON

## (2) library file:

!!index array str

"mTY"

!entry.mTY.unit.atoms table str name str type int typex int resx int flags int seq int elmnt dbl chg

"C12" "CT" 0 1 131073 29 6 0.953377

"C13" "CT" 0 1 131073 30 6 0.043855

"O4" "OS" 0 1 131073 31 -1 -0.329055

"C14" "CT" 0 1 131073 32 6 -0.011501

"C15" "CT" 0 1 131073 33 6 -0.023039

"O5" "OS" 0 1 131073 34 -1 -0.240019

"C16" "CT" 0 1 131073 35 6 -0.013476

"C17" "CT" 0 1 131073 36 6 -0.037332

"O6" "OS" 0 1 131073 37 -1 -0.277426

"C18" "CT" 0 1 131073 38 6 -0.043293

"H13" "H1" 0 1 131073 39 1 -0.222875

"H14" "H1" 0 1 131073 40 1 0.010370

"H15" "H1" 0 1 131073 41 1 0.010370

"H16" "H1" 0 1 131073 42 1 0.078749

"H17" "H1" 0 1 131073 43 1 0.078749

"H18" "H1" 0 1 131073 44 1 0.069423

"H19" "H1" 0 1 131073 45 1 0.073943

"H20" "H1" 0 1 131073 46 1 0.073360

"H21" "H1" 0 1 131073 47 1 0.073360

"H22" "H1" 0 1 131073 48 1 0.070390

"H23" "H1" 0 1 131073 49 1 0.070390

"H24" "H1" 0 1 131073 50 1 0.070390

"H25" "H1" 0 1 131073 51 1 −0.222875

"H26" "H1" 0 1 131073 52 1 0.069423

"H27" "H1" 0 1 131073 53 1 0.073943

!entry.mTY.unit.atomspertinfo table str pname str ptype int ptypex int pelmnt dbl pchg

"C12" "CT" 0 −1 0.0

"C13" "CT" 0 −1 0.0

"O4" "OS" 0 −1 0.0

"C14" "CT" 0 −1 0.0

"C15" "CT" 0 −1 0.0

"O5" "OS" 0 −1 0.0

"C16" "CT" 0 −1 0.0

"C17" "CT" 0 −1 0.0

"O6" "OS" 0 −1 0.0

"C18" "CT" 0 −1 0.0

"H13" "H1" 0 −1 0.0

"H14" "H1" 0 −1 0.0

"H15" "H1" 0 −1 0.0

"H16" "H1" 0 −1 0.0

"H17" "H1" 0 −1 0.0

"H18" "H1" 0 −1 0.0

"H19" "H1" 0 −1 0.0

"H20" "H1" 0 −1 0.0

"H21" "H1" 0 −1 0.0

"H22" "H1" 0 −1 0.0

"H23" "H1" 0 −1 0.0

"H24" "H1" 0 −1 0.0

"H25" "H1" 0 -1 0.0

"H26" "H1" 0 -1 0.0

"H27" "H1" 0 -1 0.0

!entry.mTY.unit.boundbox array dbl

-1.000000

0.0

0.0

0.0

0.0

!entry.mTY.unit.childsequence single int

2

!entry.mTY.unit.connect array int

0

0

!entry.mTY.unit.connectivity table  int atom1x  int atom2x  int flags

10 21 1

10 20 1

10 22 1

9 10 1

8 9 1

8 19 1

8 18 1

7 8 1

7 25 1

7 17 1

6 7 1

5 6 1

5 16 1

5 24 1

4 5 1

4 14 1

4 15 1

3 4 1

2 3 1

2 13 1

2 12 1

1 2 1

1 11 1

1 23 1

!entry.mTY.unit.hierarchy table  str abovetype  int abovex  str belowtype  int belowx

"U" 0 "R" 1

"R" 1 "A" 25

"R" 1 "A" 24

"R" 1 "A" 23

"R" 1 "A" 22

"R" 1 "A" 21

"R" 1 "A" 20

"R" 1 "A" 19

"R" 1 "A" 18

"R" 1 "A" 17

"R" 1 "A" 16

"R" 1 "A" 15

"R" 1 "A" 14

"R" 1 "A" 13

"R" 1 "A" 12

"R" 1 "A" 11

"R" 1 "A" 10

"R" 1 "A" 9

"R" 1 "A" 8

"R" 1 "A" 7

"R" 1 "A" 6

"R" 1 "A" 5

"R" 1 "A" 4

"R" 1 "A" 3

"R" 1 "A" 2

"R" 1 "A" 1

!entry.mTY.unit.name single str

"default_name"

```
!entry.mTY.unit.positions table    dbl x    dbl y    dbl z
  2.394000 −3.020000 0.422000
  3.904000 −2.983000 0.301000
  4.367000 −1.723000 0.734000
  5.766000 −1.569000 0.598000
  6.165000 −0.178000 1.051000
  5.736000 0.767000 0.096000
  6.056000 2.096000 0.452000
  5.509000 3.044000 −0.598000
  4.107000 3.127000 −0.466000
  3.513000 3.931000 −1.461000
  2.039000 −4.055000 0.307000
  4.193000 −3.175000 −0.745000
  4.329000 −3.793000 0.920000
  6.300000 −2.315000 1.214000
  6.075000 −1.714000 −0.450000
  7.264000 −0.144000 1.168000
  7.151000 2.226000 0.519000
  5.791000 2.678000 −1.599000
  5.972000 4.038000 −0.462000
  3.886000 4.969000 −1.427000
  3.696000 3.532000 −2.472000
  2.437000 3.936000 −1.272000
  2.098000 −2.655000 1.414000
  5.718000 0.027000 2.038000
  5.626000 2.354000 1.434000
!entry.mTY.unit.residueconnect table    int c1x    int c2x    int c3x    int c4x    int c5x    int
c6x
  0 0 0 0 0 0
!entry.mTY.unit.residues table    str name    int seq    int childseq    int startatomx    str
restype    int imagingx
  "mTY" 1 59 1 "?" 0
!entry.mTY.unit.residuesPdbSequenceNumber array int
  1
```

```
!entry.mTY.unit.solventcap array dbl
 −1.000000
 0.0
 0.0
 0.0
 0.0
!entry.mTY.unit.velocities table    dbl x    dbl y    dbl z
 0.0 0.0 0.0
 0.0 0.0 0.0
 0.0 0.0 0.0
 0.0 0.0 0.0
 0.0 0.0 0.0
 0.0 0.0 0.0
 0.0 0.0 0.0
 0.0 0.0 0.0
 0.0 0.0 0.0
 0.0 0.0 0.0
 0.0 0.0 0.0
 0.0 0.0 0.0
 0.0 0.0 0.0
 0.0 0.0 0.0
 0.0 0.0 0.0
 0.0 0.0 0.0
 0.0 0.0 0.0
 0.0 0.0 0.0
 0.0 0.0 0.0
 0.0 0.0 0.0
 0.0 0.0 0.0
 0.0 0.0 0.0
 0.0 0.0 0.0
```

# 국문초록

DNA 독트린에 따르면 유전정보는 복제, 전사, 해독의 과정을 거쳐서 DNA에서 단백질로 이동된다. 유전정보 해독의 결과 생성된 단백질은 해당 기능에 맞게 단백질접힘 현상이 발생하게 되는데, 이는 전형적인 자기조립현상이다. 이를 에너지 측면에서 보면, 보통의 단백질은 단백질 젖힘현상의 결과 생성된 구조에 해당하는 에너지 깊은 협곡에 위치하게 된다. 그러나 알파 시뉴클린과 아밀로이트 베타 같은 내재적 부정형 단백질의 경우 그러한 에너지 깊은 협곡에 존재하지 않는다. DNA 복제에서부터 단백질 해독후 과정에 이르는 유전정보의 흐름 속의 어떠한 이상에도 심각한 질병을 야기할 수 있기 때문에, 단백질의 구조 및 그에 대한 동역학적 연구는 치료적 목적을 위해서라도 반드시 필요하다 할 것이다.

이에 우리는 여러 형태의 알파 시뉴클린, 아밀로이드 베타 그리고 인공 단백질에 관한 동역학적 연구를 다양한 환경하에서 다양한 방법으로 진행하였다.

알파 시뉴클린은 140개의 아미노산으로 구성되어 있으며, 3개의 기능적 부분(membrane binding, the NAC and the acidic domains)으로 분리되며, P128이 NAC 영역의 중간부분과 높은 확률로 접촉하고 있으나, the acidic domain의 P-to-A 돌연변이 및 산성도 변화 같은 요인으로 이를 변화시킬 수 있다. Acidic 영역의 프롤린이 아밀로이드 형성에 분자내부적 샤페론의 역할을 하고 있는 듯 하다.

아밀로이드 베타는 아밀로이드 단백질 전구체로부터 베타

시크리테이제에 의해 분비되며 일반적으로 40~42개의 아미노산으로 구성된다. 아밀로이드 베타-42의 C-말단 아미노산중 아이소루이신과 알라닌은 중간체의 포텐셜 에너지를 보다 차이나게 하며, 각 중간체 간의 구조변화에 대한 에너지 장벽을 높이고, 아밀로이드 구조체의 안정성에 긍정적 역할을 하는 듯 하다. 이렇듯 아이소루이신과 알라린은 아밀로이드 형성에 촉진자로서 역할을 하고 있는 듯 하다.

베타 펩타이드를 이용한 인공단백질 설계를 위해서는 정전기적 인력, 수소결합, 소수성, 그리고 전자 반발력의 최적화를 고려해야 하는데, 전자 반발력의 최적화가 인공단백질 설계에 주요한 인자로 작용한다.

.....

**주요어 : 동역학, 알파 시뉴클린, 아밀로이드 베타, 샤페론, 촉진자**

**학 번 : 2008-30092**